University of Nottingham
UK | CHINA | MALAYSIA

Three-Dimensional Inkjet Printing of Electrically Active Materials

Oliver Bryn Nelson-Dummett
(EPSRC DTP with MTC)

Thesis submitted to the University of Nottingham for the degree

of Doctor of Philosophy

November 2024

Abstract

Additive Manufacturing (AM) for electronics (AME) offers the capability for a new generation of devices, with digitised customisation, remarkable design freedom, and low wastage. To achieve this, AM must enable excellent material properties, high resolution, multi-material processing, and scalability to attain industrial relevance. Inkjet printing (IJP) is one of the most mature technologies capable of such material properties and resolution, originating from graphical printing but now with several decades of research into functional materials behind it. IJP excels at multi-material processing and scalability, but major criticisms are the high anisotropy and inability to print truly 3D geometries, generally settling on 2.5D heterostructures instead.

This work reports on a new finding that the anisotropy of conductivity in silver nanoparticle inks has been overestimated, and that it is mostly independent of the ink composition. Further, four polymer inks were investigated to pair with the silver ink as support and for high-quality dielectric contrast. Additionally, a novel method which requires no custom hardware – "Off the Grid" – was developed to remove aliasing which artificially decreases drop placement fidelity. This increases the accuracy of shape outlines and provides methods to control layer topology and negative space.

This work was built upon to create 3D structures with uniquely complex geometries compared to previous IJP efforts, with single-drop-wide micropillars printed ≤ 4 mm high. After investigating the growth mechanism of the pillars, it was shown that they can lean without support, which enables the printing of helices and strut-based lattices. Finally, multimaterial prints are demonstrated with anisotropic silver elements within a dielectric matrix, which allows for easy control of the macro dielectric properties. Overall, this work pushes the boundaries of achievable geometries within AME and opens the potential for a wide range of functional devices to be inkjet-printed.

Publications, Conferences, and Awards

PUBLICATIONS:

- Off the Grid: A new strategy for material-jet 3D printing with enhanced sub-droplet resolution, **O. Nelson-Dummett**, G. Rivers, N. Gilani, M. Simonelli, C. J. Tuck, R. D. Wildman, R. Hague, L. Turyanska, Add. Manuf. Lett., 2024, 8, 100185.
- Photosensitisation of inkjet printed graphene with stable all-inorganic perovskite nanocrystals, J. S. Austin, N. D. Cottam, C. Zhang, F. Wang, J. H. Gosling, **O. Nelson-Dummett**, G. F. Trindade, Y. Zhou, T. S. S. James, P. H. Beton, C. Tuck, R. Hague, O. Makarovsky, L. Turyanska, Nanoscale, 2023, 15, 2134.
- Formulation of Functional Materials for Inkjet Printing: a Pathway Towards 3D electronics, A. Bastola, Y. He, J. Im, F. Wang, R. Worsley, J. S. Austin, **O. Nelson-Dummett**, R. D. Wildman, R. Hague, C. J. Tuck, L. Turyanska, Mater. Today Electron, 2023, 6, 100058.

CONFERENCE PRESENTATIONS:

- META Annual Conference, Toyama, Japan (16^{th}-19^{th} July 2024). Poster presentation. Multimaterial Inkjet Printing for Microwave Metamaterials.

- UK Metamaterials AGM, Dorking, UK (19^{th}-23^{rd} May 2024). Poster presentation. Multimaterial Inkjet Printing for Microwave Metamaterials.

- Manufacturing Technology Centre Additive Manufacturing Exchange, Coventry, UK (13^{th}-14^{th} September 2023). Poster presentation. Three-Dimensional Inkjet Printing of Electrically Active Materials.

- Manufacturing Technology Centre PhD and Industry conference, Coventry, UK (7^{th} June 2023). Poster presentation. Three-Dimensional Inkjet Printing of Electrically Active Materials.

- Solid Freeform Fabrication conference, Austin, Texas (14th-19th August 2023). Oral Presentation. Off the Grid: Redefining Resolution in Material Jetting.

- UK Metamaterials Network Summer School (15th-19th August 2022). Poster Presentation. Inkjet Printing of 3D Metamaterials in the THz/Microwave Region

- Manufacturing Technology Centre PhD and Industry conference, Coventry, UK (29th June 2022). Oral presentation. Three-Dimensional Inkjet Printing of Electrically Active Materials.

- Engineering Research Showcase, Nottingham (28th April 2022). Poster presentation. Three-Dimensional Inkjet Printing of Electrically Active Materials.

- Manufacturing Technology Centre PhD and Industry conference, Coventry, UK (29th-30th June 2021). Poster presentation. Three-Dimensional Inkjet Printing of Electrically Active Materials.

AWARDS:

- Researcher Academy Travel Grant, £250.
- Accepted to Roche Continents Future Leaders programme, turned down due to prior conference commitment

Acknowledgements

Any and all success in my academic life for the past four years owes itself to my supervisor, Lyudmila Turyanska. I cannot imagine a way in which she could be a better supervisor, be it her awe-inspiring work ethic, brilliant mentorship in matters both technical and professional, or genuine happiness at my achievements. There may one day be a moment where I am right and she is wrong, but that moment has yet to come in our time working together.

I would also like to thank my co-supervisors Richard Hague and Christopher Tuck, whose knowledge and experience have helped to steer me around the many pitfalls of such a long-term project and guided me into the start of my academic career. Further, my gratitude goes to my co-supervisor Feiran Wang, who taught me everything I know about inkjet printing and whose unceasing helpfulness made me feel welcome as a new student emerging from pandemic lockdown. My thanks also go to Naim Kapadia, Caitlin McCall, Jacek Wojcik, and the Manufacturing Technology Centre (MTC) at large, for their support, funding, and insight into the world of industry over what would otherwise have been a very academic four years.

I have received endless support and friendship from all of my colleagues at the Centre for Additive Manufacturing. My thanks go to Geoffrey Rivers, for his insane ideas and co-first-authorship on my first ever paper, and to Jonty Austin, who was first to welcome me to Nottingham and also taught me everything about electronic measurements. My apologies go to Mark East, Mark Hardy, and Adam Whitbread, the formidable lab technicians, for the constant badgering to fix whichever machine I had broken that week. Further, thank you to Mirela Axinte, Flavia Guzman Villarroel, Kerri Lindley, and Yuan Li, for their ability to navigate the labyrinthine maze of paperwork and form filling that is the University of Nottingham's bureaucracy: quite

literally nothing would have happened without you. I would also like to thank everyone who I've worked with over the years: Thomas Girerd, Sebastien Faron, Jisun Im, Negar Gilani, Yinfeng He, Robyn Worsley, Anil Bastola, Ashleigh Murray, Anna Lion, Francisco Reyes Luna, Simon Attwood, Tien Quach, Charlie Heaton, Ricky Wildman, Alexandra Foerster, James Caruana, Chris Strong, and Weitong Xiao. It's been a pleasure.

My thanks also go to Craig Sturgess, Matt Hawthorne, Jasmeet Kaur Hayre, Ian Halliday, and Le Ma for a fun three months of building a new printer together, and all of the support that came afterwards as well. I'd also like to acknowledge the work and collaborations with Mike Fay, Chris Parmenter, and James Kerfoot of the Nanoscale and Microscale Research Centre (nmRC) for their incredible expertise; Thomas Whittaker and Will Whittow of the University of Loughborough for the magic they perform on antennas (not antennae!); Nathan Roberts, Adam Thompson, and Ahmet Koca of the Manufacturing Metrology Team for their excellent analysis; and Esme Ireson, Paul Cooling, and Long Jiang of Boots Science Building for their superb training. I also acknowledge the support and funding of the University of Nottingham and the EPSRC.

Finally, I want to thank my family and friends, especially my mum, dad, and sister Gwen, whose unwavering encouragement, belief, and love are the reason I am in any way who I am today. Lastly, I want to thank Teju whose optimism and care kept me sane, and whose ambition and drive helped me to find my own.

Contents

List of Acronyms and Variables

ACRONYMS

µSLA = micro-stereolithography

2/2.5/3D = 2/2.5/3 dimensional

ABS = acrylonitrile butadiene styrene

ACMO = 4-acryloylmorpholine

AFM = atomic force microscopy

AJP = aerosol jet printing

AM = additive manufacturing

aSi = amorphous silicon

BJ = binder jetting

BSE = backscattered electrons

C=C = carbon-carbon double bond

C=O = carbon-oxygen double bond

CDLP = continuous direct light processing

CRE = coffee ring effect

CSI = Coherence scanning interferometry

DLP = direct light processing

DLS = dynamic light scattering

DOD = drop on demand

DRIE = deep reactive ion etching

DSA = drop shape analyser

DSC = differential scanning calorimetry

DW =direct writing

EBAM = electron beam additive manufacturing

EBL = electron beam lithography

EBM = electron beam melting

ECG = electrocardiogram

ED = electrodeposition

EGDPEA = ethylene glycol dicyclopentenyl ether acrylate

EHD = electrohydrodynamic jetting

EM = electron microscopy

FFF = fused filament fabrication

FIB = focussed ion beam

FoV = field of view

FTIR = Fourier-transform infrared spectroscopy

GPS = global positioning system

HTL = high temperature resin by Boston Micro Fabrication

IJP = inkjet printing

$Ink_{Ag,ANP}$ = silver nanoparticle ink DGP 40LT 15C by ANP

$Ink_{Ag,ND}$ = silver nanoparticle ink AgCiteTM90072 by Nano Dimension

$Ink_{Ag,XTPL}$ = silver nanoparticle ink Nanoink IJ36 by XTPL

$Ink_{Di,ACMO}$ = dielectric ink with ACMO

$Ink_{Di,EGDPEA}$ = dielectric ink with EGPDEA and TCDMDA

$Ink_{Di,ND}$ = dielectric 1092 ink by Nano Dimension

$Ink_{Di,TPGDA}$ = dielectric ink with TPGDA

IPA = isopropyl alcohol

IR = infrared

ITP = indium tin oxide

LDM = lights-out digital manufacturing

LED = light emitting diode

LEND = laser engineered net shaping

LOM = laminated object manufacturing

LR = lateral resolution

MJ = material jetting

MJF = multijet fusion

NA = numeric aperture

NP = silver nanoparticle

OtG = Off the Grid

PμSLA = projection micro-stereolithography

PCB = printed circuit board

PEDOT:PSS = polymer poly(3,4-ethylenedioxythiophene)

PET = polyethylene terephthalate

PHA = printhead assembly

PID = proportional-integral-derivative

PL = photolithography

PLA = polylactic acid

PS = phase shift

PTFE = poly(tetrafluoro ethylene)

QD = quantum dots

SEM = scanning electron microscopy

SEM = secondary electrons

SESI = secondary electron-secondary ion

SLA = stereolithography

SLM = selective laser melting

SLS = selective laser sintering

STL = 3D object file, literally "stereolithography"

TCDMDA = tricyclo[5.2.1.02,6] decanedimethanol diacrylate

TEM = transmission electron microscopy

TEM = transverse electric

TGA = thermogravimetric analysis

TPGDA = tri(propyl glycol) diacrylate

TRL = technology readiness level

UV = ultraviolet

Vis = visible light

WG = waveguide

VARIABLES

A = projected surface area

Ac = cross sectional area

Bo = Bond number

D = translational diffusion coefficient

d = diameter

D_{con} = diameter of the surface area in contact with drop

d_H = hydrodynamic diameter

D_i = initial drop diameter

F = frequency

f_n = nominal jetting frequency

F_r = refinement factor

f_r = refined jetting frequency

g = gravitational field strength

k = Boltzmann constant

L = nozzle diameter

$L_{a/b}$ = inner/outer distance between terminals

n_L = number of layers

n_z = wavenumber

Oh = Ohnesorge number

p = horizontal pixel coordinate

P_h = purge pressure

P_{ink} = ink pressure

P_z = power density

q = vertical pixel coordinate

R = resistance

r = radius

R_{4T} = 4 terminal resistance

R_c = contact resistance

Re = Reynold number

Sa = arithmetic mean height surface roughness

S_n = nominal drop spacing

Sq = squared mean height surface roughness

S_r = refined sdrop spacing

T = temperature

t = thickness

$\tan \delta_E$ = electric loss tangent

$\tan \delta_M$ = magnetic loss tangent

T_g = glass transition temperature

T_h = printhead temperature

T_{sint} = sintering temperature

t_{sint} = sintering time

T_{sub} = substrate temperature

V = drop velocity

$V_{image,i}$ = value if the i^{th} pixel in an image

V_{max} = maximum voltage

V_{total} = total window value

$V_{window,i}$ = value of the i^{th} pixel in a window

We = Weber number

Z = printability figure of merit

$z(x,y)$ = sample height

γ_{IFT} = surface tension

γ_r = shear rate

Δ_{centre} = on-centre gap between lines

Δ_{drop} = smallest separation between printed lines

δ_{drop} = median distance between drop centre and the fitted shape

δ_{layer} = layer offset

ε_r = relative dielectric constant

η = dynamic viscosity

θ_{eq} = equilibrium contact angle

λ_z = wavelength

μ_r = relative magnetic susceptibility

ρ = density

σ_{xyz} = conductivity in the x/y/z direction

τ = shear stress

1 INTRODUCTION

Inkjet printing (IJP), when employed as an additive manufacturing (AM) technique, is at the forefront of functional materials deposition in Industry 4.0, whilst simultaneously struggling with historical baggage from its graphical-printing origins. IJP involves the accurate positioning of a small fluid droplet (1-100 pL) onto a substrate, where it subsequently transforms from a liquid to a solid. With the first practical patents for graphical IJP appearing in 1951, the technology grew into widespread use by the end of the twentieth century [1]. It saw a range of applications, particularly with smaller print runs which require customisation between batches, such as sell-by dates, tailored packaging, and desktop printing [2]. Graphical IJP could rely on the ink being carried by the paper on which it was printed, as well as the fact that a single missed drop or a small amount of aliasing was likely to be unnoticeable to the human eye. Development of inks containing materials that can detach from the substrate and printheads which can consistently jet them has allowed the technology has since branched out into additive manufacturing (AM). IJP is now considered a promising approach for depositing a wide range functional materials [3] – including polymers [4–8], metals [9–14], ceramics [15], and low-dimensional materials [16–19] – for many types of device encompassing ceramic components [20], rate-controlled drug delivery [21], sensors [22–24] and transistors [25–28], including multi-material structures [29–31]. Compared to other AM techniques, it is particularly scalable, with multiple nozzles allowing for high throughput rates [32]. However, the functionality of the final product is still highly sensitive to missed drops and aliasing artefacts.

In recent years there have been considerable achievements in the field of printed electronics, as high-performance materials are made compatible with the IJP process [3]. Conductive materials form the basis of these devices in electrodes,

contacts, and interconnects. Development of these conductive inks for IJP started the possibility of printed electronics, with research focussing on reducing resistivity, refining resolution, and expanding substrate compatibility. Several companies, such as Elephantech [33], PV Nanocell [34], BotFactory [35], and NanoDimension [36] now offer custom-built printed circuit boards (PCBs), either to-order or in-house.

The current industrial frontrunner in geometric complexity is the Dragonfly LDM® (Lights-out Digital Manufacturing) 2.0 by Nano Dimension [36]. It simultaneously prints a polyacrylate dielectric alongside a silver-nanoparticle-loaded ink to produce PCBs with integrated componentry, antennas, transformers, and electromagnets. The dielectric is cured by an ultraviolet (UV) lamp to act as a matrix that supports the conductive silver shapes, which are sintered by a heated stage and infrared (IR) lamp.

The major limitation of three dimensional (3D) IJP is its inability to manipulate the third, vertical dimension. Current research, with few exceptions, tends to print less than 100 μm high, and often has little variation in geometry in the third dimension, essentially being limited to heterostructures, or 2.5D printing. The causes for this are two-fold: anisotropy of printed material properties and the liquid nature of the ink.

Anisotropy is inherent to IJP: material is deposited in a line along the primary printing direction, the lines merge into layers along the secondary direction, and then layers stack in the vertical (z) direction. The anisotropy can be mitigated by optimising process parameters (e.g., substrate temperature, in-situ exposure to UV or IR, and post-print sintering), but the ink composition is also a major driving factor [37]. The liquid nature of jettable inks causes unsupported overhanging – and often vertical – surfaces to not hold up during printing [38,39] unless solidification can occur more rapidly than liquid flow [40,41]. The Dragonfly printer utilises a high-silver-content

ink, which increases the layer thickness and therefore enables more verticality in their prints, and a dielectric ink which is highly temperature-stable, which increases viable post-processing temperatures. Further, the two-ink system allows for more complex geometries by embedding silver structures in the supportive dielectric matrix. Unsupported overhangs still cannot be manufactured, however.

The work presented in this thesis develops inkjet printing extended into a truly 3D additive manufacturing process of materials for electronics with greatly enhanced resolution. A new methodology for improved control over lateral drop placement, "Off the Grid", and a novel ability to produce complex 3D silver structures without support opens up a new world of possibilities for the types of devices that can be printed with IJP, including metamaterials, antennas, and battery electrodes.

- Chapter 1 provides an introduction and overview of the chapters contained in the thesis.

- Chapter 2 contains a literature review on additive manufacturing of functional materials, particularly those that pertain to high resolution electronics. It also compares the capabilities and existing work of several techniques for the printing of specific devices in 3D. After also considering their relevance to industrial adoption, inkjet printing is chosen for this avenue of work, so the review concludes with technical details of the process and requirements of this technique.

- Chapter 3 outlines the aims and objectives of the thesis.

- Chapter 4 details the materials and methods used in the pursuit of 3D inkjet printing, including the particulars of the equipment used for the printing and various characterisation methods for the behaviour and chemistry of the inks prior

to printing; how post processing affects the material properties of the prints; and the overall performance of devices.

- Chapter 5 presents the results of this ink characterisation, such as the printability of the inks, the nanoparticle construction of the silver nanoparticle inks and their basic conductivity. The material behaviour of several dielectric inks are also discussed to ascertain the most suitable one for both multi-material processing and as a dielectric medium.

- Chapter 6 reports on Off the Grid, a novel method for increasing the resolution of inkjet printing without requiring hardware upgrades to the printer. The chapter goes into detail about the working principles and efficacy of this method which removes the aliasing error usually present in all inkjet printers and goes on to demonstrate greatly improved fidelity for several functional designs.

- Chapter 7 presents truly 3D printed structures based on self-supporting micropillars. The growth mechanism for these pillars is investigated, where it is shown that they can self-support even when overhanging, allowing for complex strut-based lattices to be created. 3D structures using floating silver elements embedded in a dielectric matrix are also presented for use in GHz communications.

2 LITERATURE REVIEW

2.1 Additive Manufacturing of Functional Materials

Additive manufacturing (AM) is a technique for processing material into a desired geometry by successive deposition of material, often layer-by-layer [42]. There is a huge variety of AM processes (**Figure 2.1**), covering a wide range of material types, length scales, and applications, with the shared major benefits of low material wastage, digitizable customisation, and increased design freedom [43]. For example, powder bed fusion can be used to construct polymers (e.g. nylon, poly(ether ether ketone) etc.) [44] and metals (e.g. steel, titanium alloys etc.) [45] for rapid prototyping, and production of end-use parts in the medical, automotive and aerospace industries. Under this classification, the term inkjet printing is not officially defined. However, it is commonly used to refer to material jetting techniques where the fluid being jetted is liquid at room temperature, be that the pure material or a suspension, thus excluding techniques such as wax or molten metal material jetting.

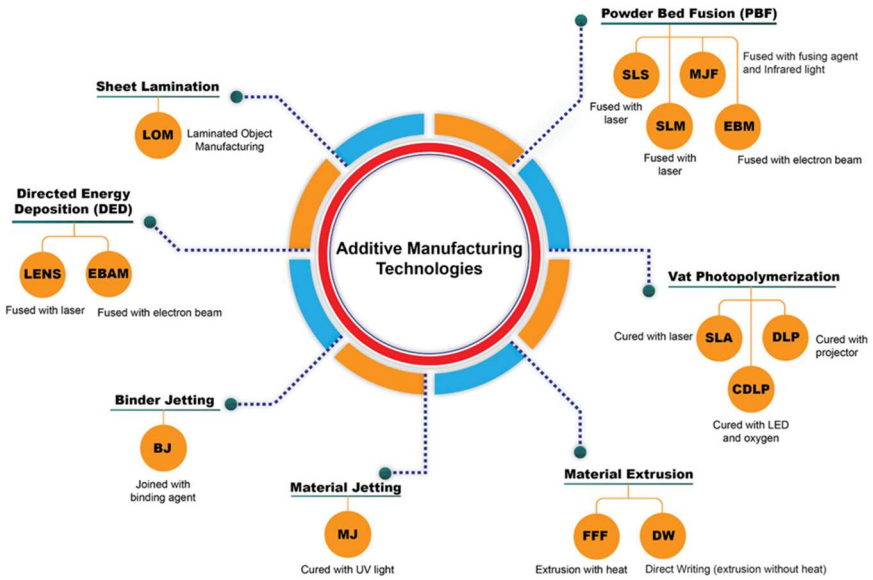

Figure 2.1: *The 7 types of AM as categorised by BS EN ISO-ASTM 52950-2021, which can be further split into varying subtypes, not all of which are represented in this single diagram. BJ = binder jetting, CDLP = continuous direct light processing, DLP = direct light processing, DW = direct writing, EBAM = electron beam additive manufacturing, EBM = electron beam melting, FFF = fused filament fabrication, LENS = laser engineered net shaping, LOM = laminated object manufacturing, MJ = material jetting, MJF = multijet fusion, SLA = stereolithography, SLM = selective laser melting, SLS = selective laser sintering. Figure reproduced from [46].*

AM can also be used to deposit functional materials, i.e. a material that has some function beyond its mechanical traits. For example, silver can be used for its high conductivity [2]; barium titanate for its ferroelectric properties [20]; graphene for chemical sensing [47] and beyond. Many such materials and applications exist, and often they will need to interface with electronics, to enable data capture, pass on signals, or simply be interacted with by users. Whilst functionalised materials can be deposited with many AM techniques [48–50], direct printing of functional materials for electronics have primarily been achieved through drop-on-demand (DoD) jetting or extrusion technologies [51]. Alternatively, a skeleton can be created with structural material which is then functionalised, e.g. by electrodeposition, as a post-process [52].

Electronic devices are used in virtually every aspect of day-to-day life and industry, but the conventional manufacturing methods used to make them are wasteful and inflexible. Additive manufacturing could revolutionise this wide-reaching sector to become more customisable, compact, and adaptive [51], as well as offering opportunities for device fabrication on traditionally unsuitable substrates.

It should be noted that, due to the resolution requirements, AM is unsuitable for the production of small components such as semiconductor microchips. Therefore, AME focusses on circuitry, antennas, and meta-structures. Discrete components can also be printed when there is a significant advantage such as improved sensitivity through complex geometry or miniaturisation through embedded components. Where these advantages do not exist, it is significantly cheaper, and often more reliable, to integrate traditionally- and additively manufactured components together. This can be seen with the current inroads that AM of electronics has made, currently being limited to rapid prototyping of small-run circuitry, and occasionally implementation in areas with complex geometric constraints such as aerospace or tailored medical devices.

2.1.1 Materials for Electronics

Electronics, at minimum, require a conductor to carry the current and an insulating material to hold it together without causing short circuits. However, more exotic materials are often required for whole devices to function: energy storage materials for a power source [18,53–55], high-dielectric-constant materials for manipulating electric fields [56,57], and an array of materials for sensing [58–61], optics [62–67], communications [68–70], energy [71–74], transistors [75–77] and more [78–81].

Sensors use a wide selection of materials, given their extraordinarily wide field of application [58,82]. Strain gauges, measuring changes in conductivity or capacitance as a sensor flexes, can be made with most forms of AM: silver-embedded polylactic acid (PLA) laid down with fused deposition modelling (FDM) [83], screen printing of graphite powder [84], direct ink writing (DIW) of carbon [85,86] or GaIn [87], inkjet printing of the conductive polymer poly(3,4-ethylenedioxythiophene) polystyrene sulfonate (PEDOT:SS) [60], and aerosol jet printing (AJP) of silver nanoparticles [88].

Similarly, temperature sensors have been produced from DIW of vanadium oxides [89] and IJP of silver [90–92], various carbon allotropes [93] (**Figure 2.2a**) and PEDOT:PSS [94] (**Figure 2.2b**). Carbon nanoparticles have also been inkjet-printed [95] and graphene nanorods embedded in PLA were deposited with FDM [96]. Biomedical sensors were also produced, from bionic ears made from hydrogels infused with silver nanoparticles [97] (**Figure 2.2c**) to wearable glucose sensors with acrylonitrile butadiene styrene (ABS) polymer microfluidic chambers [98] and gold-functionalised stainless steel DNA sensors [99]. In all of these cases, AM enabled sensor design which was on flexible substrates or utilised more efficient geometry which would be difficult to achieve with traditional processes.

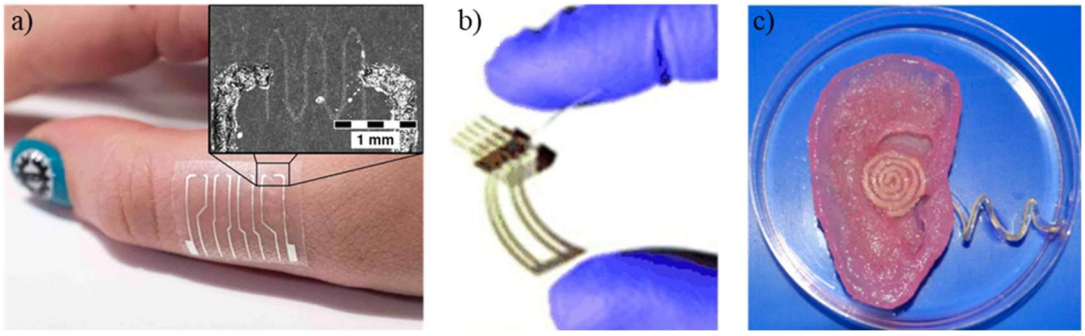

Figure 2.2: *Optical images of a variety of sensors,* ***(a)*** *a temperature sensor made from inkjet-printed PEDOT:PSS [93],* ***(b)*** *a vapour sensor made from inkjet-printed graphene oxide [94], and* ***(c)*** *a bionic ear made from alginate hydrogel and silicone embedded with silver nanoparticles printed with a custom material extrusion setup [97].*

For electronics, energy is generally stored in batteries or supercapacitors, i.e. as electrochemical energy. Since these are inherently multimaterial (anode/cathode/ electrodes and electrolyte), the AM battery literature is most focussed on inkjet printing (**Figure 2.3a**) [18,55,100–102], although direct ink writing is also well represented (**Figure 2.3b**) [103–105], with stereolithography (SLA) and (FDM) also being explored (**Figure 2.3c**) [106,107]. Battery technology is dominated by lithium-ion chemistry [108], although Zn [109] and Na [18] systems are also of interest. Generally, the cathode has been more fully researched, alongside current collectors [110]. For supercapacitors, graphene oxide and other carbon derivatives are popular choices for the electrodes (**Figure 2.3d**) [111,112], whereas there is a greater range of materials for the electrolytes [113]. AM, therefore, is uniquely advantageous in energy storage for its ability to produce complex structures with very high surface-to-volume ratios, or tailor the net shape to fit into new device forms.

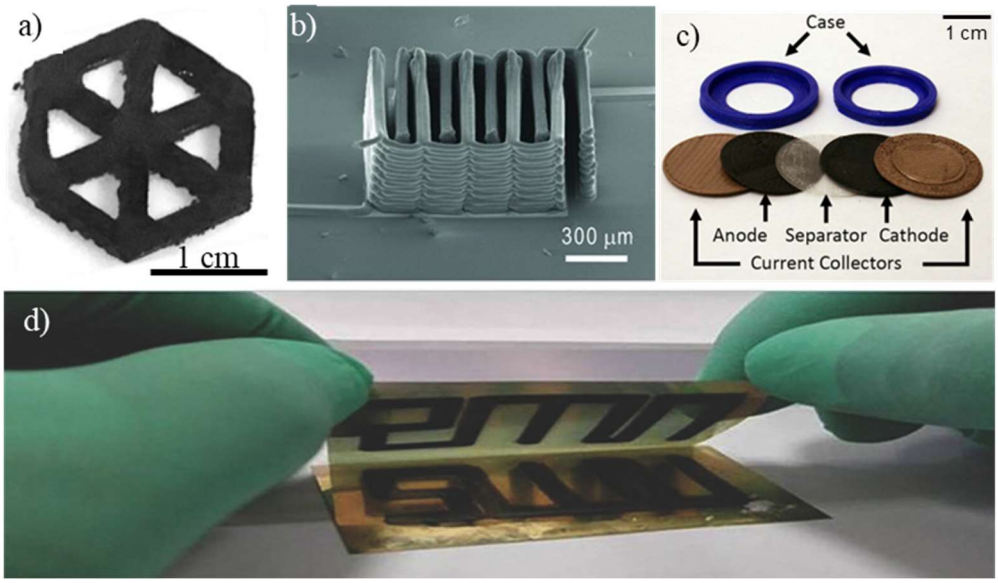

Figure 2.3: *Image of* ***(a)*** *a MoS_2-graphene aerogel anode for a sodium battery, manufactured by IJP, reproduced from [18],* ***(b)*** *interdigitated LTO/LFP battery electrodes made by DIW, reproduced from [105],* ***(c)*** *a fully FDM-printed lithium-ion battery, reproduced from [107], and* ***(d)*** *an inkjet-printed graphene supercapacitor, reproduced from [114].*

Antennas for wireless communication are very sensitive to their structure [115], which makes them prime candidates to exploit the geometric freedom which comes with AM [70]. For example, lenses for enhancing 28 GHz antennas can be made with FDM of PLA (**Figure 2.4a**) [49] and many other microwave antennas are made from silver on a dielectric substrate (**Figure 2.4b**) [69,71,116,117], although graphene has also been explored [118,119]. They can often double as energy harvesters [71], although dedicated energy harvesters such as solar cells have also been printed (**Figure 2.4c**). These use a variety of materials, including PEDOT:PSS [120], graphene [121] or silver [122] electrodes, ZnO as an electron transport layer [120,122] and anti-reflective Si-QD coatings [123], with the optically functional layer commonly being perovskite nanoparticles [124,125] or polymeric [120–122].

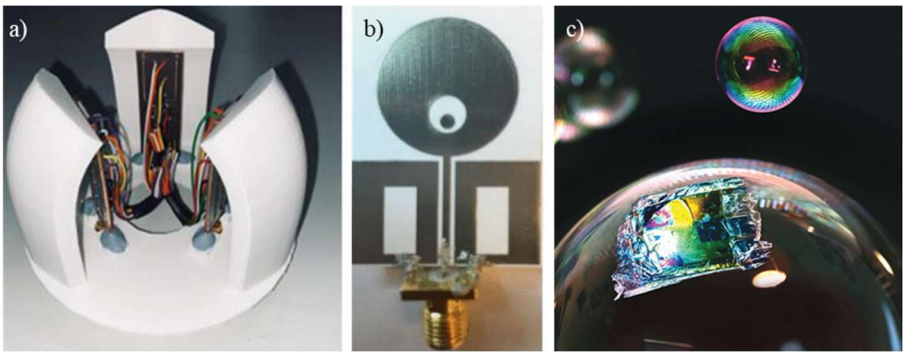

Figure 2.4: *Photographs of* ***(a)*** *a lens array for a 28 GHz slot antenna made from FDM of PLA, reproduced from [49],* ***(b)*** *a wideband 1.66–56.1 GHz monopole antenna made from inkjet-printed silver, reproduced from [116], and* ***(c)*** *a fully inkjet-printed ultra-light solar cell supported on a bubble made from various materials, reproduced from [122].*

Several of the devices discussed in this chapter have been multimaterial, where additive manufacturing processes different materials with properties that are beneficial in different parts of the device. Particularly, many include conductive silver traces to connect the device to a data logger [93,95,109,118,120]. Some designs, such as the FDM-printed lithium battery [107], can have their separate parts printed individually for manual assembly. Ideally, however, the device would be manufactured already assembled, which requires simultaneous processing of multiple materials. This adds complexity due to different layer heights of different materials, intermixing, delamination, and varying processing environments (e.g., temperature or presence of oxygen). Some of these issues can be solved with heterostructure geometries, where materials can be deposited sequentially rather than simultaneously, as demonstrated by the fully-inkjet-printed solar cell [120]. This lessens the requirement on strict layer height matching, but the challenges of mixing, delamination, and processing environment must still be met. A recent study showed that intermixing of graphene flakes and hexagonal boron nitride degraded the performance of an all-inkjet-printed field effect transistor [126]. The ultimate goal for full geometric freedom is the ability to print all materials simultaneously as needed, allowing each one to support the other in complex, 3D structures. This would facilitate novel or improved functionality, e.g. with antennas and electrodes, and compact assemblies when printing entire devices.

2.1.2 Geometric Complexity: High Resolution and True 3D

The geometric capabilities of a given additive manufacturing technique are a defining feature of the process, and usually independent of the material being processed. The highest resolution techniques which are also capable of printing a range of materials are inkjet printing, aerosol jetting, and direct ink writing, with positive feature sizes in the 10s of microns, and placement control in the single microns: a resolution which is acceptable for a wide range of devices, including microwave antennas, high-density circuitry, and a variety of sensors [51]. Whilst there are other techniques with much greater resolution (for example, two-photon stereolithography [127]), they tend to be too limited in material selection, multimaterial capability or total build size to be useful industrially. Some devices which would benefit from more complex 3D geometries include electrodes [128], metamaterials [129], and antennas [115].

In brief, inkjet printing (**Figure 2.5a**) ejects a single drop of ink on demand, which spreads out on impact with the substrate to diameters of 10-100 μm [130]. The positional accuracy of deposition is on the order of 1 μm, but due to the way data is processed for drops to merge together, there is usually significant aliasing leading to quantisation of drop placement in the 10s of microns, except for highly customised systems [40]. Once on the substrate, the ink is pinned in place, usually by evaporating away the carrier solvent or via a chemical reaction such as UV curing. The layer height varies greatly, from 10 nm – 1 μm [126,131], depending on the fluid dynamics, solidification mechanism, and loading of the ink. Several adjustments to the inkjet printing processes target the fluid dynamics to increase this lateral resolution, such as inter-layer plasma treatment to tightly control droplet flow, allowing for positional control down to 100 nm [132] or utilising an extreme coffee-ring effect to produce

double-lines of single-micron thickness [133]. However, these methods limit the geometric flexibility that is the main strength of additive manufacturing.

Aerosol jet (**Figure 2.5b**) atomises an ink containing the functional material into liquid drops of 1-5 μm diameter, which are carried by an annular sheath gas onto the substrate, which can focus the stream to a line width of 10-100 μm with a layer height as low as 0.1 μm. The drops are small enough that the fluid dynamics of spreading are negligible [134]. Direct ink writing (**Figure 2.5c**) extrudes material through a nozzle onto the substrate in a continuous line, either as a slurry which can be laser sintered to immediately solidify it [135] or as a liquid which simply cools [136] or develops a solid oxide coating as it leaves the nozzle [137].

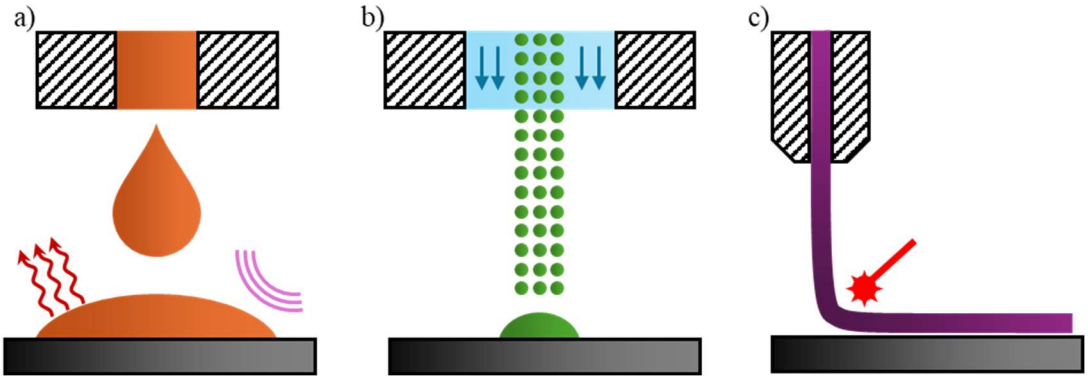

Figure 2.5: *Schematics for the deposition methods of* ***(a)*** *inkjet printing, where a piezoelectric element (black stripes) squeezes a drop of ink (orange) onto a substrate, where it is solidified, for example by UV irradiation (purple) or evaporation (red arrows),* ***(b)*** *aerosol jetting, where a sheath gas (light blue) carries aerosolised particles (green) through a nozzle (black stripes) onto the substrate, and* ***(c)*** *direct ink writing, where a continuous line of viscous ink (purple) is extruded out of a nozzle (black stripes) onto the substrate, where it solidifies due to cooling, evaporation, oxidation or laser (red) sintering.*

The liquid nature of the ink in inkjet printing requires that the drop be pinned or otherwise restricted from flowing very quickly, lest the print become a puddle. By ensuring rapid evaporation with a high-temperature substrate, individual free-standing pillars have been printed from metal nanoparticles. For example, pillars with a diameter ~100 μm, heights up to 1.5 mm, and vertical conductivity σ_z = 40 Ω^{-1} m^{-1} were printed from AuNPs on a substrate at temperature T_{sub} = 70 °C (**Figure 2.6a**) [138], and pillars with a diameter of ~200 μm and a height of up to 10 mm were

produced from AgNPs (T_{sub} = 60 °C, $\sigma_z = 3 \times 10^3$ Ω^{-1} m^{-1}, **Figure 2.6b**) [41]. Overhanging features allow for a hugely diverse range of shapes, including helices and bridge interconnects (T_{sub} = 80 °C), but have thus far required customised setups to make a single pillar at a time (**Figure 2.6c**) [40]. IJP produces anisotropic silver structures, where insulating ligands accumulate between the layer; horizontal electrical conductivity is around $\sigma_{xy} = 8 \times 10^6$ Ω^{-1} m^{-1} with the proper post-processing conditions, with vertical conductivity three orders of magnitude lower [37].

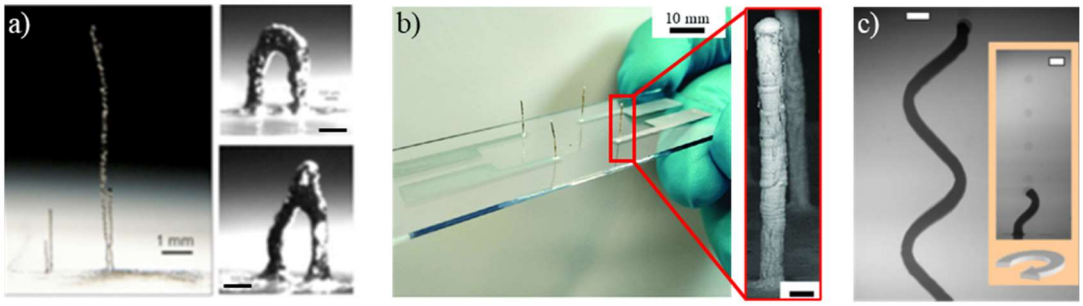

Figure 2.6: *Optical images of metal nanoparticle pillars produced by inkjet printing, using* ***(a)*** *gold nanoparticles to create individual wires (left) and bridge connections (right, scale bar = 100 µm), reproduced from [138],* ***(b)*** *silver nanoparticles for vertical interconnects (with an inset of an SEM image of a single pillar, right, scale bar = 200 µm), modified from [41], and* ***(c)*** *silver nanoparticles to create self-supporting overhanging structures, such as helices with a custom rotating substrate holder (both scale bars are 100 µm), reproduced from [40].*

The most developed and complex set of structures to date have been produced by AJP. Silver micropillar arrays have been produced (**Figure 2.7a**) [139–141], which were used as the basis for strut-based extended lattices, although their electrical conductivity was not reported (**Figure 2.7b**) [141,142]. However, aerosol-jet-printed silver is reported to be approximately half as conductive as inkjet-printed silver [134].

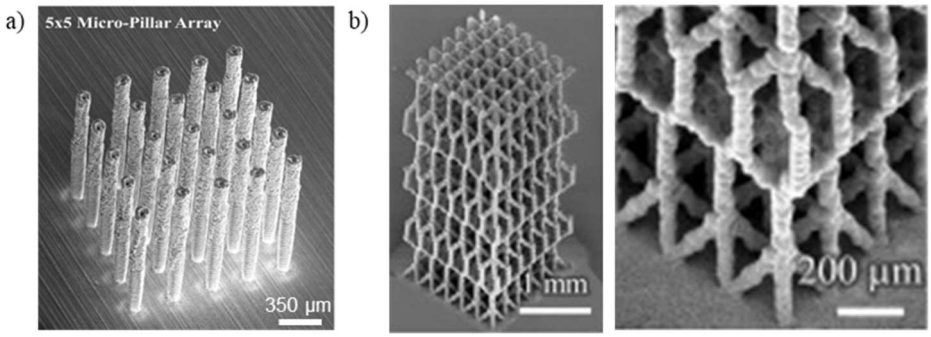

Figure 2.7: *SEM images of AgNP structures manufactured with aerosol jet printing.* ***(a)*** *Vertical micropillar arrays, reproduced from [139], and* ***(b)*** *self-supporting lattices, reproduced from [142].*

Direct ink writing (DIW) of the liquid metal InGa can take advantage of the outer oxide layer rapidly forming a solid skin which stops the liquid spreading, to produce impressive self-supporting structures several millimetres tall and with < 2 μm trace width (**Figure 2.8a**) and conductivity $\sigma = 3.4 \times 10^6\ \Omega^{-1}\ m^{-1}$. However, it is limited to a single nozzle and is best suited to designs which can be formed with a single continuous line [137]. Silver can be similarly printed when combined with rapid laser sintering directly at the nozzle (**Figure 2.8b**), although it has a lower conductivity of $\sigma = 1.9 \times 10^5\ \Omega^{-1}\ m^{-1}$ [135]. More recently, DIW of Field's metal achieved similar geometric results and a conductivity of $\sigma = 2 \times 10^6\ \Omega^{-1}\ m^{-1}$, with a lower resolution of 100 μm trace width to achieve greater production rates, demonstrating applications in temperature sensing, antennas, and metamaterials (**Figure 2.8c**) [136].

Figure 2.8: *Direct ink writing of conductive metals in 3D shown in* ***(a)*** *an SEM image of InGa 3D circuitry, both scale bars = 100 μm, reproduced from [137], and optical images of helical antennas made from* ***(b)*** *laser-sintered silver, reproduced from [135], and* ***(c)*** *Field's metal, reproduced from [136].*

Micropillar arrays are a common starting point for exploring 3D geometry, and other materials and techniques have also been explored, including ones outside of additive manufacturing (**Table 2-1**), which can then be extended to more complex geometries (**Table 2-2**), and are tabulated here for completeness. However, only the three techniques discussed above have the combination of resolution, material properties, and geometric freedom required for successful integration into electronics.

Table 2-1: *Overview of micropillar arrays. DRIE = deep reactive ion etching, EBL = electron beam lithography, EHD = electrohydrodynamic jetting, HTL = a resin by Boston Micro Fabrication, PL = photolithography, µSLA = micro-stereolithography. Diameter ranges on cones indicate top/bottom radii. Other ranges indicate multiple samples within that range were fabricated.*

Material	Array Dimensions / µm			Shape	Fabrication Method	Application	Ref
	Diameter	Height	Spacing				
GaAs/AlGaAs	2-5	10	5.5	Cylinder	EBL	Subwavelength THz laser	[143]
Si	10-40	8-10	4.5	Cylinder	PL	Cathode for photoelectrochemical reactions	[144]
Si	2	2	5	Cylinder	PL	Cathode for photoelectrochemical reactions	[78]
Si	4.4-2	4.5	5.2	Cone	PL	Near-infrared LED	[145]
TiO_2	2.5	10	10	Cylinder	PL stamp	Photocatalyst	[146]
PVDF	10	20	4	Cylinder	PL stamp	Piezo energy harvesting or sensors	[147]
PDMS + Fe	400	3000	1000	Cylinder	Laser-drilled mould	Magnetically controlled manipulation surface	[148]
Si	10-20	5-100	50-200	Cylinder	PL	Voltammetric modelling test samples	[149]
Si	5	12	7.5	Cylinder	PL	Chromatography columns	[150]
PDMS	10	40	30	Cylinder	Mould made by PL	Flexible capacitive sensors	[151]
Si	80	40	100	Square	PL	THz absorption	[152]
Si	50-70	34-275	42-60	Circular & elliptical	PL	THz beam shaping	[153]
PDMS	100-50	100-500	200	Cone	Soft lithography	Biosensor	[154]
Ag	90	600	350	Cylinder	Aerosol jet	Recording electrical signals from tissue	[139,140]
Si	10	20	15-1000	Cylinder	DRIE	Controlling the Leidenfrost effect	[155]
Au	40	500	330	Cylinder	Inkjet	3D metal structuring	[40]
HTL + Cr/Cu	20	75	320	Square prism	µSLA	THz split-ring resonator	[156]
Ag	32	560	300	Cylinder	Inkjet	Electrodes for extracellular measurements	[157]
Ag	35	500	100	Cylinder	Aerosol jet	Precursor to micro-lattices	[141]
Au	0.05	0.85	0.2	Cylinder	EHD	Nanoantennae	[158]
PZT	75	1200	200	Cylinder	Inkjet	Photocatalysis	[159]
TiO_2	40	600	200	Cylinder	Inkjet	Photocatalysis	[159]
Si_3N_4	100	500	250	Cylinder	Inkjet	Mechanical sensing	[160]

Table 2-2: *Additively manufactured pillars or 3D structures with pillar-like geometries. Minimum feature size refers to smallest positive feature, such as pillar diameter or wall thickness. DIW = direct ink writing, ED = electrodeposition, EHD = electrohydrodynamic jetting, PLA = polylactic acid, PμSLA = projection micro-stereolithography, SLA = stereolithography.*

Material	Min. Feature size / μm	Max. Height / μm	Shape	Fabrication Method	Application	Ref
Au	40	500*	Cylinders, helices, bridges, zigzags	Inkjet	3D metal structuring	[40]
NOVA 3D resin + Ni/Cu/Co	50	1500*	Strut-based lattice	PμSLA + ED	Magnetic micro-bots	[52]
Au	3	20	Individual pillars	EHD	Recording cell action potentials	[161]
Ag	35	2260*	Strut-based lattice	Aerosol jet	Hierarchical materials	[141,142]
Ag	120	2200	Individual pillars	Inkjet	Vertical interconnects	[41]
InGa	2	2000	Self-supporting lines	DIW	3D circuitry	[137]
Field's metal	100	40,000	Helices, metamaterials	DIW	Sensors, antennae, signal processing	[136]
MiiCraft resin + Cu/Ni	300	50,000	Strut-based lattice	SLA + ED	Complex metallic architectures	[162]
Ag	1	800*	Various helices, butterflies	Laser-DIW	Flexible electronics	[135]
Ag	0.7	35	Pillars, walls	EHD	3D electronics	[163]
PLA	100	4000	Helices, woodpile	Solvent cast printing	3D architectures	[164]
Au	75	1350	Individual pillars	Inkjet	Microelectronics	[138]

The alternative to self-supporting structures is to simultaneously print a support material [38,39], although this is yet to be achieved in the literature by aerosol jet or DIW. The IJP PolyJet system by Stratasys is capable of printing multiple polymeric materials plus a soluble support material. This enables overhangs and hollow parts up to 200 mm tall [131]. However, material selection is limited to the proprietary polymers available from Stratasys. Outside of the PolyJet system, using a non-resorbable polymer in conjunction with a resorbable and drug-loaded polymer enabled customisable pills whose geometry determined the release rate of the drug [165]. Further, Saleh et al. [166] used a UV-curable polymer as a permanent support matrix for silver nanoparticle circuitry, reaching vertical print dimensions up to 3 mm. This concept is also used by the Nano Dimension Dragonfly printer, which is expanded upon in **Chapter 2.2.1**.

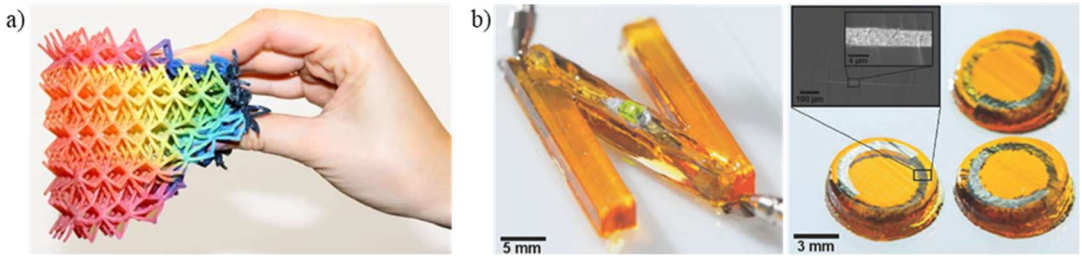

Figure 2.9: *Images of* ***(a)*** *a multicolour flexible lattice made from the Agilus 30 series of inks on the Stratasys PolyJet [131], and* ***(b)*** *3D circuitry made from silver nanoparticles in a UV-cured polymer matrix, reproduced from [166].*

2.2 Applications in Electronics

Electronics has a wide scope for maximising the usefulness of novel 3D geometries. This section presents current work on the most fundamental part of electronics, circuitry, as well as two classes of device that are particularly sensitive to their geometry: antennas and metamaterials.

2.2.1 Printed Circuitry

Electronic devices are circuitry comprised of microchips, passive components (resistors, capacitors etc.), and functionalised components (antennas, sensors etc.),

often connected with printed circuit boards (PCBs). Currently, PCBs are made by printing a photomask onto a photoresist to selectively etch copper film glued to an insulating substrate [167]. This is a well-established process, but not easy to extend into three dimensions. 3D IJP is the most mature alternative AM technology, creating PCBs by printing a conductive and an insulating material, building up layer-by-layer, and often including infrared- or post-sintering to increase conductivity.

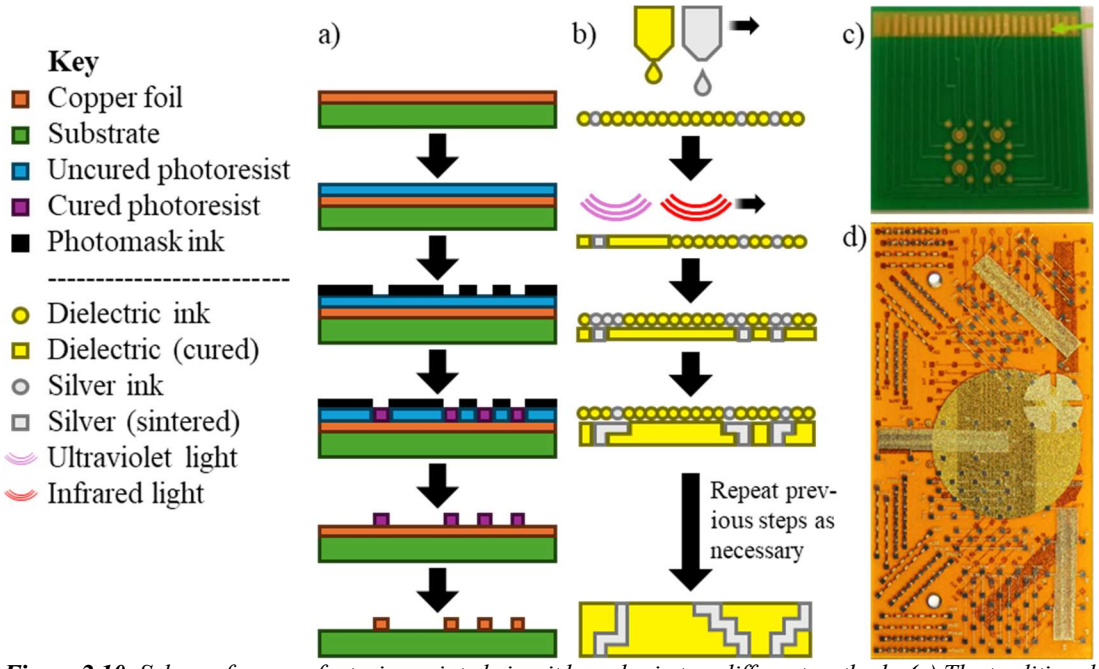

Figure 2.10: *Schema for manufacturing printed circuit boards via two different methods.* ***(a)*** *The traditional method starts with a copper foil adhered to a dielectric substrate, which is covered with a photoresist. A photomask is printed on top in the negative pattern of the desired circuitry, and the photoresist is cured in the places where the ink is not present. The ink and uncured photoresist are washed off, then the copper is etched away with an acid where it isn't protected by the photoresist. Finally, the cured photoresist is washed off. Optional extra steps could include repeating the process on the other side of the board and drilling vias to electrically connect the two sides.* ***(b)*** *3D inkjet printing uses two inks; a polymer precursor (often an acrylate monomer which is UV-cured into a polyacrylate) and a conductive ink (usually silver nanoparticles suspended in a volatile solvent). Individual drops are placed in a 2D layer such that adjacent drops of the same material merge with each other to form a continuous film. IR radiation or a heated substrate sinters the silver nanoparticles together, and UV radiation cures the dielectric. 2D layers are sequentially stacked to form a 3D PCB. The silver may be sintered further post-print to increase conductivity. Images of* ***(c)*** *a traditional PCB, where the arrow is pointing to contact pads to solder other electronics onto it, reproduced from [167] and* ***(d)*** *a 3D inkjet-printed PCB with an inbuilt circular antenna [168] are also shown.*

A primary challenge of all inkjet-printed metal nanoparticles is their inferior conductivity to bulk metal, and particularly the anisotropy of their conductivity (**Chapter 2.1.2**). The resolution (10s of microns) is also inferior to traditional methods such as lithographic etching [169]. DIW and AJP are not generally capable of

simultaneous multimaterial printing but exceed IJP in creating free-standing 3D prints (**Figure 2.7**, **Figure 2.8**), and have less conductivity anisotropy [170].

DIW is effective for small bridge interconnects which increase circuit density, which is synergistic with densely packed lines due to the lack of overspray or satellite drops [171]. It has also been explored for carbon circuitry, which is robust to flexing but has lower conductivity [172–175] compared with silver [176,177] (**Figure 2.11a, b**).

AJP is most useful where high geometric complexity is required without support, for example in electrodes or catalysis [142], but tends to have the most overspray and process instability which can cause short-circuiting [170]. However, it's large stand-off distance makes it ideal for printing conformable circuitry onto complex 3D objects [170], even with orthogonal surfaces [178] (**Figure 2.11c**).

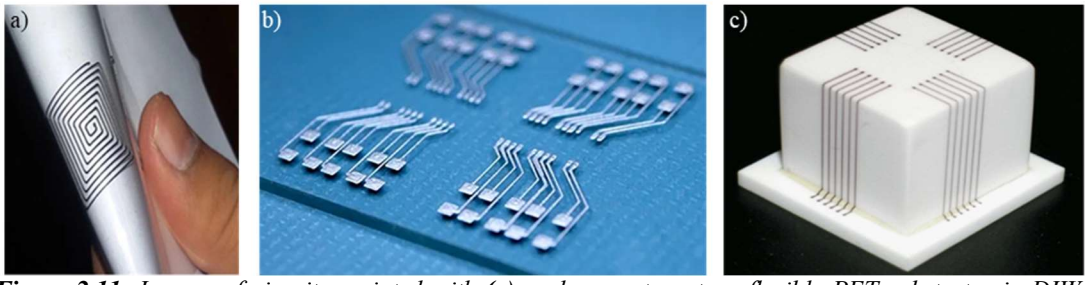

Figure 2.11: *Images of circuitry printed with* ***(a)*** *carbon paste onto a flexible PET substrate via DIW, reproduced from [174],* ***(b)*** *silver on a glass substrate via DIW, reproduced from [179], and* ***(c)*** *silver onto a ceramic cube via AJP, reproduced from [178]*

The most important consideration in circuitry is that of conductivity. Traditional manufacturing is generally capable of achieving near-bulk conductivity, often using copper due to its lower cost [51]. AM methods achieve lower conductivities (**Table 2-3: Comparison of conductivities for various material and methods.**), which would increase the power consumption of devices made in this manner. Optimised, complex pathways may reduce the total length which the current has to travel, which can reduce the overall resistance, but this effect will be minimal compared to the much larger

difference in overall conductivity. Therefore, the most successful AM methods in this regard utilise silver for higher conductivities, which has the downside of increased cost compared to copper.

Table 2-3: *Comparison of conductivities for various material and methods.*

Material	Manufacturing Method	Conductivity / Ω^{-1} m^{-1}	Reference
Copper	Traditional etching	6.0×10^7	[51]
Gold	Traditional etching	4.1×10^7	[2]
	IJP	3×10^6	[180]
Silver	IJP (horizontal)	8×10^6	[37]
	IJP (vertical)	8×10^3	[37]
	AJP	4×10^6	[134]
	DIW	1.9×10^5	[135]
InGa	DIW	3.4×10^6	[137]
Field's metal	DIW	2×10^6	[136]

2.2.2 Metamaterials and Antennas

The performance of antennas and metamaterials is influenced by their physical shape and structure, as well as by the individual materials from which they are made [115,181]. As such, they are highly frequency dependent and are designed to target selected frequencies or bands for an enormous range of functionalities.

This dependence on geometry makes them ideal candidates for additive manufacturing [70,129]. Devices operating with GHz-THz frequencies can utilise feature sizes of 10s of microns, and are used for communications, both terrestrially and in space [129], for which there are many applications where compact design from complex geometries (aerospace, handheld electronics etc.) would be of great benefit.

2.2.2.1 Antennas

Antennas are devices that convert between electromagnetic waves and electric current, in either or both directions. AM allows for the flexibility of design to miniaturise the size of the antenna without sacrificing bandwidth, gain, or directionality [115]. The resolutions of IJP, AJP, and DIW are most suitable for microwave or THz applications (**Figure 2.12**), with inkjet printing having the largest set of literature available.

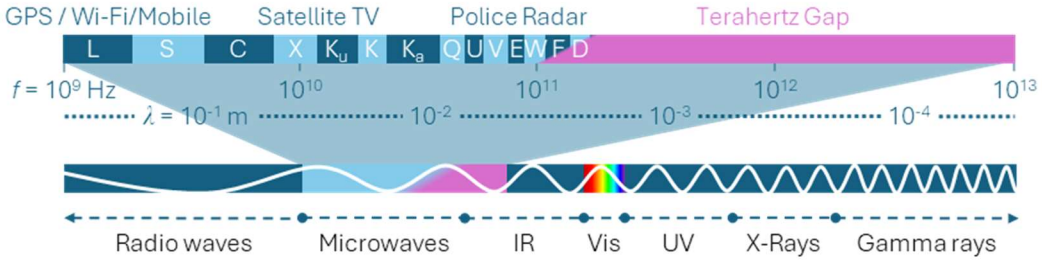

Figure 2.12: *Schematic of the microwave frequency communication bands, the terahertz gap, and where they both fit in the broader electromagnetic spectrum. The letter designations for the microwave bands are shown in white text, and at the top are a few applications in the approximate location for their frequency. The frequency (f) and wavelength (λ) for the top scale are also shown. GPS = global positioning system, IR = infrared, UV = ultraviolet, Vis = visible light.*

2D antennas are the simplest, having been printed with graphene via IJP [68] or silver via IJP [119,182], DIW [135], or AJP [183]. IJP can achieve 3D geometries by starting in the Polyjet printer to print a 3D polymer lens which complements a 2D IJP silver spiral antenna to achieve an overall gain of 4.6 dB in the X band [69]. The Polyjet system was also used to create a self-folding cube net onto which silver patches were printed with a Dimatix printer from Fujifilm. The hinges of the net were made with a shape memory polymer, causing the overall shape to fluctuate as the environmental temperature changed, creating a remote temperature sensor (**Figure 2.13a**) [71]. Foldable and flexible substrates can also enable a pseudo 3D antenna design with inkjet printing, with the additional bonus of internal space to fit extra electronics [184], or produce wearable antennas which can embed themselves in clothes or medical dressings [117].

AJP can utilise its large stand-off distance to print onto 3D surfaces that would be challenging for IJP. For example, an antenna designed around the curves of a fingernail can be created with AJP silver onto a fake nail to be worn as an identification tag (**Figure 2.13b**) [185], or inside a phone case as the primary antenna [186].

Similarly, DIW can print onto 3D surfaces if their topology can be pre-programmed into the movement of the dispensing needle. This allows minimally small L band antennas to be produced by depositing silver onto glass hemispheres (**Figure 2.13c**) [187] or into a wearable ring for K_u band operation [188]. As shown in **Chapter 2.1.2**, DIW is also capable of producing impressive free-standing helical antennas which are as small as is theoretically possible for operation at their chosen frequency (in these cases, L band [135] and C band [136].)

Figure 2.13: *Optical images of antennas produced by* ***(a)*** *IJP silver patch antennas onto an inkjet-printed shape-memory polymer, reproduced from [71],* ***(b)*** *aerosol jetting silver onto acrylic nails for identification antennas, reproduced from [185], and* ***(c)*** *direct ink writing silver onto a glass hemisphere to create an electrically small L band antennas, reproduced from [187].*

2.2.2.2 Metamaterials

A metamaterial is a structured material with a response, function, or property which arises due to the collective effects of the meta-atom elements that make up its structure that is not possible to achieve conventionally with an unstructured material. They often exhibit significant symmetry but can utilise a degree of controlled randomness. Generally, the overall scale of the meta-atoms determines a wavelength at which the metamaterial is most effective. The wave interacting with the metamaterial does not have to be electromagnetic, however, but could be acoustic, mechanical, or even

thermal (**Figure 2.14**). Examples are resonant structures which absorb select frequencies of light, materials with negative Poisson ratios, or acoustic lenses. The direct link between structure and performance makes them ideal candidates for additive manufacturing [189].

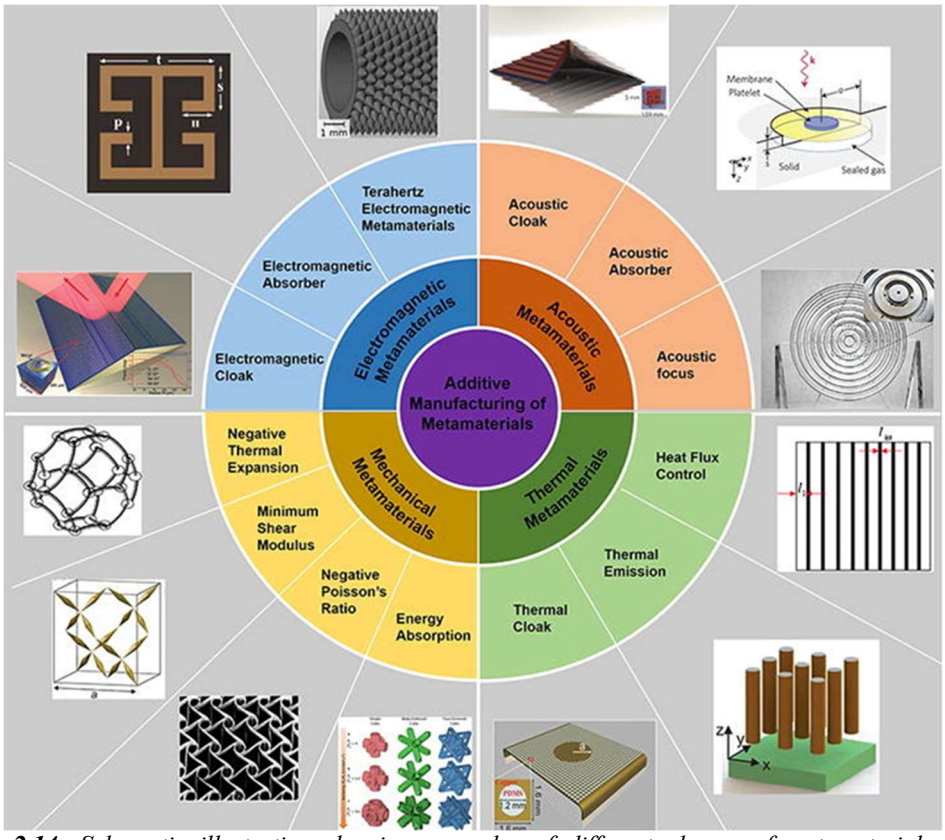

Figure 2.14: *Schematic illustration showing examples of different classes of metamaterial and the geometries of the meta-atoms that could make up their structure, reproduced from [189].*

2D resonators, such as split rings, are the simplest to create via techniques such as IJP, AJP, and DIW. They absorb electromagnetic radiation at specific frequencies depending on their geometry, and this resonant peak can be shifted slightly by various environmental factors, so they can be used as sensors. For example, inkjet-printed silver resonators (6 mm wide resonators with 500 µm traces) responded to the presence of ethanol to act as remote sensors in microfluidics channels [190,191]. They are also ideal for THz frequencies, with promising applications in medical imaging [192] and high-speed data transfer [193], but have traditionally required complex and costly photolithographic etching to manufacture [194]. Inkjet printing resonators is an

attractive option for the efficient absorption and reflection of these beams [152,156,194–196] (**Figure 2.15a**), although inaccuracies in the manufacturing process produces a less sharp response (full-width half-maximum increased 30% compared to samples fabricated via lithography) [197]. All-dielectric metamaterials are also used in beam-control, for example a waveguide for low-THz frequencies was printed on the PolyJet system [198]. AJP is similarly capable for such applications, although has been less studied, but one silver nanoparticle resonator was found to be comparable to traditional manufacture for tuneable band-stop filters in the 200-500 GHz range [199] (**Figure 2.15b**). DIW has also been used for the construction of resonators, using Field's metal to create a raised structure which acts as a band-stop filter between two patch antennas at around 2.45 GHz [136] (**Figure 2.15c**). AM has primarily benefited this field by providing a more cost-effective and flexible method to produce such resonators, which has previously required expensive photolithographic techniques otherwise.

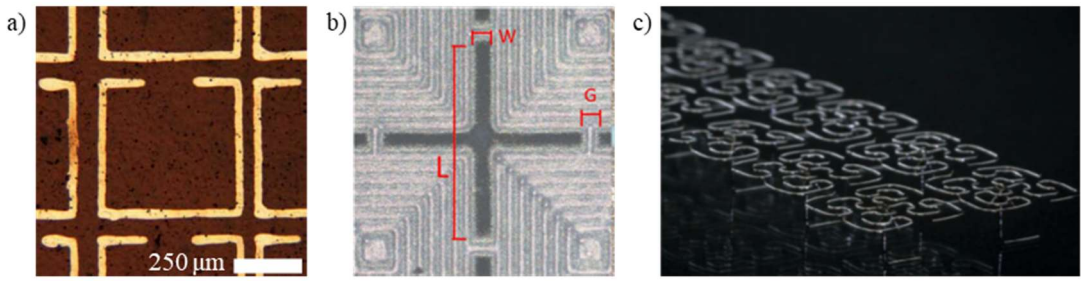

Figure 2.15: *Images of THz metamaterials produced by* ***(a)*** *IJP silver nanoparticles onto polyimide to create a 0.2 THz absorber, reproduced from [197],* ***(b)*** *AJP AgNPs onto ceramic for a 0.23 THz absorber (the height of the cross, labelled L, is 520 µm), reproduced from [199], and* ***(c)*** *DIW of free-standing Field's metal for a 2.45 GHz coupler (each square meta-atom is 8 mm across), reproduced from [136].*

There is limited literature on metamaterials produced via AM at this scale, despite there being many structures that are both feasible and potentially more desirable to produce via AM. For example, a Fresnel lens approach could enable focussing of THz beams [153]. Also of interest are photonic lattices – a subset of metamaterial which uses diffraction to create bandgaps for use in photonic traps, beam shaping, and optical

computing [181]. One design of photonic lattices that is suitable for AM uses pillars where the regular spacing and dielectric properties create a band gap of frequencies which are unable to pass through. Line defects can be introduced to allow these frequencies to pass through specific regions in a manner similar to an optical fibre, but where more complex behaviour can be enabled. Adding point-defects creates resonant cavities at highly specific frequencies, which – when combined with the line defects – cause the signal to jump to a different line defect, effectively creating a frequency-specific logic gate (**Figure 2.16a**) [181]. Analogous structures have been inkjet-printed from silver for electrodes, 40 µm in diameter and 500 µm tall (**Figure 2.16b, c**) [40]. Other structures analogous to different photonic lattices have also been produced, for example, woodpile structures have been produced via DIW from polyelectrolytes (200 µm line width, **Figure 2.16d-e**).

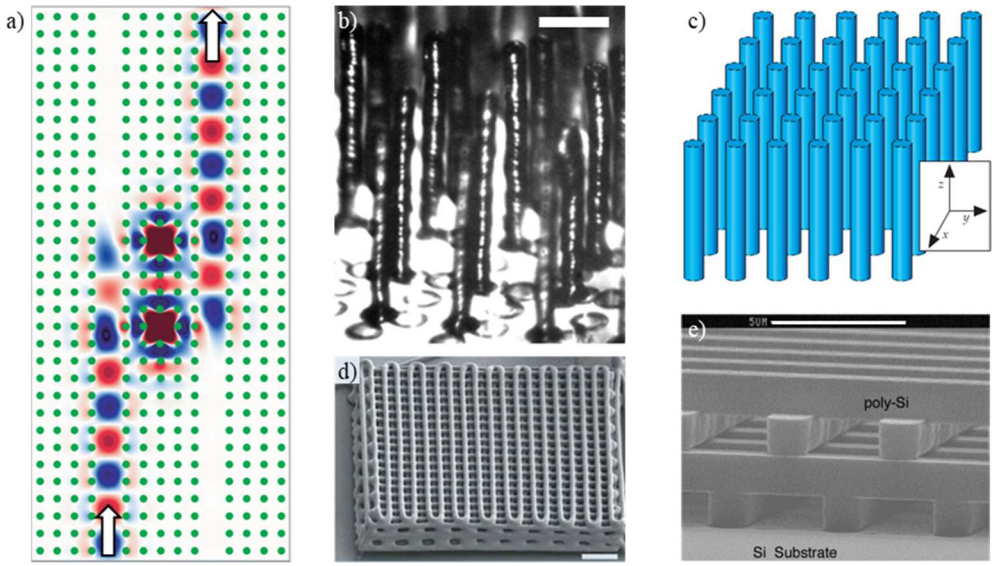

Figure 2.16: *Examples of photonic lattice designs, including* ***(a)*** *the simulated electric field of a wave going through a band pass filter based on a photonic lattice, reproduced from [181]. It shows a top view of pillars (green circles), arranged with an input and output port. The two gaps in the middle are resonant cavities which transfer the wave from the left line to the right if the wave has a frequency which resonates with the two central point defects. The red/blue shows the peaks/troughs of the electric field, which is vertically polarised. The arrows show the direction of travel. Also shown are* ***(b)*** *an optical image of silver pillars made by IJP (scale bar = 200 µm), reproduced from [40], which are analogous to* ***(c)*** *a schematic of a pillar-based photonic lattice, the basis for the design in (a), reproduced from [181], and* ***(d)*** *a woodpile structure made from DIW of a polyelectrolyte (scale bar 10 µm) made for a supercapacitor electrode, reproduced from [103], but which is analogous to the structure shown in* ***(e)*** *an infrared photonic woodpile lattice made by repeated etching and deposition of Si (scale bar = 5µm), reproduced from [200].*

2.2.3 Industrial Adoption

The benefits of additive manufacturing for electronics are clear, but for wider adoption into industry, the approach needs to have excellent material properties (e.g. conductivity), few geometric restrictions, and the ability to manufacture at scale. However, there are also clear limitations in comparison to traditional manufacturing methods, particularly reliability and conductivity. Very high resolutions are also difficult to achieve with AM, so semiconductor chips that require nanometre-scale resolutions are not possible. Furthermore, the flexibility of AM means that a more specialised manufacturing route will usually be cheaper and faster for large-scale mass production. Therefore, with the current state of AM, the use of AM must be justified based on the benefits outlined above, rather than being considered as a default manufacturing approach.

Additive manufacturing technologies capable of feature sizes below 100 μm tend to have a limited selection of compatible materials (for example, vat polymerisation and FDM techniques rely on relatively low loading of functional materials into a polymer matrix [83], or require post-processing such as plating [52,162]), or difficulties with large builds (for example, AJP has low deposition rates and experiences issues with process variability [201]). Despite this, progress has been made in the AM of complex 3D structures which span multiple length scales, from 10 μm features to overall build sizes of several millimetres.

The two main competitors in AJP for electronics (Optomec [202] and Cicor [203]) focus on complex designs and conformal printing with total print heights in the 10s of microns, although Optomec has demonstrated simple 3D structures up to 1 mm tall (**Figure 2.17a**) [204]. However, slow volumetric build speeds [201] and increased expense due to the nature of aerosol generation [134] make scalability challenging.

Similarly, the Voltera NOVA [179] is a DIW printer designed for printing flexible electronics in 2D (**Figure 2.17b**). Hummink is a new company reporting to achieve vertical micropillar structures with aspect ratios of up to 20 and XY tolerances of 0.44 µm, although no images of 3D prints > 200 µm were reported yet (**Figure 2.17c, d**) [171]. Further, the volumetric print speed is likely to be low due to only having a single nozzle, hence limiting its scalability.

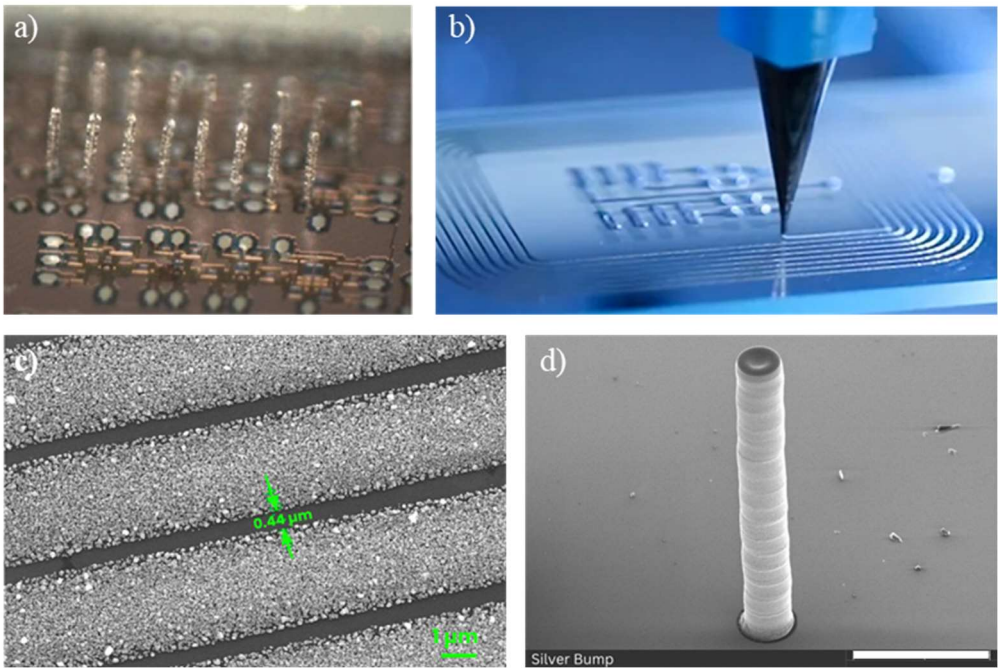

Figure 2.17: *Images of silver nanoparticles deposited by* ***(a)*** *Optomec's aerosol jet printer, showing pillars approximately 1 mm tall on a circuit board, reproduced from [204],* ***(b)*** *Voltera's NOVA DIW printer, reproduced from [179], and Hummink's DIW printer, with SEM images of* ***(c)*** *the minimum possible negative space achievable and* ***(d)*** *a 200 µm tall pillar (scale bar = 100 µm), reproduced from [171].*

Inkjet printing is the most mature technology, with a number of companies offering single printed circuit boards (PCBs) layer (Elephantech [33] and PV Nanocell [34], **Figure 2.18a**), and BotFactory offering 4-layer PCBs with included pick-and-place then soldering for microchips (**Figure 2.18b**) [35], which have potential for 2D or near-2D applications. The most advanced commercial 3D inkjet printer to date is the Dragonfly series made by Nano Dimension. It simultaneously prints silver nanoparticles and a UV-curable acrylate supportive matrix with a 35 µm resolution, and a maximum vertical height of 3 mm (**Figure 2.18c**) [205]. The silver is sintered

by the high substrate temperature, T_{sub} = 140 °C, along with an exposure to an infrared lamp for each printed silver layer. An extensive automated printhead maintenance system allows for consistent jetting throughout long prints, enabling the print times needed for manufacturing pieces larger than a few millimetres without catastrophic nozzle clogging. Originally developed for rapid design and production of custom PCBs, it has been successfully adopted for meta-lens antennas, the electronics for an optoelectronic neural interface, and an X-Band bandpass filter [168]. Nano Dimension report to already have several industrial partners, although mostly to use in rapid prototyping as opposed to end-stage products [168]. Further development is therefore needed at this stage, mostly due to cost and the need to fully understand the relationship between the manufacturing process and the final material properties.

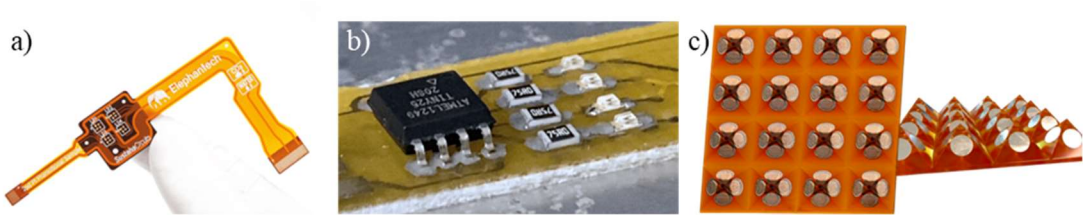

Figure 2.18: *Images of inkjet-printed silver from* ***(a)*** *PV Nano Cell, a single layer of silver printed onto a dielectric substrate, reproduced from [34],* ***(b)*** *BotFactory, where both silver and the dielectric are inkjet-printed, then the microchips are soldered in place all within the same machine, reproduced from [35], and* ***(c)*** *Nano Dimension, where simultaneously printing the silver and the dielectric allow for more complicated geometries, such as this sphere-antenna array [168].*

Inkjet printing has the highest TRL (technology readiness level) of the three technologies, in most part owing to its scalability: printheads with thousands of nozzles are used to increase the rate of deposition. It is also capable of simultaneous multimaterial printing with a maturity that neither aerosol jet nor DIW possess [134]. However, IJP of free-standing overhangs requires a custom setup which limits the industrial translation and scale of this approach. Therefore, significant work is needed to catch up with the geometric freedom of the other forms of additive manufacturing.

2.3 Inkjet Printing Process

There are three primary mechanisms that define the process of inkjet printing: droplet generation, droplet-substrate interactions, and droplet solidification [130]. In particular, the fluid dynamics of the ink place a significant restriction on the inks that can be used, which may vary slightly amongst specific printers, but are – for the most part – general to the process.

2.3.1 Droplet Generation

Drop-on-demand (DOD) piezoelectric printheads are the droplet-generators of choice for functional inkjet printing. They produce very little waste, can be chemically compatible with almost any material, and the waveform they produce can be easily tailored to optimise the jetting quality of a given ink. Typical jetting frequencies are around 10 kHz, with droplet volumes ranging from 2 to 100 pL [130].

To generate a droplet, the piezoelectric actuator creates a pressure wave in the fluid chamber held behind the printing nozzle which overcomes the surface tension of the fluid at the nozzle exit to eject a droplet. The precise droplet volume and ejection velocity depend on the waveform and printhead geometry in use [206]. The ejected droplet initially moves at high speed and continues to move as the driving pressure wave dissipates, creating a stretched-out ligament of ink joining the nozzle to the droplet. The droplet slows due to dissipative viscous forces, the increasing surface area of the stretching ligament, and some minor air resistance effects. Eventually the ligament breaks, and surface tension pulls the ejected ink into a sphere. The ligament may break into multiple droplets due to Plateau-Rayleigh instability (**Figure 2.19**), also known as satellite droplets, which can be avoided by careful selection of waveform parameters as well as particular attention to the ink's rheology.

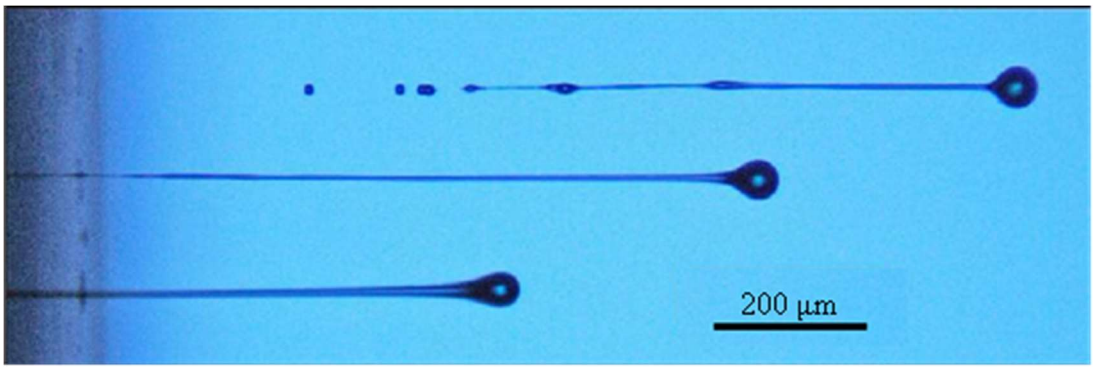

***Figure 2.19**: Ejected ink droplets showing the stretching of the connecting ligament and its break-up into satellite droplets. Reproduced from [207].*

2.3.2 Ink Rheology

Generating a stable droplet requires formulations with a specific range of ink properties and optimisation of printing parameters. Particularly important are the ink's density (ρ), surface tension (γ_{IFT}) and dynamic viscosity (η), as well as the drop velocity (V) and the nozzle diameter (L). These properties come together to define the dimensionless Reynolds (Re), Weber (We) and Ohnesorge (Oh) numbers:

$$Re = \frac{\rho V L}{\eta} \tag{2.1}$$

$$We = \frac{\rho V^2 L}{\gamma_{IFT}} \tag{2.2}$$

$$Oh = \frac{\sqrt{We}}{Re} = \frac{\eta}{\sqrt{\rho L \gamma_{IFT}}} \tag{2.3}$$

Re is the ratio of inertial to viscous forces, and We is the ratio of inertial forces to the surface tension. Oh incorporates the inertial, viscous, and surface tension forces together to characterise the ability of an ink to form acceptable droplets [2]. The reciprocal of Oh, labelled Z, was originally thought to need to exceed $Z = 2$ to generate stable droplets [208], but was later refined to the range of $1 < Z < 10$ through numerical simulations. A very viscous ink – such that $Z < 1$ – dissipates the energy of the pressure wave within a printhead, making it difficult to form droplets. Conversely,

if Z is too high then the primary ink droplet is accompanied by unwanted satellite droplets [130].

Further, the ink must be able to overcome its own surface tension to form a drop, which places a lower bound on *We* [209]. Finally, when the drop impacts onto the substrate it must stay as a cohesive drop rather than splashing. The specifics of drop-substrate interaction are covered in detail in **Chapter 2.3.3**, but in short, splashing occurs when the energy of impact is large enough that it can only be dissipated by the drop breaking into several, smaller drops to increase the total surface area [210,211]. **Figure 2.20** combines these restrictions to form a parameter space for printable inks.

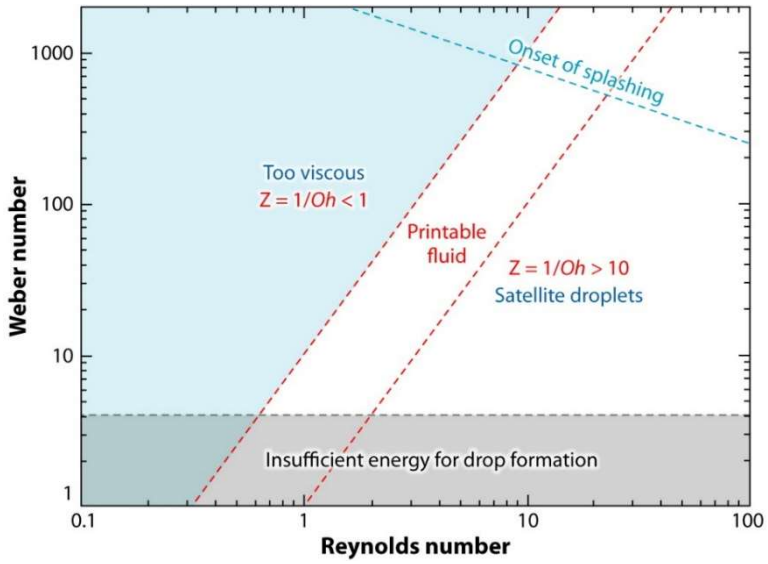

Figure 2.20: *Parameter space defining the Weber (We) and Reynolds (Re) numbers for a printable fluid. Re, We, and Oh (Ohnesorge number) are defined in equations (2.1)-(2.3). Figure reproduced from* [130].

Various studies have investigated acceptable ranges for ink rheology, with a viscosity η = 1-20 mPa s and a surface tension γ_{IFT} = 20-70 mN m^{-1} proving successful to be [80,212,213]. The popular Samba cartridge by Fujifilm suggests a viscosity η = 4-8 mPa s and a surface tension γ_{IFT} = 28-32 mN m^{-1}.

Many additives have been successfully utilised to achieve the desired rheological properties, such as ethylene/propylene glycol, glycerol, and polystyrene [214–217] for modifying viscosity, and surfactants such as surfynol and didodecyldiphenyl ether

disulfonate [218,219] to lower the surface tension. However, ink that satisfies the rheological requirements could still lead to clogging if large particles are present – typically particles larger than $1/50^{th}$ of the nozzle diameter should be avoided [220]. Further, agglomeration of nanoparticles must be avoided, which requires suitable stabilising ligands to be attached to their surface, often by specific surface functionalisation [221]. Metal nanoparticle inks are commonly used for their high conductivities and often require polymeric stabilisers such as poly(acrylic acid) [222] or poly(vinylpyrrolidone) (PVP) [29] for AgNPs, and multifunctional thiols for AuNPs [223]. CuNPs are also of interest, but their high susceptibility to oxidation during storage and sintering make successful ink formation challenging. Instead, Cu precursors, such as copper formate can be used [224].

Polymer inks are generally non-Newtonian, so require further rheological consideration. This is due to strain hardening effects during elongational flow, and mostly takes effect for concentrations where the molecules overlap. Optimisation of concentration and molecular weight is needed to avoid satellite drops, without allowing a linked network of molecules to form, which prevents the droplet detaching from the printhead [225]. Poorly soluble polymers, such as PEDOT:PSS, can be printed as nanoparticle dispersions of dopant-stabilised gels [5], and fully soluble polymers, such as poly(3-hexylthiophene) or polyvinylcarbazole, tend to have low polymer contents in the inks, < 1.5 wt.%. An alternative strategy, often used for dielectrics, is to instead print a reactive monomer precursor which is photo- or thermally cured, such as tripropylene glycol diacrylate (TPGDA) [226], polysiloxane [227], or poly(amic) acid [79]. This has the dual advantage of avoiding linked networks during drop formation and increasing the overall functional material content of the ink.

2.3.3 Droplet-Substrate Interaction

The first interaction between the drop and the substrate is the impact. To get accurate and precise drop placing, deposition must avoid splashing, rebound, or break-up [228,229]. This behaviour involves inertial, capillary, and gravitational forces, which are described by *Re*, *We*, and the dimensionless Bond number (*Bo*) respectively. *Re* and *We* are described in (2.1) and (2.2), and *Bo* is given as:

$$Bo = \frac{\rho g L^2}{\gamma_{IFT}} \tag{2.4}$$

Taking typical values for an ink – density $\rho \approx 1000\ \mathrm{kg\ m^{-3}}$, drop diameter $L \approx 100\ \mu\mathrm{m}$, surface tension $\gamma_{IFT} < 0.1\ \mathrm{N\ m^{-1}}$, and the gravitational constant g – shows that $Bo \ll 1$ and so gravitational forces can be ignored. A similar approach, considering the acceptable parameter space (**Figure 2.20**), shows that DOD printing is generally an inviscid process, and driven more by the effects of impact than capillary forces [230].

Ignoring gravitational forces, the final shape of the drop will approximate a spherical cap with a volume equal to the drop's initial volume. The diameter of the surface area in contact with the cap, D_{con}, depends only on the initial drop diameter, D_i, and the equilibrium contact angle, θ_{eq}. If a drop spreads upon impact, then the advancing contact angle is relevant, but flow reversals from drop interactions or solvent evaporation make the receding contact angle relevant. Contact angles are governed by the surface energy of the substrate, so variations in the surface energy can guide drops for finer feature resolution (**Figure 2.21**) [132,231,232]. Surface energy changes can also enable a broader category of inks for a given substrate – for example, surface coatings [233] or plasma treatment [233–236] to enhance hydrophilicity.

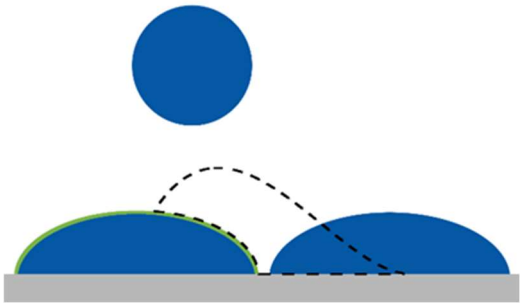

Figure 2.21: *A droplet of PEDOT:PSS ink (blue) flowing off a pre-printed, CF4-plasma-treated PEDOT:PSS pattern due to the high surface energy of the fluorinated surface (green). The intermediate position of the droplet is shown as the dashed black lines and the substrate is in grey. This allows for extremely small but repeatable separation between adjacent droplets. Reproduced from [132]*

2.3.4 Drop-Drop Interactions

Individual drops need to merge to form continuous patterns, for example a conductive trace, so the interaction of drops as they are spreading over the substrate is key to forming two-dimensional patterns. To create three-dimensional patterns, subsequent two-dimensional patterns are printed on already-solidified layers. Changes in surface energy do need to be accounted for in these subsequent layers, but the physical mechanisms will be the same [130].

If drops are printed too far apart, more than twice their radius, they will simply stay isolated and solidify independently (**Figure 2.22a**). As drop spacing decreases their spreading is stopped, resulting in a narrower bead with scalloped edges (**Figure 2.22b**). Further decreasing the spacing removes the scalloped edge, forming an ideal smooth-edged bead (**Figure 2.22c**) which is narrower still. Even closer drop spacing cause periodic bulges (**Figure 2.22d**), which tend to start at the beginning of a liquid bead. If the delay between drops is large enough – or the temperature high enough – each drop will evaporate before the next is deposited. In this case, regardless of drop spacing, each drop acts individually and creates a line of stacked discs (**Figure 2.22e**). On the other hand, bulging is encouraged by very little delay between drops [237]. Unfortunately, the idealised drop spacing, creates a virtual grid to which drop positioning must align, limiting flexibility in precise drop positioning [170].

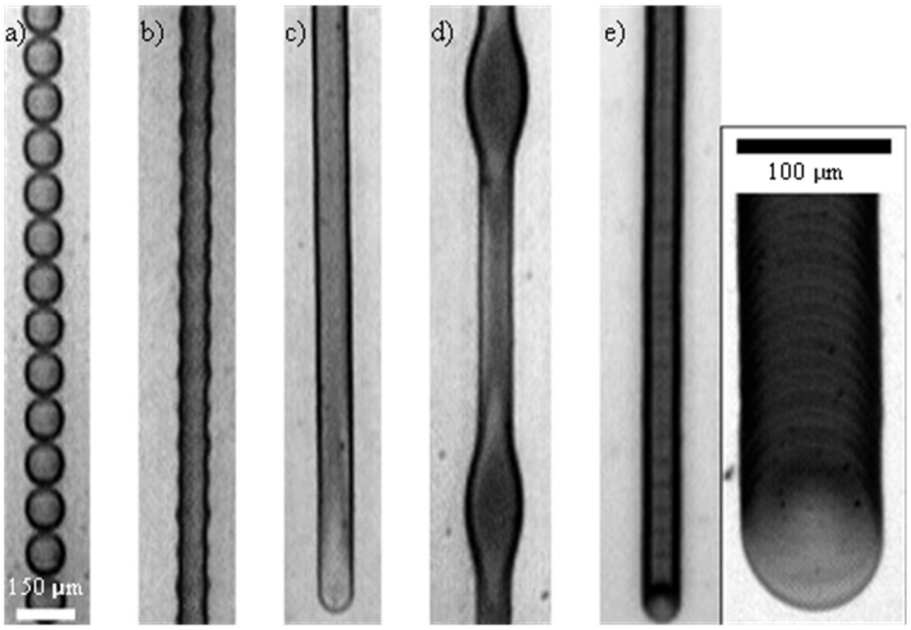

Figure 2.22: *Optical micrographs of inkjet-printed lines, with drop spacing decreasing from (a)-(d). The morphologies are called* ***(a)*** *"individual drops",* ***(b)*** *"scalloped",* ***(c)*** *"uniform", and* ***(d)*** *"bulging".* ***(e)*** *If drops solidify before the next is deposited, a "stacked coins" formation appears, seen more clearly in the magnified inset. Reproduced from* [237].

2.3.5 Drop Solidification

Solvent evaporation is the most common form of drop solidification in inkjet printing. This can lead to significant volume reduction, since long-chain polymer solutions and particle suspensions often need to be dilute to pass the rheological requirements discussed in **Chapter 2.3.1**. As the solvent evaporates, if the contact line is pinned and the contact angle is non-zero, fluid flows from the centre of the drop outwards, carrying solute with it. The solute segregates to, and is deposited at, the initial contact line, creating the "coffee ring" or "coffee stain" effect (CRE) [237–239]. This effect can be successfully used for twin-line deposition [133,240,241] and coffee-ring lithography [162,242], which has excellent resolution but more limited geometry.

Generally, printing requires an even deposition of solute, not a coffee ring. A second solidification mechanism, such as cooling wax [243,244] or gelation [245], or increasing the vapour pressure in the environment around the drop changes the evaporation dynamics to suppress the CRE, although the latter at the expense of overall evaporation rate [130]. Alternatively, a solution containing multiple solvents

with different vapour pressures (for example diethylene glycol or formamide combined with water [246,247]) will set up radial concentration gradients in the drop, as the higher-vapour-pressure solvent evaporates most quickly, increasing the surface tension at the edge – where this evaporation is greatest – and driving fluid back to the centre [248] in opposition to the CRE [249,250]. This process, known as Marangoni flow, is enhanced by increasing the temperature [251], unless crowding of suspended solids occurs due to the rapidly decreasing drop volume [252], which mostly occurs if the solids are poorly soluble in the primary solvent [253].

For inks where Marangoni flow does not occur – aqueous inks, for example – cooling the substrate can reduce the CRE. Cooling will reduce the evaporation rate at the thinner edges of the drop more than the thicker centre, reducing the driving force for outward flow [237]. Fluid flow and diffusion of solid content during evaporation can also cause segregation of the different constituents in the final dried drop, such as organic ligands travelling to the top of the drying drops, leaving an organic layer above the silver nanoparticles which impedes vertical electrical conductivity [37].

Drying mechanisms can become much more complex, with uneven contamination of the substrate altering the thickness of the rings (**Figure 2.23a**); contact lines breaking free and re-pinning at a smaller radius to form multiple rings (**Figure 2.23b**); the formation of central deposits surrounded by a coffee ring (**Figure 2.23c**); azimuthal deviation due to multi-solvent segregation (**Figure 2.23d**); and segregation into cells all having been reported (**Figure 2.23e**).

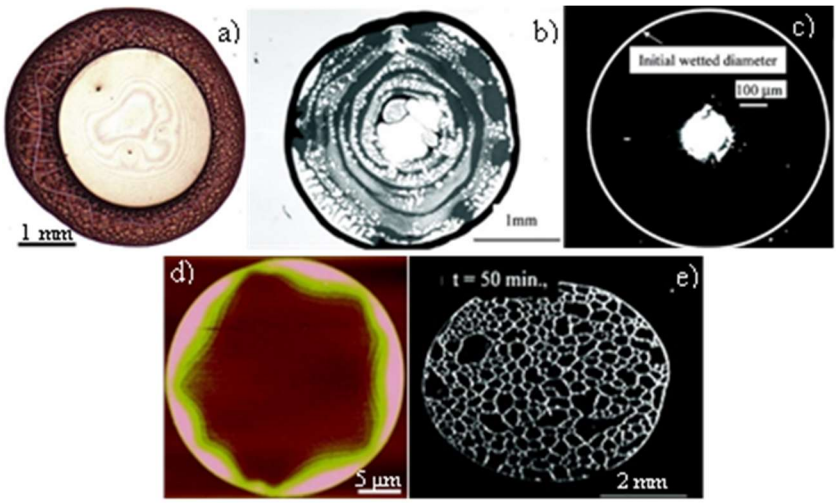

Figure 2.23: *Different morphologies of dried drops.* ***(a)*** *An uneven coffee ring caused by contamination on the substrate, from an aqueous drop with 60 nm polystyrene spheres on a titanium substrate* [254]*;* ***(b)*** *multiple rings, from an aqueous drop with 1 µm polystyrene microspheres on glass* [255]*;* ***(c)*** *a central bump significantly smaller than the original drop, from an isopropanol drop with 1 µm polystyrene microspheres on polydimethylsiloxane* [256]*;* ***(d)*** *a height map showing azimuthal deviations due to multi-solvent segregation, from a hexanol drop containing dendrimers on mica – pink regions are 60 nm higher than the dark brown regions* [257]*; and* ***(e)*** *hexagonal cells from an aqueous drop containing polystyrene microspheres with a high concentration of insoluble surfactant on a hydrophobic octadecyltricholorosilane substrate* [258]*. All images are optical micrographs except for (d), an AFM topographic image.*

The other most common form of solidification is UV-curing, i.e. initiating a reaction with ultraviolet light to polymerise the liquid ink. Such an ink is composed of monomers, a photoinitiator, and other additives [259]. The photoinitiator absorbs UV light to generate free radicals, which creates a chain propagation reaction that is eventually terminated when no more unreacted groups are available. A large range of such inks have been developed in literature, including polyacrylates [260], epoxy resins [261] and complex mixtures [262].

2.3.6 Challenges in Multi-Material Inkjet Printing

Multi-material inkjet printing appears at first to be nearly the same as the single-material printing discussed above. Simply add a second printhead and deposit a different material through it, in the same manner as CMYK graphical printing [1]. This independent method does have the same considerations as single-material printing during droplet generation, and droplet-substrate interactions are largely

similar too. The complications come during the droplet-droplet interactions and droplet solidification processes [263].

First, the introduction of a second material introduces three more interfaces – at the second material to the substrate, air, and first material – that need to be considered. After the first layer of printing there are also effectively two substrates to consider, and the problem compounds as more materials are added. If unaccounted for, this can lead to incomplete coverage, resulting in short circuits through insulating layers [264]. The understanding and ability to model such systems is still in its infancy, particularly when trying to model multiple types of inks together (e.g. an evaporative ink containing nanoparticles with a UV cured polymer ink) [265]. When two inks are miscible, the contact line between them will merge, resulting in interdiffusion. If a clear, high-resolution boundary is required, or if there is a low tolerance for contamination, the device performance will suffer as a result. However, this could be exploited to create a composition gradient or improve interfacial bonding to reduce the risk of delamination [266,267].

Second, different materials require different energy sources and intensities to solidify. Metal nanoparticles generally require temperatures above 300 °C or powerful IR irradiation to sinter together [268], which could damage polymers [269]. Differential expansion or contraction, caused by variations in temperature or chemical changes due to irradiation, can lead to a build-up in stress and ultimately crack inflexible layers [270]. Either polymers that can withstand higher temperatures must be used [79,205], or less damaging sintering routines, such as UV sintering [166] or precisely focussed laser sintering [271], adopted.

There have been several examples of simultaneous printing of conductive silver alongside an insulating dielectric to create 3D circuitry, taking advantage of the relatively low sintering temperature of silver nanoparticles (T_{sint} = 150 °C) and a temperature stable dielectric, poly (4-vinyl phenol) [264], or using UV sintering of silver nanoparticles to reduce the damage to the dielectric ink [166]. Both of these works pinned the silver, either with an elevated substrate temperature (T_{sub} = 65 °C) or UV irradiation respectively, to reduce the effect of differing fluid dynamics on the changing substrate as they built into 3D. Prints using more than two materials [72,263,271,272] generally have simple geometries and print sequentially, so that the printing parameters can be optimised to the specific print, rather than being able to generalise to any geometry, since the potential parameter space is too large.

2.4 Conclusions

Additive manufacturing is a promising set of techniques with the shared major benefits of low material wastage, digitizable customisation, and hugely increased design freedom [43]. One sector where it has the potential for massive impact is the production of electronics, where it could enable miniaturisation, customisation, and easy access to communication or imaging frequencies [51] otherwise restricted to expensive, wasteful production techniques such as lithographical etching [169].

A vast range of materials and applications are available to AM [3,58,70,110], but the most basic for any set of electronics are the conductors (e.g. silver, gold, graphene, PEDOT:PSS). Of these, silver has seen the most success for its balance of cost, chemical stability, and total conductivity, often being processed in the form of nanoparticles before being sintered [3].

The goal of miniaturisation requires high resolution (10s of microns) which, combined with the high electrical conductivity requirement, limits the AM techniques to inkjet printing, aerosol jet printing, and direct ink writing. IJP is the most mature technology and has the advantage of being able to process multiple materials simultaneously, which allows for the printing of supports and other functional materials to allow for whole-device manufacturing in one step [263]. However, AJP and DIW are significantly better at unsupported geometries [136,142], and have less anisotropy in their conductivity compared with inkjet printing [37].

All three are capable of printing high resolution circuits, with subtly different advantages. DIW excels at extremely dense circuitry which requires 3D bridge interconnects [137], AJP can produce the most complex lattices which might be useful for high-surface-area electrodes [142], and IJP can embed components within a dielectric to create a full device in one step whilst simultaneously being able to interface with microchips via soldering [35,168].

Antennas and metamaterials are also prime candidates for additive manufacturing, due to the strong connection between their performance and their structure. Particularly microwave and THz frequencies respond well to designs that utilise the resolutions of AJP [185], IJP [182] and DIW [187]. Microwave frequencies correspond to commonly used communication bands, so these antennas complement other potential devices which need to work remotely. THz frequencies are less explored, mostly because they exist in the so-called “terahertz gap”, a range of frequencies that has been historically difficult to work with. This makes it a prime target for metamaterials, a relatively less researched class of materials which use their structure to interact with highly specific frequencies. 2D filters and reflectors from resonating elements are documented, particularly with IJP [194–196] but also

DIW [136] and AJP [199]. 3D structures for metamaterials do exist, particularly photonic crystals [181], but little research has been dedicated to producing them with AM, despite analagous geometries being reported for other applications [40,103,139].

The three AM techniques being discussed all have some level of commercial attention: AJP through Optomec [202] and Cicor [203]; DIW through Voltera NOVA [179] and Hummink [171]; and IJP through several companies including BotFactory [35] and Nano Dimension [205]. Whilst DIW and AJP are superior in terms of 3D geometric complexity, IJP is by far the most industrially ready, mostly because of its ability to use multiple nozzles, sometimes thousands per printhead, and multiple heads simultaneously, enabling fast, multimaterial manufacturing [263]. Therefore, enhancing the ability of IJP to produce complex, 3D geometries would immediately impact how complex electronics could be manufactured.

The primary challenges associated with IJP are the anisotropy and the lack of 3D complexity. The former is caused by segregation of organic ligands to the top of each printed layer, creating an insulating barrier to electrons trying to flow to the next layer up [37]. The ligands are required to stabilise the nanoparticles in the ink, so they don't aggregate and clog up the nozzle. The alternative to nanoparticle inks are metal salts, however they also have organic impurities and tend to have such low metal loading that they negate IJP's speed advantage [2].

The problem of 3D complexity can be tackled in two ways – by printing supports [39] or by pinning the drops so solidification can occur more rapidly than liquid flow [40]. Support material complicates the printing process significantly – the number of interfaces to consider for wetting and intermixing increases, different layer heights have to be accounted for, and the processing environment has to be amenable

to all of the materials involved [126]. However, this problem has been approached, both in literature [41] and commercially [168]. The alternative – rapid pinning – has also proved successful but requires extremely high precision to avoid collapse of even slightly overhanging structures [40]. This generally requires a customised printing setup, since the manner in which inkjet printers process geometric data requires aliasing of drop positions to approximately half that of the drop's radius [170].

3 AIMS AND OBJECTIVES

3.1 Research Gaps and Challenges

For additive manufacturing to deliver on its potential significant advantages for manufacturing multimaterial electronics, it must deliver high resolution and electrical conductivity, limiting viable methods to inkjet printing, aerosol jet printing, and direct ink writing. IJP is the most mature, particularly for multi-material printing and in terms of scalability but is less suited for unsupported geometries and suffers from significant anisotropy in conductivity.

Key target applications include antennas and metamaterials, especially for applications in microwave and terahertz (THz) frequencies. Whilst 2D structures such as filters and reflectors are documented, research on AM of 3D metamaterials in these frequency domains remains sparse.

The key research challenges are therefore optimising the material properties of the print, including the effect of post processing; the liquid nature of the ink requiring rapid pinning to avoid slumping; matching the processing parameters and environment in multimaterial prints; and the development of strategies for high accuracy reproduction of antenna- or metamaterial geometries in both 2- and 3 dimensions.

3.2 Aims and Objectives

The first step towards 3D multimaterial designs is to optimise a two-ink system of conductive silver nanoparticles and a dielectric polymer, since those are the most commonly used across a wide range of application. Particularly, it is important to establish the relationship between the composition of the conductive silver inks and their electrical performance in three dimensions, as well as looking into the effect of post-processing treatments. The dielectric material will then be chosen according to

its printability and dielectric properties, as well as considering their ability to withstand the high temperatures required to print and sinter the silver ink

Next, a printing strategy will be developed and optimised to increase the control over ink drop deposition. The primary aim is to reduce the aliasing effect of translating continuous geometrical data into pixel-based images, which should improve the performance of geometry-sensitive devices such as antennas and metamaterials. Further, it will enable printing unsupported overhangs, mimicking the abilities of custom setups in the literature but compatible with traditional inkjet printing technology. This will allow for easier integration of larger designs and multimaterial deposition.

Finally, the optimised material properties and printing strategies will be combined to fabricate complex 3D structures, in both single- and multimaterial prints. This work will build towards the fabrication of 3D devices, such as antennas and metamaterials, that take advantage of unique, high-resolution geometries for enhanced performance and novel capabilities.

3.3 Methodology

Development of novel materials for inkjet printing is a difficult and time-consuming process, and so this project's collaboration with Nano Dimension will utilise their current high-performance formulations alongside more readily available alternative inks to establish a solid comparison with the literature. All of the inks will undergo rheological testing to establish their printability. The silver nanoparticle inks will be characterised according to chemical composition and particle characteristics, before optimising their conductivity in all three directions with a sweep of post-print sintering parameters. The dielectric inks will be selected according to their compatibility with

the silver's sintering environment, as well as their dielectric properties at the frequencies of interest. This work is presented in **Chapter 5**.

Enabling higher resolution requires removing the aliasing effect of representing continuous geometry with pixellated bitmaps. However, standard printing technology requires bitmaps to operate, so a new conception of what pixels represent is required. **Chapter 6** shows the development of breaking the conceptual link between the size of a pixel and the size of a physical drop, which requires new algorithms to be developed to create such bitmaps. These algorithms will be investigated for their effectiveness in reproducing the target geometry with a simplified model for the material distribution of print resulting from this deposition strategy, along with consideration of the surface topology. Simple shapes, such as triangles and circles, will be used initially, before looking at more complex designs which could be used antennas or metamaterials.

Finally, the ink selection and novel printing strategies will be combined to produce complex 3D geometries. This will start with silver-only materials, targeting single-drop pillars that have been previously reported, but only on limited custom setups. The new strategy developed will target larger arrays, particularly for lattice geometries. The second, dielectric material will then be used to enable geometries that require support, such as with floating elements. The target application is an anisotropic dielectric, where the density of silver can be smoothly adjusted within the print using the new high-resolution strategy to allow for spatial control of the dielectric properties. This work is presented in **Chapter 7**.

4 MATERIALS AND METHODS

4.1 Materials

Several commercial inks were used in this work as received unless otherwise stated. Three were formed from suspended silver nanoparticles (AgNPs) in a solvent and were used to print conductive features. AgCite^{TM} 90072 Silver Nanoparticle Conductive Ink is produced by Nano Dimension ($Ink_{Ag,ND}$) and was supplied by the Manufacturing Technology Centre; DGP 40LT 15C is produced by Advanced Nano Products ($Ink_{Ag,ANP}$) and was purchased from Printed Electronics Limited; and Ag Nanoink IJ36 ($Ink_{Ag,XTPL}$) is produced by XTPL and was purchased direct. According to the supplied data sheets $Ink_{Ag,ND}$ has a solid content of 50 wt.% suspended in 2-(2-butoxyethoxy)ethanol; $Ink_{Ag,ANP}$ has a solid content of 30-35 wt.%, suspended in triethylene glycol monoethyl ether; and $Ink_{Ag,XTPL}$ has a solid content of 34 wt.%, suspended in 2-(2-butoxyethoxy)ethanol.

$Ink_{Ag,ND}$ was chosen due to it's very high silver content – the largest available, and exceeding anything reported in literature for inkjet printing. However, it is not widely used since it is only sold alongside Nano Dimension's Dragonfly printer. $Ink_{Ag,ANP}$ was therefore also included, since it is the most commonly used silver nanoparticle ink throughout the literature. However, it has both a significantly lower silver content and utilises a different solvent. $Ink_{Ag,XTPL}$ helps to bridge the gap between these inks, having a similar silver content to $Ink_{Ag,ANP}$ but the same solvent as $Ink_{Ag,ND}$.

UV-curable polymer inks were used to print dielectric features and as a supporting matrix for 3D silver designs. Dielectric Ink 1092 is produced by Nano Dimension ($Ink_{Di,ND}$) and was supplied by the Manufacturing Technology Centre. It is a mixture of UV curable acrylates: 4-(1-oxo-2-propenyl)-morpholine (>30 %), 2-propenoic

acid, 1,1'-(1,10-decanediyl) ester (15-50 %), (octahydro-4,7-methano-1H-undenediyl)bis(methylene) diacrylate (15-50 %), (2,4,6-trioxo-1,3,5-triazinane-1,3,5-triyl)triethylene triacrylate (5-30 %), and a urethane acrylate oligomer (5-30 %). The full composition - specific chemical identity and exact percentage of composition – has been withheld as a trade secret.

Three UV-curable polymer inks were made in-house. The first ($Ink_{Di,TPGDA}$) contains 3 wt.% ethyl 4-(dimethylamino)benzoate (EDB, the initiator), 3 wt.% 2,4-diethyl-9H-thioxanthen-9-one (DETX, the accelerant and co-initiator), and 94 wt.% tri(propyl glycol) diacrylate (TPGDA). The second ($Ink_{Di,EGDPEA}$) was made from 3 wt.% EDB, 3 wt.% DETX, 18.8 wt.% tricyclo[5.2.1.$0^{2,6}$]decanedimethanol diacrylate (TCDMDA), and 75.2 wt.% ethylene glycol dicyclopentenyl ether acrylate (EGDPEA). Finally, $Ink_{Di,ACMO}$ was made from 3 wt. % EDB, 3 wt.% DETX, and 94 wt.% 4-acryloylmorpholine (ACMO). All chemicals were purchased from Sigma Aldrich and used as received. All inks were made in a dark room to avoid premature UV exposure and mixed for at least 24 hours before use.

$Ink_{Di,ND}$ is included due to it being designed for compatibility with InkAg,ND alongside decent dielectric properties in the microwave-GHz frequency range. These other three dielectric inks represent a range of inks known to have stable jetting properties, with $Ink_{Di,ACMO}$ and $Ink_{Di,TPGDA}$ having been used for early studies as a support matrix. $Ink_{Di,EGDPEA}$ has also been included because of its potential for fine tuning of the material properties in future studies by tweaking the EGPDEA:TCDMDA ratio.

The following substrates were used: borosilicate glass microscope slides (Fisher), polyethylene terephthalate (PET) and polyethylene naphthalate film (GTS Flexible

Materials Ltd), polyimide (Kapton® HN general purpose polyimide film, Dupont), indium tin oxide (ITO) coated borosilicate glass (Sigma Aldrich), prime grade silicon wafers with 200 nm SiO_2 surface coating (PI-KEM). All substrates were wiped with IPA and dried with N_2 prior to use.

4.2 Inkjet Printing

Two inkjet printers were used in this work, along with four types of printhead. The PixDRO LP50 printer can print large numbers of layers (>100) with complex designs. It is compatible with Spectra SE-128 AA printheads, which have excellent accuracy (<5 μm when optimised) and good resolution (30-100 μm drop radius, depending on the specific ink and substrate), as well as the ability to jet AgNP inks in a stable manner for a long time. They were used to print a wide variety of silver structures, especially designs with complicated printing strategies, as well as some multimaterial designs. Xaar-128 printheads were also used with the LP50 printer, with the advantage of large drop volumes and stable printing of the dielectric inks at elevated temperatures. They were used to print multi-material polymer-and-silver designs, particularly where the larger drop volume was advantageous (see Table 4-1). The Fujifilm Dimatix DMP-2800 was used with its proprietary printheads (see Table 4-1) for silver prints with few layers. It is more commonly used in the literature than the LP50, so it is a good reference point for the standard capabilities of 3D inkjet printers and requires much smaller volumes of ink (<0.5 mL for the Dimatix printer compared to >5 mL for the LP50 printer).

For both printers, the overall process of setting up a print through each one's proprietary software is similar. First, the ink is loaded into the printhead reservoir and flushed through to the nozzles with a small positive air pressure. The jetting

parameters are then optimised to ensure optimal production of droplets. At this stage it is also possible to identify active vs defective nozzles and inform the printer which ones to use for the actual print. Then, a simple square or line geometry is used to determine optimal printing parameters such as drop spacing and substrate temperature. **Chapter 4.2.3** contains more details of the specifics for these optimisations. Both printers take the pattern to print from bitmaps, which are converted into swathe movement and nozzle firing data which the printer motors and piezoelectric actuators can utilise by internal code built into the printer's software. The origin point can be chosen by the user; the Dimatix prints starting at the top-left of the bitmap, whereas the LP50 can start at any corner, although the default is the bottom-left. The Dimatix can only print one material at a time and has an inbuilt function for repeating the same bitmap for up to 99 layers. The LP50 is more flexible, but requires user-written C# code to print anything more complicated than a single layer of one bitmap.

4.2.1 PixDRO LP50

The LP50 is an R&D focussed printer able to operate multiple printheads independently, allowing for multimaterial printing. It is operated through a proprietary user interface, which allows for control of various built-in functionality to optimise the jetting process, as described below. Further, there is built in functionality which can accessed via C# code, such as printhead maintenance or the function which triggers the printer to print any generated print data. A simple piece of C# code is provided for the user to print a single bitmap, which can then be modified to be as complex as necessary. For example, code could be written to loop over all the bitmaps in a folder and print each one in turn, as well as modifying parameters such as drop spacing, the print start location on the substrate, or the actively jetting printhead (if multiple are connected) at any point. This code is then run from the graphical user

interface after setting up all of the parameters not otherwise specified in the C# code. This enables a huge amount of flexibility in the print process not achievable on any other system.

Movement in the y-axis (**Figure 4.1**) is typically preferred for the primary printing direction. The X-, Y-, and Z-axes create a printing volume of 310 × 210 × 25 mm, with the S-axis allowing for substrate rotations of ±1°. The P-axis can rotate the assembly, which hold the printheads and ink reservoirs, a total of 94°.

The system has an aluminium substrate platen, which can be heated to T_{sub} = 70 °C and includes a vacuum clamp to mount substrates. A secondary heated platen was commissioned from Trent Thermal Technology to enable $T_{sub} \leq 200$ °C. There are monochrome cameras to monitor the drop formation (dropview camera) and view the substrate (printview camera). The dropview camera has a stroboscopic LED synchronised with the jetting signals to form an image of many droplets averaged over a set time period. This allows the user to monitor the effects of changing the printing parameters – such as waveform, jetting frequency, temperature, etc. – in real time and determine the optimal parameters for ideal jetting. The printview camera has a ring light and a coaxial light and is primarily used to set the origin of the print and quickly view the outcome of a printed pattern.

Figure 4.1: *Diagram of the motion systems (left), modified from [273], and photograph (right) of the PixDRO LP50 printer.*

The ink and printheads are carried on the printhead assembly (PHA), which is moved as a whole along the X-axis and rotated about the P-axis. The PHA attaches to a carrier assembly via a magnetic mounting ring, which enables repeatable positioning of the PHA and disengages if the printheads are obstructed for protection. The ink is held in a reservoir under negative pressure (P_{ink} = -3.8–0 kPa) during printing, with up to P_h = +25 kPa for purging. Ink goes from the reservoir to the printheads via a heating block, which heats both the ink and the printhead to a temperature $T_h \leq 90$ °C to optimise the ink's rheology for jetting. The PHA used in this work contains two separate ink-delivery systems with two printheads to allow for simultaneous printing of two materials. A second PHA was developed in collaboration with Added Scientific Ltd that can run 4 independent Xaar-128 printheads.

The nozzles can be cleaned and unblocked by purging (using air pressure to force ink through the nozzles) and wiping on a microfibre cloth roll. Additionally, it has capping stations for the Spectra SE-128 AA printheads (**Chapter 4.2.3**) that apply a negative pressure to suck ink or built-up aggregates out of the nozzles.

4.2.2 Dimatix DMP-2800

The Fujifilm Dimatix DMP-2800 is an inkjet printer that is used for ink development and single-material printing. The software enables users to define the printing parameters – such as waveform, printhead temperature, etc. – and print 2D bitmaps.

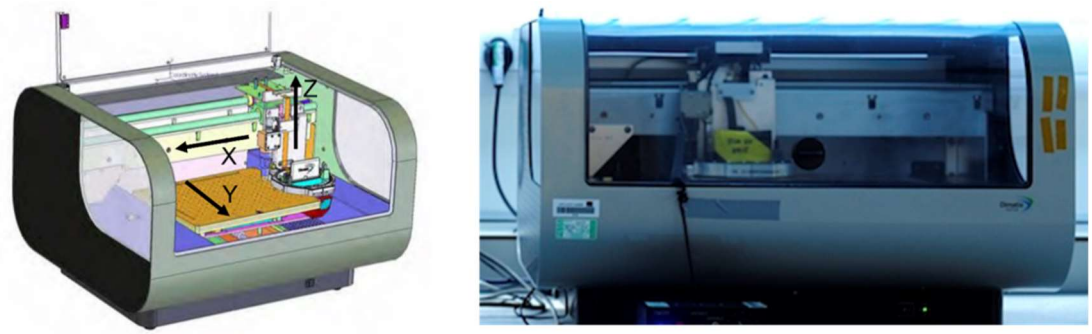

Figure 4.2: *Diagram of the motion systems (left), modified from [273], and a photograph (right) of the Fujifilm Dimatix DMP-2800 inkjet printer.*

The motion of the printer is modelled in **Figure 4.2**. X-axis movement is typically preferred for the primary printing direction. The X-, Y-, and Z-axes create a printing volume of 315 × 210 × 0.5 mm or 260 × 210 × 25 mm, depending on substrate thickness. The printhead can be rotated about the Z-axis by hand, using a Vernier scale to get 0.1° of accuracy, in order to change the nozzle spacing in the Y-direction.

The system has a metal substrate platen, which can be heated to $T_{sub} \leq 60$ °C and includes a vacuum clamp to hold down substrates. Higher temperatures ($T_{sub} \leq 120$ °C) can be reached using a custom resistive heater consisting of a wire wound around a glass microscope slide and insulated with Kapton tape, or with a customised Ultimaker Heated Bed (up to $T_{sub} = 90$ °C). As with the LP50, there are 2 monochrome cameras to monitor the drop formation (dropview camera) and view the substrate (printview camera). These work as described for the LP50 in **Chapter 4.2.1.**

The printheads are attached to a cartridge, which can hold up to 1 mL of ink and has an air pressure port which can be used to purge the printheads with $P_h \leq 35$ kPa. The assembly which carries the printheads and cartridge is carried along the X-axis.

The nozzles can be kept clean and unblocked by purging (using air pressure to force ink though the nozzles) and blotting (touching the nozzles to a blotting pad to remove excess ink that has built up on the nozzle plate).

4.2.3 Printheads

Printheads are the devices which perform the ejection of drops of ink out of its nozzles. A pressure wave in the fluid chamber behind the printing nozzle builds pressure up beyond a certain threshold to overcome the surface tension and eject a drop. All printheads used in this work generate the wave with a piezoelectric actuator, which

gives excellent control over the waveform and thus the precise volume and ejection velocity of the drop [206].

The Dimatix DMP-2800 printer uses either a DMC-11610 (discontinued by the manufacturer in 2021) or Dimatix Samba cartridge, and the PiXDRO LP50 printer uses a Spectra SE-128 AA printhead. The PiXDRO LP50 was also retrofitted to accept Xaar 128 printheads. This retrofit was designed and built in collaboration with Added Scientific Ltd. The printheads are compared below in **Table 4-1**.

Table 4-1: *Printhead specifications and recommended ink parameters for the DMC-11610, Dimatix Samba, Spectra SE-128 AA, and Xaar 128 printheads.*

	DMC-11610	**Dimatix Samba**	**Spectra SE-128 AA**	**Xaar 128**
Manufacturer	Fujifilm	Fujifilm	Fujifilm	Xaar
Nozzle diameter / μm	21	17	35	49.5
Number of nozzles	16	12	128	128
Drop volume / pL	10	2.4	25-30	80
Ink viscosity / cps	10-12	4-8	8-20	5-17
Ink surface tension / mN m^{-1}	28-30	28-32	–	20-45
Maximum temperature / °C	60	60	90	55
Maximum jetting frequency / kHz	15	80	40	10

In both systems, ink was purged through the printheads to fill the nozzles and flush out any blockages. Drop formation was then optimised with the built-in drop watcher system to tune the voltage waveform. Ideal jetting produces drops that fall vertically with tails that thin then break without producing satellite drops before merging with the main drop to form a single sphere before it contacts the substrate (**Figure 4.3a**).

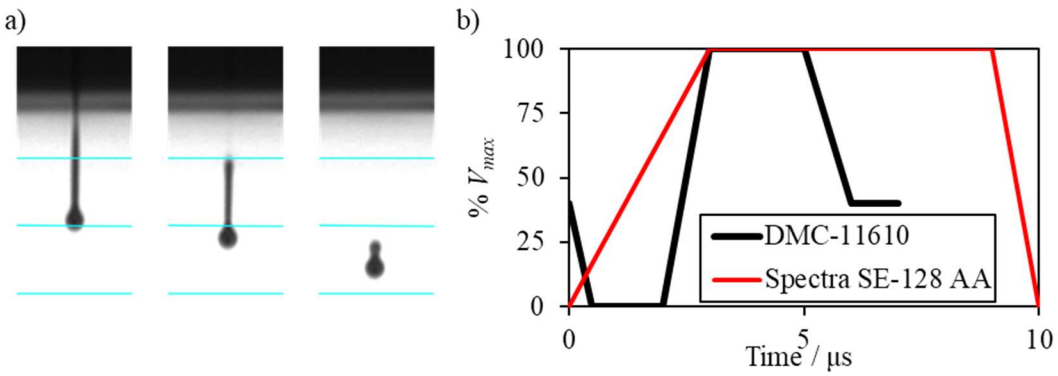

Figure 4.3: (a) *Still frames from the recording of $Ink_{Ag,ND}$ drop formation from a Spectra SE-128 AA printhead. From left to right, the ink is ejected and detaches from the nozzle, followed by retraction of the tail into the main drop, forming a single sphere. The blue lines are 100 µm apart.* ***(b)*** *The voltage waveforms for $Ink_{Ag,ND}$ in a DMC-11610 cartridge (black), and a Spectra SE-128 AA printhead (red). Both printheads are heated to 40 °C, but the maximum voltage (V_{max}) of the DMC-11610 cartridge is set to V_{max} = 40 V, whereas the maximum voltage of the Spectra SE-128 AA printhead is set to V_{max} = 53 V.*

A waveform is the voltage signal sent to a piezoelectric transducer in the printhead to change its shape and push ink out of a nozzle. The precise values and shape of the waveform depend on the cartridge in use as well as the ink. For example, the waveform to print $Ink_{Ag,ND}$ in a Dimatix DMC-11610 cartridge starts with the voltage at 40 % of the maximum. It relaxes to zero to pull ink into the chamber, then jumps to 100 % to expel the ink. By contrast, the waveform to print the same ink in a Spectra SE-128 AA printhead only requires the expulsion phase (**Figure 4.3b**). In all printheads, the voltage levels of this waveform can be specified to an accuracy of 0.1 V, and for all but the Xaar 128 printheads, the timing of the voltage setpoints (e.g., how rapidly it goes from the relaxed state of 0 V to the maximum) can be specified to an accuracy of 0.1 µs. The waveform timings of the Xaar 128 printheads cannot be changed. These adjustments allow for drop ejection velocities between 1-10 m s^{-1}, and droplet volume adjustments of ~10 % from the nominal drop volume, depending upon the ink.

Along with the waveform, the printhead temperature (T_h), maximum voltage (V_{max}), frequency (f), and applied pressure (P_{ink}, LP50 only) were optimised for ideal jetting. Heating the substrate can cause indirect heating of the printhead, which changes the

rheology of the ink inside the head. Therefore, this was also optimised alongside the jetting parameters which are presented in **Table 4-2**.

To find the optimal jetting parameters, first T_h is selected to achieve the desired rheology. Then, for the LP50, P_{ink} is adjusted by purging ink through the nozzles and adjusting until ink that is wetting the nozzle plate is neither falling off due to gravity but also not being sucked back up into the printhead. Finally, the waveform voltage is adjusted to maximise the drop ejection velocity, which can be measured natively with either printer's dropwatcher facility, without creating satellite drops. If a velocity of at least 1 m s^{-1} cannot be achieved, the timings of the waveform may be adjusted through a process of trial-and-error until a sufficient drop velocity is possible.

Table 4-2: *Jetting parameters for the inks and printheads used. T_h = set printhead temperature, T_{sub} = substrate temperature, f = frequency. *V_{max} = maximum voltage as defined by* ***Figure 4.3b****. DMC-11610 and Samba cartridge used the same waveform. The Xaar-128 waveform has been withheld as a trade secret. **The LP50 printer requires a negative pressure (P_{ink}) on the ink to prevent it from flowing out of the nozzles under gravity. The Dimatix DMP-2800 doesn't require this function. ***Changes depending on the temperature of the printhead, which rises during a print with a heated substrate.*

Ink	Printhead	T_h / °C	T_{sub} / °C	V_{max}* / V	P_{ink}** / mbar	f / Hz
$Ink_{Ag,ND}$	DMC-11610	40	60-100	35	-[2]	10000
	Samba	40	60-100	35	-	10000
	Spectra	40	70	55	-25	200-2000
$Ink_{Ag,ANP}$	Spectra	40	70	55	-25	200-2000
$Ink_{Ag,XTPL}$	Samba	40	60-100	35	-	10000
	Spectra	40	70	55	-25	200-2000
	Xaar-128	20	90-150	20-35***	-13	1000
$Ink_{Di,EGDPEA}$	Xaar-128	20	20-150	35	-10	1000
$Ink_{Di,ACMO}$	Xaar-128	20	20-150	35	-10	1000
$Ink_{Di,TPGDA}$	Spectra	55	70	45	-27	1500
	Xaar-128	20	20	35	-10	1000
$Ink_{Di,ND}$	Spectra	55	70	45	-27	1500

The drop spacing was also optimised to form a continuous film without bulging. For a given set of jetting parameters, printing environment, and ink, a drop spacing test was run, where 1×50 drop lines (horizontal and vertical), and a 1 mm square were printed at a range of drop spacings and the optimal range decided upon visually. The

ranges for the sweep were: 10-50 μm for DMC-11610 & Samba printheads with a precision of 5 μm; 300-500 DPI for the Spectra SE-128 AA printheads with a precision of 10 DPI; and 150-300 DPI for the Xaar-128 printheads with a precision of 10 DPI.

4.2.4 Printing Strategy

Deposition strategy alters the sequence in which drops are deposited to optimise the merging and solidification of the material on the substrate or previously printed layers to achieve a smooth, continuous film with well-defined edges. All prints in this work used a leader bar, where 10-20 drops were ejected and discarded before the desired pattern is printed. This is needed because the first few drops of each swathe are the least stable and liable to eject at the incorrect angle.

The silver nanoparticle inks require time to dry before the next layer can print and can flake if too much ink merges and dries together. Therefore, striped and chequerboard strategies were adopted to allow smaller sections to dry individually. This method involved assigning each pixel in the original bitmap into two sets (blue or green in **Figure 4.4a**) according to either a striped or chequerboard pattern. The bitmap created from just the blue set of pixels was printed first, followed by the bitmap created from the green set.

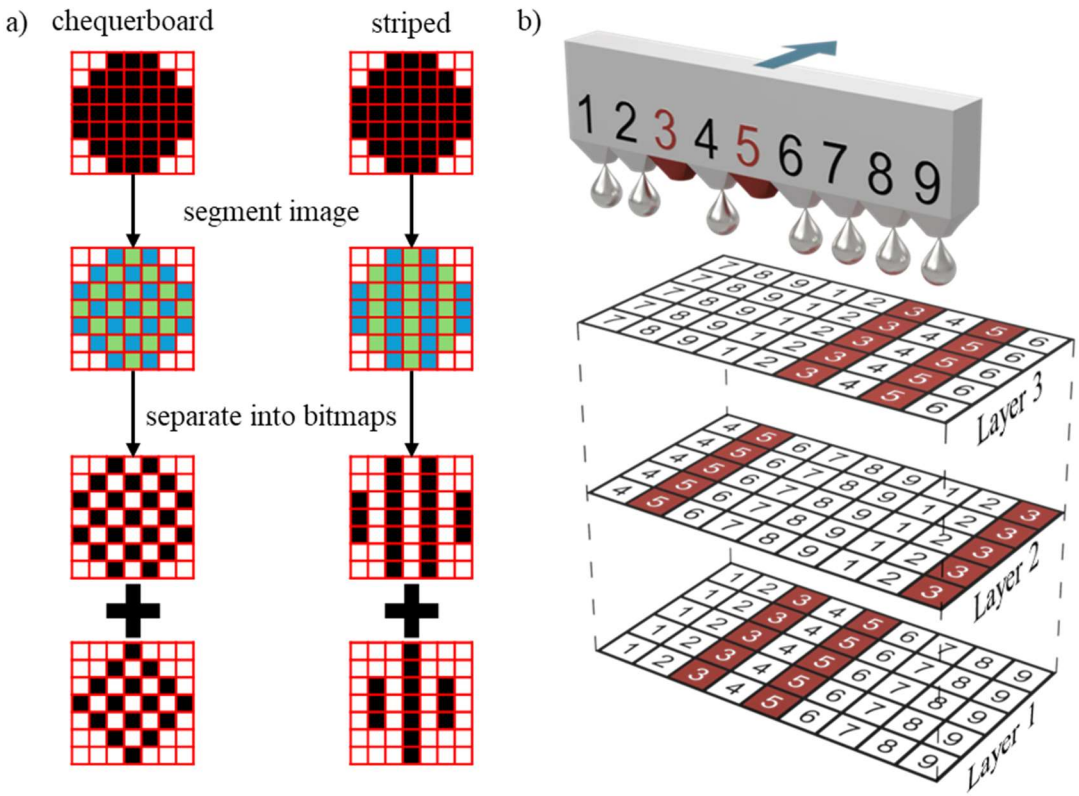

Figure 4.4: *Schematics of different print strategies for improved printing quality.* ***(a)*** *Images can be segmented into separate bitmaps to allow for different drying characteristics in either a chequerboard or striped pattern. Here, vertical stripes are demonstrated, but horizontal stripes can also be used. The black pixels in the original bitmap (top) are those where a drop will be printed, so only those pixels are segmented into the separate categories (blue and green). Separate bitmaps are made from each individual category and passed to the printer one at a time for printing (blue first).* ***(b)*** *A pixel step-over can help to spread the effect of faulty nozzles out over the whole print, instead of causing a single point of failure. The printhead (grey) moves over the area to be printed in the direction of the blue arrow. Numbers on the printhead indicate the corresponding nozzle number. Both number and nozzle are coloured red to indicate if that nozzle is faulty, otherwise a silver drop is shown being ejected. The three layers (black grids) show which nozzle prints a drop at each location – the red coloured squares indicate if it has been printed with a faulty nozzle. A pixel step-over of 3 is demonstrated here, where the nozzle number aligned with the leftmost column of each layer increases by 3 for each layer.*

For increased reliability, one nozzle was typically used during printing, except in the case of the Xaar printheads. Here, all 128 nozzles were activated, and a pixel step-over was used instead. This changes which nozzle prints the first column of the bitmap on each layer, with subsequent passes filling in the remaining columns as usual. **Figure 4.4b** demonstrates this for a printhead with nine nozzles and a pixel step-over of 3. Each of three layers is represented by a grid, with each number in the grid representing which nozzle ejected a drop at that position. The first layer is printed in a single swathe (i.e., a movement of the printhead transverse to the line of the nozzles

during which drops are ejected), aligning the first column of the layer with nozzle 1. However, nozzles 3 and 5 are blocked (marked red in **Figure 4.4b**), meaning those columns of the layer will not actually be printed. If multiple layers were printed identically, there would always be a gap in those columns.

Instead, the second layer has its first column aligned with nozzle 4, since the previous layer had aligned nozzle 1 to its first column and the chosen pixel step-over is 3: 1 + 3 = 4. Therefore, the second column (printed by nozzle 5) is faulty in this layer. Since there are nine total nozzles, only the first six columns of this layer are printed in the first swathe, so the layer is finished by moving the printhead over and aligning the seventh column with nozzle 1, thus the ninth column (printed by nozzle 3) is faulty.

Similarly, the third layer has nozzle 7 aligned with its the first column, resulting in faulty sixth and eighth columns. In this way, any nozzles which are blocked (before or during the print) are put in varied positions on each layer, averaging out negative effects over the course of the print. This requires the number of identical layers being printed to larger than the number of nozzles that are blocked to be effective.

The printhead moves along the primary printing direction, firing drops at the required times according to the selected drop spacing and print speed, as well as the bitmap being printed. Bitmaps for printing were made and edited either using the software GIMP [274] (version 2.10.14), or from custom MATLAB [275] scripts (available in the Supplementary Information). A single movement of the printhead is a swathe, and multiple swathes build up laterally to form a printed layer. Often, the first few drops of each swathe are the least stable and liable to eject at the incorrect angle. Therefore, leader bars were printed to discard these first few drops before the

actual pattern starts. Subsequent layers can be printed on top of previous, solidified layers to build a part up in three dimensions.

The drop spacing is the distance between neighbouring droplets that are intended to merge. For a given ink, substrate, drop volume, and substrate temperature, there is a relatively narrow range of values that will give a uniform line or film without any gaps or bulges [237], so this parameter must also be optimised.

4.2.5 Solidification and Post Processing

Once deposited, the liquid ink needs to solidify into a cohesive layer and may require post-processing to improve the material properties. Evaporative inks ($Ink_{Ag,ND}$, $Ink_{Ag,ANP}$, and $Ink_{Ag,XTPL}$) are solidified on the substrate using an elevated substrate temperature (**Table 4-2**). A Vacuutherm vacuum oven (Thermofisher) was used to sinter AgNPs for a period of t_{sint} = 1-24 hrs, at a temperature T_{sint} = 120-200 °C and at ambient pressure.

$Ink_{Di,EGDPEA}$, $Ink_{Di,TPGDA}$, $Ink_{Di,ACMO}$, and $Ink_{Di,ND}$ were cured using a UV lamp (Phoseon FireFly 25x10AC395-4W), attached behind the printhead and turned on during printing (per-swathe curing) or swept over an entire printed layer (per-layer curing). The distance between lamp and the sample is 30 mm, leading to a power density of P_z = 6 mW cm^{-2}, as measured by an RSP-PRO UV Meter (106-5310). Per-swathe curing occurs at the speed of the print, whereas the speed of the per-layer curing was adjusted between 10-100 mm s^{-1} to adjust the UV dosage. No post-processing was required for these inks.

4.3 Characterisation Methods

4.3.1 Fourier-Transform Infrared Spectroscopy

Fourier-transform infrared spectroscopy (FTIR) measures a sample's response to infrared and near-infrared radiation (wavelength λ_z = 2.5-25 μm, or wavenumber n_z = 4000-400 cm^{-1}) to characterise the chemical bonds present. Vibration and rotation of atoms about their bonds alters the dipole moment of the bond, with the characteristic frequencies affected by the mode of motion, the mass of the atoms, and the bond type. IR photons are absorbed by the sample at the corresponding energy to these frequency modes, so the peaks in the absorption spectrum can be matched to the corresponding chemical bond present in the sample [276]. An FTIR spectrometer scans the wavelength illuminating the sample across the IR range by means of a Michelson interferometer, where an IR beam is split by a semi-permeable beam splitter, then recombined. The path lengths of each split part of the beam can be chosen to cause constructive interference at the chosen wavelength and destructive interference otherwise.

A Perkin Elmer Fourier transform infrared Frontier Spectrometer was used to record the infrared transmission spectrum of uncured and UV-cured $Ink_{Di,ND}$. The curing mechanism entails the breaking of the C=C bond, but not the C=O bond. The change in the ratio of the corresponding peaks' areas before and after curing was used to estimate the conversion rate.

4.3.2 Ultraviolet-Visible Spectroscopy

Ultraviolet-Visible (UV-Vis) spectroscopy measures a sample's absorption of photons within the wavelength range λ_z = 190-1100 nm. A UV-Vis spectrometer illuminates the sample across this range by means of a diffraction grating, which disperses the light from a xenon flash lamp into its constituent wavelengths. The required

wavelength is selected by a movable mirror and a slit. The absorption spectrum of nanoparticles in this range is heavily influenced by their size and shape, so their peak absorption wavelength is used as an estimate of nanoparticle size which is insensitive to clumping [277].

Ink nanoparticles' charge carriers experience quantum confinement, which is strongly affected by the nanoparticle size. Absorption of a photon occurs at energies corresponding to the separation between the energy levels of the confined charge carriers, so the position and width of the absorption peaks in the UV-Vis spectrum gives a measurement of the size distribution. For nanoparticle solutions with organic capping ligands, the peak position is insensitive to clumping, unlike other methods such as dynamic light scattering [277].

A Cary 3500 UV-Vis spectrophotometer with Kartell Art. 1938 PMMA cuvettes was used to measure the absorption spectrum of $Ink_{Ag,ND}$, $Ink_{Ag,XTPL}$, and $Ink_{Ag,ANP}$ at wavelengths of 200-900 nm, with a step size of 1 nm and a dwell time of 0.02 s. Each ink was diluted with IPA by a factor of 10^4 to optimise the signal-to-noise ratio.

4.3.3 Dynamic Light Scattering

Dynamic light scattering (DLS) measures the scattering of monochromatic light on particles undergoing Brownian motion in solution. The phase difference between a reference beam and a laser scattered by the sample varies as the particles move, causing fluctuations in intensity due to interference between the beams. The rate of these fluctuations is correlated to the translational diffusion coefficient, D, which is related to the hydrodynamic diameter of the particles, d_H, according to the Stokes-Einstein equation:

$$D = \frac{kT}{3\pi\eta d_H} \tag{4.1}$$

where k is the Boltzmann constant, T is the temperature, and η is the viscosity. The hydrodynamic diameter is that of a sphere with the equivalent mobility to the particles in solution, including the effects of any ligands or solvent interaction.

A Malvern Zetasizer Nano-ZS equipped with a He-Ne laser was used to measure the particle size distribution of $Ink_{Ag,ND}$, $Ink_{Ag,XTPL}$, and $Ink_{Ag,ANP}$. They were diluted by a factor of 10^5 in methanol, and ultrasonicated for 20 mins to break up any agglomerates. 1 mL of each solution was loaded into a cuvette (Sarstedt, 67.741) and measured three times in quick succession (2 mins between measurements). The same sample was measured three times again after 15 minutes to examine the stability of the diluted solution.

4.3.4 Thermogravimetric Analysis

Thermogravimetric analysis (TGA) applies a heating profile (e.g., isothermal hold, linear ramp etc.) to a sample and measures the change in mass over time. This gives information about the ratio of volatile and non-volatile components, as well as thermal degradation of the sample in different atmospheres. A Perkin Elmer TGA 4000 with the Pyris Manager software was used to create custom heating profiles for each analysis. Before starting, the included alumina crucible (part N5200040) was heated to $T > 1000$ °C with a butane torch to burn off any contaminants.

20 µL of $Ink_{Ag,ND}$, $Ink_{Ag,XTPL}$, and $Ink_{Ag,ANP}$ were individually loaded into the crucible and subjected to a temperature ramp of 30-500 °C at rate of 10 °C min^{-1} with a hold at 100 °C for 20 hrs and a final hold at 500 °C for 1 hr in a nitrogen atmosphere to measure the relative weights of the solvent, organic stabilisers, and silver content. The 20-hour hold at 100 °C was found to be sufficient to remove all solvent ($T = 230$ °C is the boiling point for the solvent in $Ink_{Ag,ND}$ & $Ink_{Ag,XTPL}$, and

$T = 256$ °C for the solvent $\text{Ink}_{\text{Ag,ANP}}$). The second hold at 500 °C removes the remaining organic matter, whilst the nitrogen atmosphere prevents oxidation.

4.3.5 Rheology Measurements

To confirm the inks' printability, a Malvern Kinexus Pro rotational rheometer was used to measure their viscosity at 20 °C, 40 °C, or 55 °C with cone and plate geometry at a working distance of 0.2 mm. The sample is held between a stationary plate, whilst the cone is rotated at a set shear rate, γ_r. The shear stress, τ, exerted on the cone as it rotates whilst in contact with the liquid is measured to calculate viscosity, η:

$$\eta = \frac{\gamma_r}{\tau} \tag{4.2}$$

Shear rate was ramped up from 0.1 s^{-1} to 100 s^{-1}, with five samples taken per decade and a 2 s ramp between decades. The viscosity reached a constant minimum around 100 s^{-1}, and this value was used as the ink's viscosity during printing.

The density of the inks was measured by weighing 200 µL deposited by an Eppendorf pipette, with an analytical balance (ABT 100-5M, Kern & Sohn GmbH).

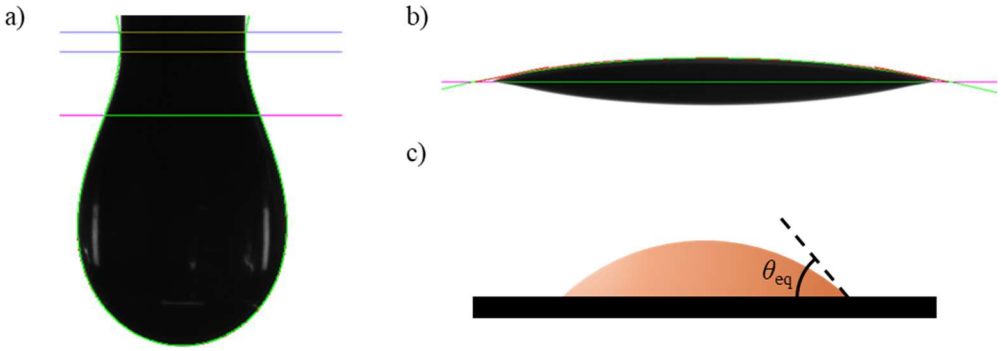

Figure 4.5: (a) *Screenshot of a backlit drop of $\text{Ink}_{\text{Di,ND}}$ hanging from a needle from the analysis software for the pendant drop method. The blue and pink lines are placed by the user to define the needle without ink, the interface between needle and ink, and the ink drop itself (pink line). The green curve is the calculated outline according to the Fabry-Laplace model used to estimate the surface tension.* ***(b)*** *Screenshot of a backlit drop of $\text{Ink}_{\text{Di,ND}}$ on glass from the analysis software for the surface tension. The pink and green line represents the surface of the glass, and the green curve is the outline of the ink drop detected by the software. The red line is the tangent to the surface of the drop at the interface with the glass.* ***(c)*** *Schematic of the definition of the surface contact angle (θ_{eq}) for a fluid droplet (orange) on a solid surface (black). The dashed line is tangent to the droplet at the point it interfaces with the solid surface.*

The surface tension of each ink and the corresponding contact angle on glass microscope slides were measured with a Krüss Drop Shape Analyser (DSA) 100E. Surface tension was measured using the pendant drop method. Each ink was placed in a 1 mL syringe with a 1.25 mm diameter metal needle, and 10 μL increments of ink were expelled until the drop was on the verge of falling. The image of the backlit liquid was then analysed in the accompanying software to extract the surface tension from shape of the drop's profile. Since the technique relies on illumination, photo-initiated inks were made without photo-initiators to avoid curing during measurement. The average result of 5 separate tests is reported for each ink. Drops for contact angle measurements were similarly produced and analysed.

4.3.6 Electron Microscopy

Electron microscopy (EM) takes advantage of the short wavelength of high-energy electrons to image samples with resolutions as low as 0.2 nm. A high voltage beam of electrons is accelerated, focused, and scanned over a sample with a series of shaped electromagnetic fields. For scanning electron microscopy (SEM), secondary electrons (SE) and backscattered electrons (BSE) are collected. SEs are generated by excitation of valence electrons within the sample and come from the top 50 nm of the sample, so are very sensitive to topography. BSEs are from inelastic collisions deeper within the sample, so are sensitive to topography and the atomic number of the atoms with which the beam collides [278].

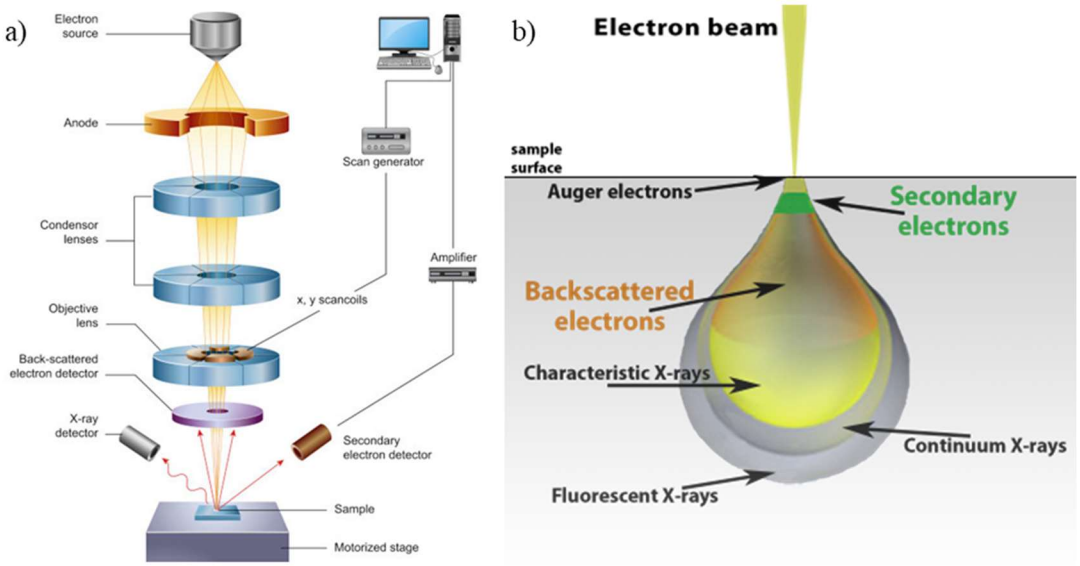

Figure 4.6: ***(a)*** *Schematic of the electron generation, focussing, and detection in a scanning electron microscope (SEM) column.* ***(b)*** *A diagram of the interaction volume of an SEM, showing from which part of the sample different signal types originate. Both reproduced from [279].*

A Hitachi SEM TM3030 with a Deben sprite multi axis stage controller and tilt attachment was used in BSE mode with a 15 kV accelerating voltage. A JEOL JSM IT-200 SEM was also used for higher resolution imaging of 1-20 drop stacks of $Ink_{Ag,XTPL}$.

A Zeiss Crossbeam 550 (resolution 1.6 nm) was used for cross-sectioning and imaging of 10-drop stacks of $Ink_{Ag,ND}$ drops on ITO coated glass. Image acquisition was conducted employing the Secondary Electron-Secondary Ion (SESI) detector, set at 2 kV and 200 pA, while maintaining a working distance of 5 mm. This technique fires a beam of ions similarly to the electron beam of the SEM, but when the ions impact the sample, they eject atoms from the sample, milling a face parallel to the beam. FIB-SEM was performed at the Nanoscale and Microscale Research Centre by Dr Negar Gilani.

In transmission electron microscopy (TEM) the sample is exposed to a beam of electrons, and transmitted electrons are detected. Contrast in the image is formed by

fluctuations in the electron density of the sample. A TEM can achieve ~0.2 nm resolution, capable of resolving atomic crystal structures.

TEM was performed by Dr Michael W. Fay at the Nanoscale and Microscale Research Centre, University of Nottingham on a JEOL 2100+ at an operating voltage of 200 kV. Samples of AgCite^{TM} 90072 were diluted by a factor of 2000 in IPA and dried to form a single layer of particles; where the beam hits a nanoparticle it is scattered, and that area of the image appears darker as the electrons are diverted away from the detector. A DENSsolutions Wildfire S3 heating cheap was used to investigate the morphology and sintering of the nanoparticles as the temperature was ramped from 140 °C to 250 °C at 1 °C min^{-1}. Fiji ImageJ [280] was used to extract the particle shapes from a TEM image before heating (**Figure 4.7**). First, a median filter of radius 3 was applied to smooth out pixellation artefacts without changing the overall shape [281], as well as remove background signal that was triggering the particle detection algorithm used later. This was followed by thresholding to create a binary image using the built-in "MinError" algorithm. One particle was incorrectly broken up by the thresholding and re-filled manually. The built-in watershed algorithm then separated clumps of particles that were touching before the particles were detected as individual black regions. Particles touching the edge of the image were excluded.

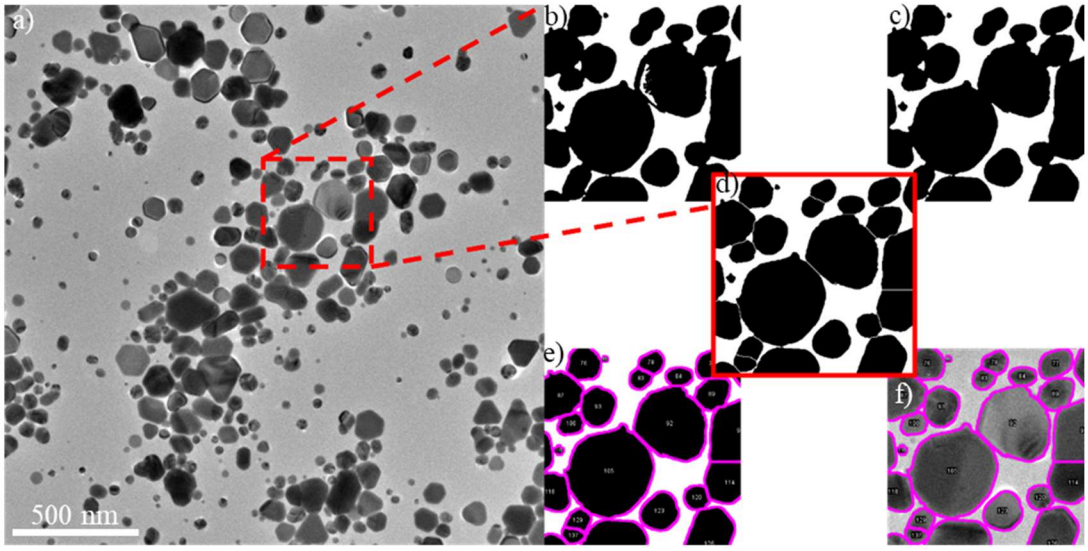

Figure 4.7: *The steps to detecting and defining the outline of particles in an image using Fiji ImageJ. The dashed red region has been chosen to best illustrate the full process, but* ***(a)*** *the entire image as taken with the transmission electron microscope was analysed. A median filter of radius 3 was first used to smooth out the background and reduce pixellation artefacts. Then,* ***(b)*** *the built-in "MinError" thresholds the image, turning the particles black and the background white.* ***(c)*** *Artificial holes introduced by the thresholding were filled in – this was only required on the single particle pictured.* ***(d)*** *A watershed algorithm separated clumps of touching particles, then* ***(e)*** *contiguous regions of black were detected as particles, ignoring those intersecting with the edge of the image.* ***(f)*** *The detected particles' outlines are also shown superimposed over the original image.*

4.3.7 Optical Imaging

Optical micrographs were taken using a Nikon Eclipse LV100ND optical microscope with a Nikon Digital Sight DS-Fi2 camera, with a 5×, 10×, or 20× objective lens. The same was used to measure features such as sample width and distance between contacts. Images were also taken with Canon EOS 60D DSLR camera with one of the following lenses: Canon EF-S 17-85mm f/4-5.6 IS USM, Canon EF-S 18-55mm f/3.5-5.6 IS STM, or Canon EF 100mm f/2.8 Macro USM.

4.3.8 Surface Profilometry

Surface profilometry is used to measure the surface topology of a sample. Coherence scanning interferometry is one such technique which relies on a beam of white light interfering with itself upon reflection from the sample. The focal plane of the light starts above the sample, and as it moves down the coherence of the highest points on that sample will peak first. This produces a height coordinate at each pixel that

corresponds to the surface of the sample. It offers a non-destructive method to evaluate surface roughness and sample thickness with resolution below 1 nm.

Measurements were performed by Mr Nathan Roberts, Dr Adam Thompson, and Mr Ahmet Koca at the Manufacturing Metrology Team, University of Nottingham using a Zygo NewView NX2. The data was analysed in the Mountains software with the assistance of Dr Geoffrey Rivers (Centre for Additive Manufacturing, University of Nottingham) using the parameters listed in **Table 4-3**. The chosen measurement for surface roughness according to ISO 25178-2:2012 is the root mean square height, *Sq*:

$$Sq = \sqrt{\frac{1}{A}\iint_A (z(x,y)-\bar{z})^2} \tag{4.3}$$

where A is the projected surface area onto the x-y plane, and z is the height of the sample at a given point. Some analysis was also performed with custom MATLAB R2021a scripts.

Table 4-3: *Parameters for estimating Sq of samples with the Zygo NewView NX2. NA – numeric aperture, LR = lateral resolution, PS = phase shift, FoV = field of view.*

Component	**Parameter**	**Value**	**Unit**
White light source	nominal wavelength	570	nm
5.5× objective	NA	0.15	-
	LR	1.90	µm
	PS	1.56	mm
	FoV	1.56 × 1.56	mm × mm
Sq parameters	S-filter nesting index	2	µm
	L-filter nesting index	0.9	mm

4.3.9 Atomic Force Microscopy

Atomic force microscopy (AFM) is used to measure a wide variety of surface properties, but particularly surface topology at sub-atomic resolution. The most common mode for this measurement is peak force tapping mode, where a sharp tip (radius <10 nm) mounted to a cantilever is oscillated up and down. A laser is reflected off the back of the cantilever onto a 4-quadrant photodetector to track its motion (**Figure 4.8a**). The tip is then lowered onto the sample, until it makes contact at the bottom of its oscillation, which changes its motion. This change in motion is used to calculate the peak force on the tip. The tip is scanned over the surface and the height of the base of the cantilever is adjusted with a piezoelectric transducer, until the peak force equals a set target (**Figure 4.8b**). The height of the base is then recorded at each measurement point over the sample, creating a point cloud of the sample's surface.

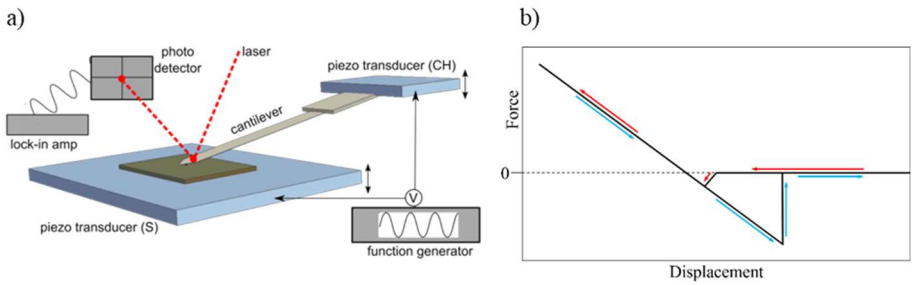

Figure 4.8: (a) *Schematic of the layout of an atomic force microscope tip and laser measuring system, reproduced from [282].* ***(b)*** *A schematic of the forces imposed on the AFM tip as it approaches (red arrows) and retreats (blue arrows) from the sample surface. The tip starts above the surface (maximum displacement), with no force applied by the surfaced. When it gets close, Coulombic forces attract it to the surface until it is in contact. As the tip keeps moving downwards, it pushes against the surface, which pushes back on the tip, until it reaches its lowest point (minimum displacement). As it retreats, Coulombic forces keep it adhered to the surface, until the tension in the cantilever is sufficient to pull it off.*

An AIST NT Smart SPM with Multi75 (Budget Sensors) tip (tip radius 10 nm, resonant frequency of F = 83 kHz, amplitude of 20 nm) was used to image the surface of printed AgNP ink, both sintered and unsintered for t_{sint} = 6.75 hours at T_{sint} = 140 °C to investigate the effects of sintering on particle morphology. Measurements were performed by Dr J Kerfoot, Nanoscale and Microscale Research Centre, University of Nottingham.

4.3.10 Electrical Characterisation

The electrical conductivity of samples was measured in a four-terminal geometry (**Figure 4.9**) to correct for resistance from contacts and the wires [283]. The resistance of the sample using this four-terminal measurement, R_{4T}, is equal to the gradient when the voltage between the inner contacts is plotted against the current.

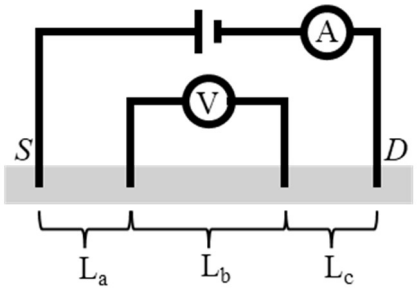

Figure 4.9: *Schematic of a four-terminal measurement. Four contacts are wired (black) onto the sample (grey) as shown. A voltage is applied between the source (S) and drain (D) contacts and varied over the given range. The current is measured between the S and D contacts, as well as the voltage between the two inner connections.*

The electrical conductivity, σ, is calculated as:

$$\sigma = \frac{R_{4T} A_c}{L_b} \tag{4.4}$$

where A_c is the cross-sectional area of the sample. In 3D printing, σ is typically anisotropic and is therefore labelled with a directional subscript. Particularly, the vertical direction has a lower conductivity due to impurities segregating in between layers, so it is expected that $\sigma_z < \sigma_{xy}$, where the xy subscript denotes the in-plane conductivity (since σ is often close to isotropic between the x and y directions). The contact resistance, R_C, can be calculated as:

$$R_C = \frac{1}{2}\left[R_{SD} - R_{4T}\left(\frac{L_a+L_b+L_c}{L_b}\right)\right] \tag{4.5}$$

where R_{SD} is the resistance between the source and drain contact.

Sheet resistance, R_s, is the resistance of a square of material with a certain thickness, t, given by:

$$R_s = \frac{1}{\sigma t} \tag{4.6}$$

To measure the conductivity of the printed samples, silver liquid adhesive (RS PRO, 186-3000) contacts were added and allowed to dry for a minimum of 24 hours. A four-probe micropositioner system (Micromanipulator 450PM) was used to place tungsten probes (Micromanipulator 7B-5) with a tip radius of 0.5 mm on top of the contacts. A microscope view was used to allow for precise placement. The system also used a vacuum pump to hold the sample and micropositioners in place during the measurement. The probes were connected to two Keithley 2401 Sourcemeters and the voltage was swept from -10 mV to +10 mV and back twice over. The distance between the connections on the sample, as well as the sample widths, were measured using a Nikon Eclipse LV100ND optical microscope with a Nikon Digital Sight DS-Fi2 camera. Measurements were made on at least three identical samples, and values are reported as the mean ± standard deviation.

4.3.11 Relative Permittivity Testing

Dielectric properties of samples made from silver embedded in a polymer matrix were tested by Dr Thomas Whittaker and Prof William Whittow, Wireless Communications Research Group, University of Loughborough. The samples were made to fit into the aperture of a WR90 waveguide with side lengths of 10.16 mm × 22.86 mm and thickness of 1.27 mm. An Anritsu MS46522B Vector Network Analyzer (VNA) (**Figure 4.10a**) was used to generate a signal and feed the waveguide over the frequency range 8-12 GHz. The waveguide utilises the TE_{10} mode, where the polarisation of the electric field aligns with the X-axis of the printer (**Figure 4.10b**).

Before conducting the measurements, the VNA was calibrated with the Line-Reflect-Line calibration method with an empty sample holder. This moves the

reference planes of the measurement to the faces of the same and negates effects of the cables and coaxial to the waveguide transitions. The amplitude and phase of the transmission and reflection coefficients (both forward and reverse directions) were used to retrieve the relative dielectric constant (ε_r), electric loss tangent (tan δ_E), relative magnetic permeability (μ_r), and magnetic loss tangent (tan δ_M) according to the Nicolson-Ross-Weir method [284,285]. Both the forward and reverse measurement data are used to compute the dielectric properties of these samples, hence producing two sets of material characterisation data for each measurement. Each sample was measured six times, and was removed, rotated 180° about the Y-axis, and reinserted after each measurement. Reported values at each frequency point are averaged across the six material data sets. Furthermore, the dielectric constant over the entire frequency range is averaged, with an error equal to the standard deviation of the corresponding data.

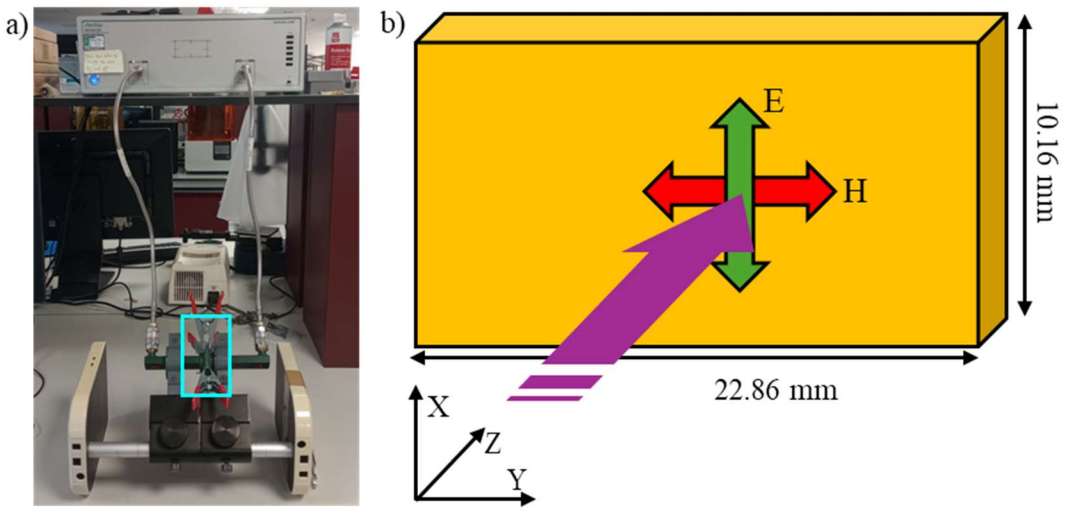

Figure 4.10: (a) *Image of the vector network analyser. The grey box at the top sends signals through optical fibres inside the flexible conduit, which pass through the waveguide clamped in the holder highlighted by the rectangle in cyan.* ***(b)*** *Schematic showing the electric (E, green) and magnetic (H, red) polarisation of the input signal (purple) as it passes through the waveguide. The axes represented here correspond to the LP50 printer axes.*

5 INK CHARACTERISATION

This work uses inks to carry conductive and insulating materials, with some being commercially available and others being produced in-house. This chapter describes the formulation of the in-house inks, the characterisation of the commercial inks, and the effect on the resulting material properties by optimising printing and post processing conditions. The conductive inks are all formulated with silver nanoparticles, and the insulating materials are all UV-curable monomers.

5.1 Conductive Silver Nanoparticle Inks

The three commercial silver-nanoparticle (AgNP) inks have physical properties that are already optimised for inkjet printing (**Table 5-1**). They are all printable ($1<Z<10$) when the ink is at 40 °C in both the Spectra SE-128 AA and the Xaar-128 printheads. $Ink_{Ag,ND}$ and $Ink_{Ag,XTPL}$ use the same solvent (2-(2-butoxyethoxy) ethanol), hence have a similar viscosity, but $Ink_{Ag,ND}$ has a high silver loading at 47.6 wt.% compared to 35.2 wt.% for $Ink_{Ag,XTPL}$, which leads to a higher density. $Ink_{Ag,ANP}$ uses a different solvent with a lower viscosity (triethylene glycol monoethyl ether) and has the lowest silver loading of 28.2 wt.%, and a higher ligand content (1.6 wt.% compared to 0.9 wt.% for $Ink_{Ag,ND}$ and $Ink_{Ag,XTPL}$).

Table 5-1: *Physical properties of $Ink_{Ag,ANP}$, $Ink_{Ag,ND}$ and $Ink_{Ag,XTPL}$. The remaining weight after the silver and ligand loading is from the ink's solvent. The first Z value is calculated for the Spectra SE-128 printhead, which has a nozzle diameter of 35 µm, and the second is is calculated for the Xaar 128 printhead, which has a nozzle diameter of 49.5 µm. Viscosity measured at 40 °C. γ_{IFT} = surface tension.*

Ink	Ag:Ligand / wt.%	Viscosity / cP	Density / g mL^{-1}	γ_{IFT} / mN m^{-1}	Z
$Ink_{Ag,ND}$	47.6 : 0.9	19.3 ± 0.2	1.30 ± 0.11	28.4 ± 0.2	1.9 ± 0.1 / 2.3 ± 0.1
$Ink_{Ag,ANP}$	28.2 : 1.6	8.15 ± 0.09	1.13 ± 0.09	24.3 ± 0.5	3.8 ± 0.2 / 4.5 ± 0.2
$Ink_{Ag,XTPL}$	35.2 : 0.9	19.3 ± 0.3	1.15 ± 0.04	21.6 ± 1.5	1.5 ± 0.1 / 1.8 ± 0.1

The solid content was measured using TGA in a N_2 atmosphere (**Figure 5.1a**). The initial mass loss was recorded at a relatively low temperature (T = 100 ° C) to avoid degradation of any solid content and to complete the evaporation of the solvent. The mass plateaus after 1000 mins. This is followed by increasing the temperature at 10 °C min^{-1} to T = 500 °C to thermally degrade the organic ligands, differentiating them from the mass of the silver content (around 7 mg in total, depending on the wt.% of the ink).

The viscosity was measured using a log ramp from a shear rate of 0.1 s^{-1} up to 100 s^{-1}. For each ink, the viscosity decreased with increasing shear rate until it plateaued above ~60 s^{-1}, which is caused by breaking of the short-range order arising from nanoparticle interactions [286]. There is also significant slip-stick behaviour at shear rates below 25 s^{-1}, which is the cause of the sharp changes in viscosity in this regime, but which is not present at higher shear rates. Since inkjet printing has a high shear rate, the value of the plateau at high shear rates corresponds well to the behaviour of the ink during jetting [130].

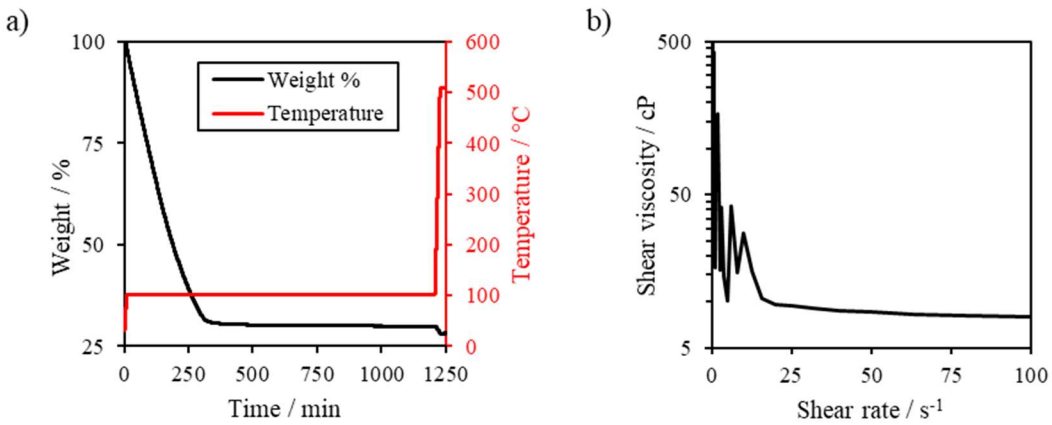

Figure 5.1: (a) *TGA trace for $Ink_{Ag,ANP}$, showing an initial solvent loss at 100 °C which plateaus after 1000 minutes, followed by loss of organic ligands by thermal degradation at 500 °C leaving only silver.* ***(b)*** *A shear rate sweep to measure the shear viscosity of $Ink_{Ag,ANP}$ at 40 °C.*

5.1.1 Nanoparticle Analysis

Nanoparticle morphology affects their properties, including their behaviour during sintering, and therefore the final electrical properties. TEM images of the inks (**Figure 5.2**) reveal that the $Ink_{Ag,ND}$ has the widest distribution of particle sizes, with a slightly angular morphology (mean diameter $d = 68 \pm 42$ nm). Nanoparticles in $Ink_{Ag,XTPL}$ have a similar morphology, but a narrower distribution of sizes (mean diameter $d = 55 \pm 14$ nm), and $Ink_{Ag,ANP}$ contains mostly spherical particles with a narrow size distribution except for a few rod-like particles (mean diameter $d = 67 \pm 18$ nm).

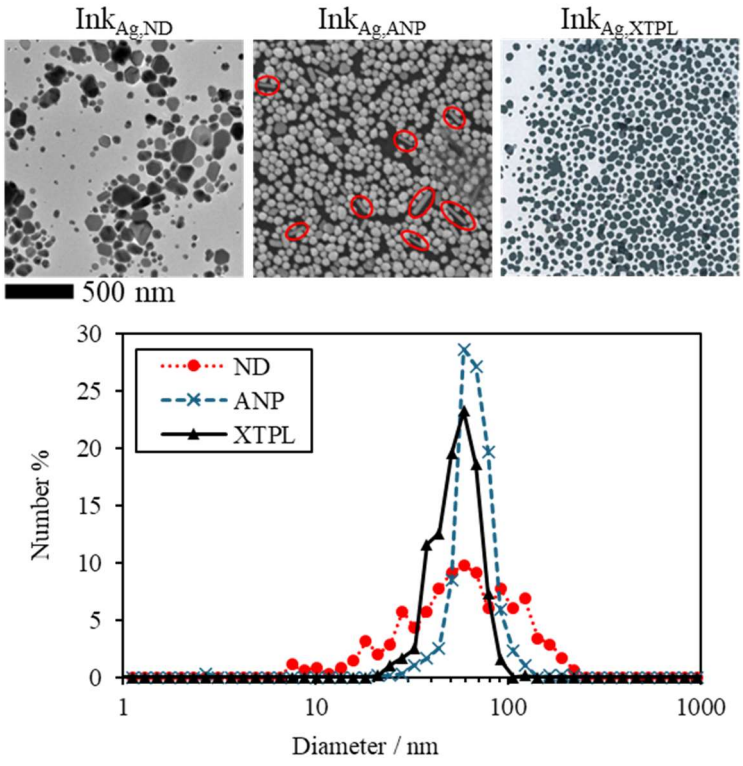

Figure 5.2: *TEM images of the silver nanoparticle inks. Imaging of $Ink_{Ag,ND}$ was performed by Dr Mike Fay (nmRC, University of Nottingham), the image of $Ink_{Ag,ANP}$ has been reproduced from [37] and the image of $Ink_{Ag,XTPL}$ has been reproduced from [287]. The graph shows the particle size distribution as extracted from these images, excluding the rod-like particles in $Ink_{Ag,ANP}$ (circled in red) which were not detected by the particle detection algorithm. Lines connecting the data points have been added as a guide to the eye.*

To corroborate the TEM analysis, dynamic light scattering (DLS) measurements and UV-Vis spectra were recorded of each ink (**Table 5-2**). Both UV-Vis and TEM directly measure the size of the metallic core of the nanoparticles, with the ligands having little effect on the final result. UV-Vis measures absorption from a far larger

number of particles than are present in a single TEM image, but it is challenging to estimate a size distribution. All three inks have estimates of the mean nanoparticle diameter within the error range of the data extracted from the TEM images, which confirms that that the size distribution measured through TEM is representative.

Dynamic light scattering also measures a large number of particles and estimates a size distribution but measures the hydrodynamic diameter instead of the diameter of the nanoparticle. Therefore, it is expected that DLS will overestimate the particle diameter due to the effects of ligands and solvent interaction, which is borne out for $Ink_{Ag,ND}$ and $Ink_{Ag,XTPL}$ (**Table 5-2**). Further, scattering intensities are significantly higher for larger diameters (intensity $\propto d^6$), which is likely the reason for the much larger overestimate for $Ink_{Ag,ND}$ compared to $Ink_{Ag,XTPL}$, showing diameters of 195 ± 94 nm and 62 ± 16 nm from DLS of $Ink_{Ag,ND}$ and $Ink_{Ag,XTPL}$ respectively, compared with 68 ± 42 nm and 55 ± 14 nm from TEM.

However, DLS underestimates the size of particles with very high aspect ratios [288], since it is assumed the particles are spherical, which is not the case for $Ink_{Ag,ANP}$ (**Figure 5.2**, **Table 5-2**). This leads to the underestimation of the diameter observed, from 28 ± 9 nm from DLS measurements to 67 ± 18 nm from TEM.

Table 5-2: *Mean diameter of the nanoparticles in the three AgNP inks measured by three separate methods.*

	Diameter / nm		
Ink	**TEM**	**DLS**	**UV-Vis**
$Ink_{Ag,ND}$	68 ± 42	195 ± 94	76
$Ink_{Ag,ANP}$	67 ± 18	28 ± 9	65
$Ink_{Ag,XTPL}$	55 ± 14	62 ± 16	63

Atomic force microscopy (AFM) is capable of imaging the silver nanoparticles to a high resolution but, unlike TEM, it is able to image the surface of a thick layer of

nanoparticles. Therefore, AFM was used to investigate the morphology of the nanoparticles after sintering at T_{sint} = 140 °C for t_{sint} = 6.75 hours (**Figure 5.3**). The nanoparticles in $Ink_{Ag,ND}$ are more angular and with flat facets compared with the more rounded nanoparticles of the other two inks. Further, the nanoparticles appear to tesselate more precisely in $Ink_{Ag,ND}$, leading to a larger area of contact for sintering, which can be seen in the gradual height transitions between nanoparticles, compared to the quick fall off in height at the edge of a particle. The nanoparticles in $Ink_{Ag,ANP}$ were difficult to image due to what we conjecture is a large amount of organic matter on the surface – most likely residual PVP ligands, since $Ink_{Ag,ANP}$ has the highest ligand content of the inks. These images were not taken last in order, so the fuzzy look is not an artefact from tip contamination. This is backed up by the literature, which has shown significant segregation of organic ligand to the surface of this ink [37], which also has the highest amount of organic matter by weight of any of the three inks.

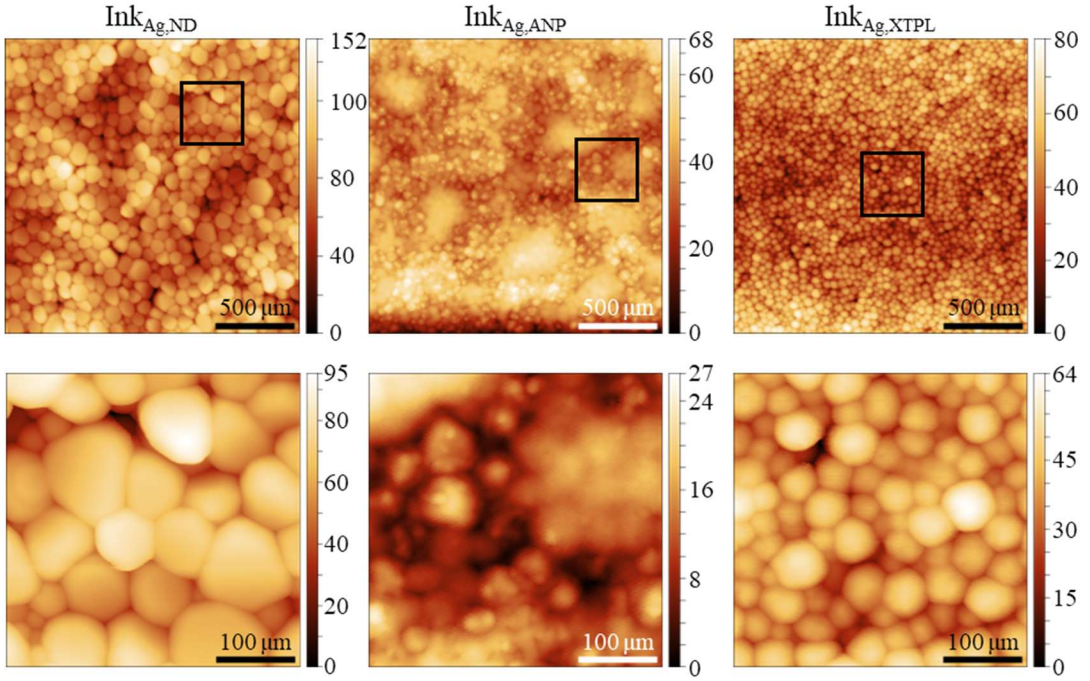

Figure 5.3: *AFM height maps of the three silver nanoparticle inks after sintering at T_{sint} = 140 °C for t_{sint} = 6.75 hours. The lower images are magnified height maps of the corresponding areas marked as black squares in the above images. The colour scales are in nm. Imaging performed by Dr James Kerfoot (nmRC, University of Nottingham).*

5.1.2 Electrical Characterisation

Nanoparticles can be sintered significantly below their bulk melting point (962 °C for silver) due to their very high surface energy [2]. Bulk silver has an electrical conductivity of $\sigma = 6.3 \times 10^7$ S m^{-1}, whereas the sintered nanoparticles have a conductivity of approximately 20 % of bulk ($\sigma_{xy} = (2.9 \pm 0.6) \times 10^7$ S m^{-1} for $Ink_{Ag,ND}$ sintered at T_{sint} = 200 °C for t_{sint} = 2 hours), depending on the ink and the post processing (**Figure 5.4**), due to organic residues and incomplete connectivity between nanoparticles. Sintering at higher temperatures and for longer periods of time improves the connectivity – and thus the conductivity – due to merging of the nanoparticles driven by a reduction in surface energy. Following sintering for t_{sint} = 6.75 hrs, σ_{xy} of $Ink_{Ag,ND}$ increases at all temperatures, with increasing temperatures up to T_{sint} = 170 °C, after which no further increase of T_{sint} resulted in improved conductivity (**Figure 5.4a**). Initially, the project plan was to compare the printing results between the PixDRO LP50 and the Nano Dimension Dragonfly printers. The latter sinters at T_{sint} = 140 °C, so this temperature was chosen for further work to ensure a fair comparison, despite the lower (although still high) overall conductivity of $\sigma_{xy} = (1.05 \pm 0.05) \times 10^7$ S m^{-1}. Due to significant unforeseen machine downtime on the Dragonfly printer, it wasn't possible to perform these comparisons, but this wasn't known when selecting T_{sint} for the first set of experiments. Therefore, to maintain consistency across all experiments, T_{sint} = 140 °C was kept so as not invalidate the earlier work.

Increasing the time of sintering (at T_{sint} = 140 °C) also improves σ_{xy}, up to t_{sint} = 6.75 hours, after which no significant change was observed (**Figure 5.4b**), so this was chosen as the sintering time for further work. Under these conditions, $Ink_{Ag,ND}$ has $\sigma_{xy} = (1.05 \pm 0.05) \times 10^7$ S m^{-1}, $Ink_{Ag,XTPL}$ has $\sigma_{xy} = (1.65 \pm 0.07) \times 10^7$ S m^{-1}, and

$Ink_{Ag,ANP}$ exhibits $\sigma_{xy} = (0.9 \pm 0.3) \times 10^7$ S m^{-1}, corresponding to 17 %, 26 %, and 14 % of bulk silver conductivity.

All three inks exhibit a significantly lower vertical conductivity (σ_z) compared to their in-plane conductivity (σ_{xy}) (**Figure 5.4c**), where $Ink_{Ag,ND}$ has $\sigma_z = (4 \pm 1) \times 10^6$ S m^{-1}, $Ink_{Ag,XTPL}$ has $\sigma_z = (2.1 \pm 0.4) \times 10^6$ S m^{-1}, and $Ink_{Ag,ANP}$ has $\sigma_z = (4.5 \pm 0.9) \times 10^6$ S m^{-1}. This is due to accumulation of the ligands at the top of each layer, which creates an insulating barrier to vertical conductivity [37]. This is contrary to the findings of Trindade et al. [37], which saw an anisotropy of three orders of magnitude, despite having similar results for in-plane conductivity, $\sigma_{xy} = (9 \pm 3) \times 10^6$ S m^{-1} at $T_{sint} = 150$ °C. This difference is likely due to the geometry of their sample: a 200-layer square instead of a micropillar. This could cause differences in the drying behaviour and subsequently the movement of the ligands within the ink as it dries. Further, they were unable to print sufficiently high to fit four terminals, which may have caused significant contact resistance which is difficult to account for.

$Ink_{Ag,XTPL}$ has the highest anisotropy ($\sigma_{xy}/\sigma_z = 7.79$) anisotropy, with $Inkg_{Ag,ND}$ in second ($\sigma_{xy}/\sigma_z = 2.55$) and $Ink_{Ag,ANP}$ the least ($\sigma_{xy}/\sigma_z = 1.68$). This shows that even the reduced ligand content of $Ink_{Ag,ND}$ is insufficient to alleviate the problem of conductivity anisotropy – instead, there needs to be some mechanism to remove the ligands from the surface of each layer as it is printing.

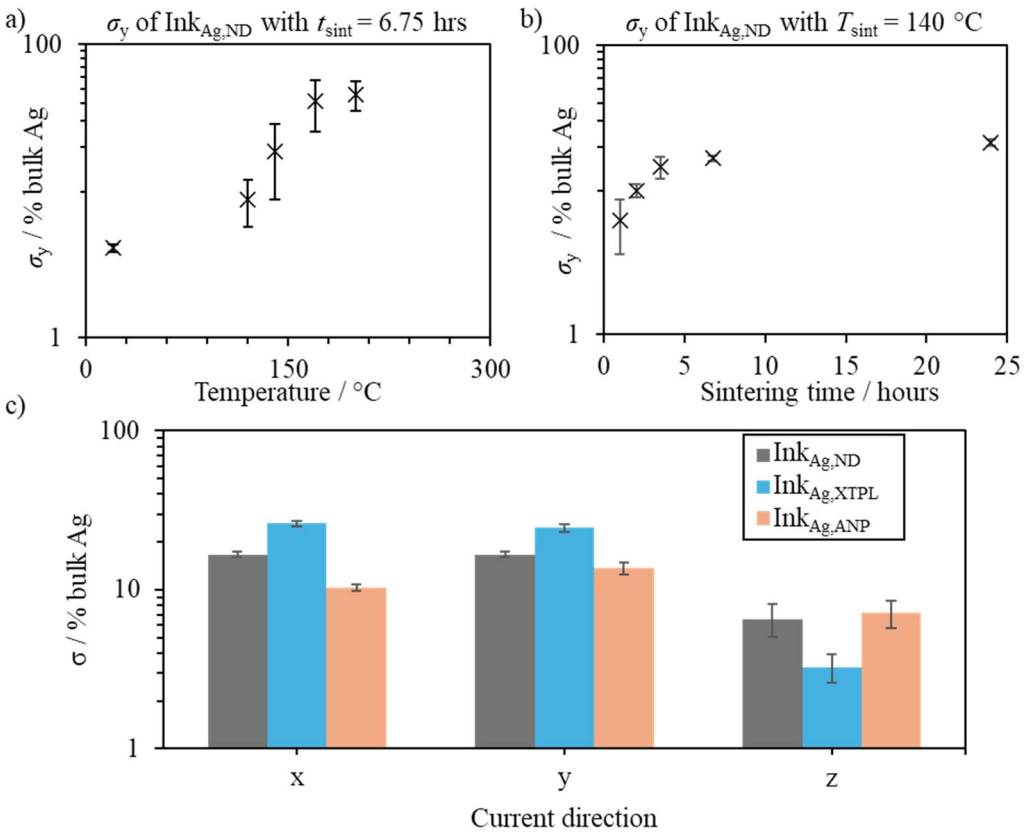

Figure 5.4: *Electrical conductivity in the Y direction of $Ink_{Ag,ND}$ and its dependence on* ***(a)*** *sintering temperature for a constant t_{sint} = 6.75 hours,* ***(b)*** *sintering temperature for a constant T_{sint} = 140 °C. The electrical conductivity for all three AgNP inks is shown in* ***(c)*** *for different directions of current flow, with error bars representing the standard deviation from a sample size of three. All samples were printed on the LP50 with Spectra SE-128 AA printheads, where the primary printing direction corresponds to the Y axis and the Z axis is vertical.*

5.2 Dielectric Polymer Inks

The polymer inks used in this work function as a supportive matrix for printing 3D silver structures and as a dielectric medium for the design of radiofrequency metamaterials. Polymers used should be stable at the elevated temperatures required for silver ink sintering, have a large relative permittivity constant (ε_r) and low dielectric loss at GHz frequencies.

All four polymer inks selected for this work are UV-curable acrylates, whose monomers form polymers by free-radical polymerisation. A free radical is created when an initiator molecule absorbs a UV photon, which then reacts with an acrylate monomer (**Figure 5.5a)**. This creates an acrylate free radical, which can react with

further monomers in the process of chain polymerisation (**Figure 5.5b**). The process terminates by the combination (**Figure 5.5c**) or disproportionation (**Figure 5.5d**) of two free radicals.

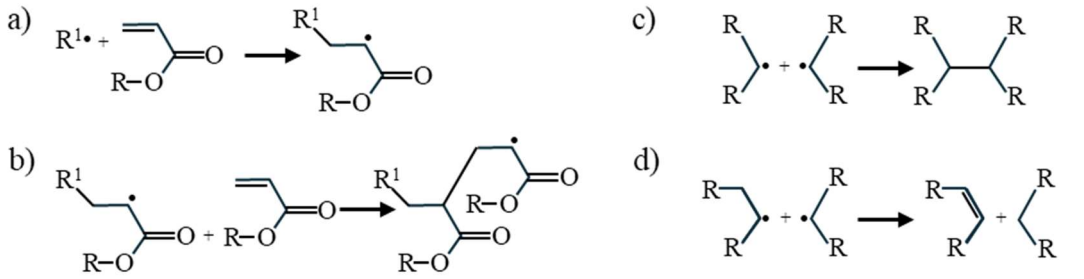

Figure 5.5: *Free radical polymerisation of acrylate monomers.* ***(a)*** *The free radical (R^1•) formed by the absorption of a photon by an initiator molecule reacts with an acrylate monomer.* ***(b)*** *That same acrylate monomer now acts as the free radical, reacting with a second acrylate monomer to start the process of chain polymerisation. This reaction continues until it is terminated by* ***(c)*** *combination or* ***(d)*** *disproportionation of two free radicals.*

ε_r is a measure of the ability of a dielectric material to store energy in an electric field. It is relatively constant in the microwave/GHz regime since these frequencies are far from any modes by which materials can create a change in polarisation (electronic/ionic conduction < 10^0 Hz; dipole orientation < 10^6 Hz; atomic vibration >10^{10} Hz; electronic vibration > 10^{16} Hz) [289]. The loss factor (tan δ_E) is a measure of the dissipation of the energy which would otherwise be stored, and at these frequencies in these materials is primarily from lossy relaxation of dipoles reorienting to align with the field. $Ink_{Di,ACMO}$ has the highest $\varepsilon_r = 3.36$ but the tan $\delta_E = 0.055$ (**Table 5-3**) is too large for high performance metamaterials. $Ink_{Di,TPGDA}$, $Ink_{Di,EGDPEA}$, and $Ink_{Di,ND}$ have similar ε_r = 2.78, 2.76, and 2.76 respectively, but $Ink_{Di,TPGDA}$ has the highest tan $\delta_E = 0.024$ out of these three (compared to 0.016 and 0.013 $Ink_{Di,EGDPEA}$, and $Ink_{Di,ND}$ respectively). Therefore, $Ink_{Di,EGDPEA}$, and $Ink_{Di,ND}$ were selected for further work.

Table 5-3: *Dielectric properties of the four dielectric inks at 10 GHz.*

Ink	ε_r	**tan** δ_E
$Ink_{Di,EGDPEA}$	2.76	0.016
$Ink_{Di,ACMO}$	3.36	0.055
$Ink_{Di,TPGDA}$	2.78	0.024
$Ink_{Di,ND}$	2.76	0.013

5.2.1 Printability

The rheology of the four polymer inks was characterised to ensure their printability (**Table 5-4**). Such inks often require heating to jet consistently, so this study was conducted at several temperatures. First at room temperature, which is still printable for dielectric inks, but the viscosity is sufficiently high that it is difficult to purge ink into the nozzles. Second at T = 40 °C, which is the temperature at which the printheads equilibrate when printing over a heated substrate at T_{sub} = 70 °C in the LP50, and third at T = 55 °C, which is the recommended ink temperature for $Ink_{Di,ND}$ [168]. Therefore, $Ink_{Di,ND}$ was printed at T_{ink} = 55 °C, but the others were printed at T_{ink} = 40 °C to reduce satellite drops when printing for a long time (>1 hr).

Table 5-4: *Rheology of the four UV-curable dielectric inks. Due to the lack of UV shielding, surface tension (γ_{IFT}) was measured without any initiator present for all inks except for $Ink_{Di,ND}$. The first Z value is calculated for the Spectra SE-128 AA printhead, which has a nozzle diameter of 35 μm, and the second is is calculated for the Xaar 128 printhead, which has a nozzle diameter of 49.5 μm. *The surface tension of this ink is not available from the manufacturer and could not be measured in-house (see* ***Chapter 4.3.5****).*

Ink	Temperature / °C	Viscosity / cP	Density / g mL^{-1}	γ_{IFT} / mN m^{-1}	Z
$Ink_{Di,ND}$	20	45.7 ± 0.3	1.04 ± 0.03	—*	—
	40	8.5 ± 0.2			—
	55	9.9 ± 0.2			—
$Ink_{Di,EGDPEA}$	20	30.2 ± 0.3	0.94 ± 0.04	34.3 ± 0.1	1.11 ± 0.04/ 1.32 ± 0.04
	40	12.2 ± 0.3			2.8 ± 0.1/ 3.3 ± 02
	55	7.3 ± 0.3			4.6 ± 0.3/ 5.5 ± 0.3
$Ink_{Di,TPGDA}$	20	18.8 ± 0.3	0.965 ± 0.007	24.3 ± 0.2	1.52 ± 0.04/ 1.81 ± 0.04
	40	8.3 ± 0.4			3.4 ± 0.2/ 4.1 ± 0.2
	55	5.3 ± 0.3			5.4 ± 0.3/ 6.4 ± 0.4
$Ink_{Di,ACMO}$	20	13.9 ± 0.3	1.12 ± 0.02	33.4 ± 0.4	2.6 ± 0.1/ 3.1 ± 0.1
	40	6.4 ± 0.4			5.6 ± 0.4/ 6.7 ± 0.5
	55	4.1 ± 0.2			8.8 ± 0.6/ 10.5 ± 0.7

Since printing utilises an elevated substrate temperature to ensure evaporation of the AgNP ink, there is a significant difference in the spreading of the dielectric ink between the first and last swathes before it is pinned with the UV light. A single layer was printed with a single-pixel hole every third pixel. The pattern was printed with a single nozzle left-to-right before being cured with the UV light, so the left side of the print had significantly more time to heat up and subsequently spread further than occurred on the right-hand side, leading to closure of the holes on the left side, and portions of the ink un-merged on the right side (**Figure 5.6a**). This lack of merging also shows on the right side of multilayer prints (**Figure 5.6b**). The LP50 has a built-

in function to change the secondary print direction, so prints using the dielectric inks used the strategy of alternating each layer being printed from left-to-right or right-to-left to cancel out this anisotropy.

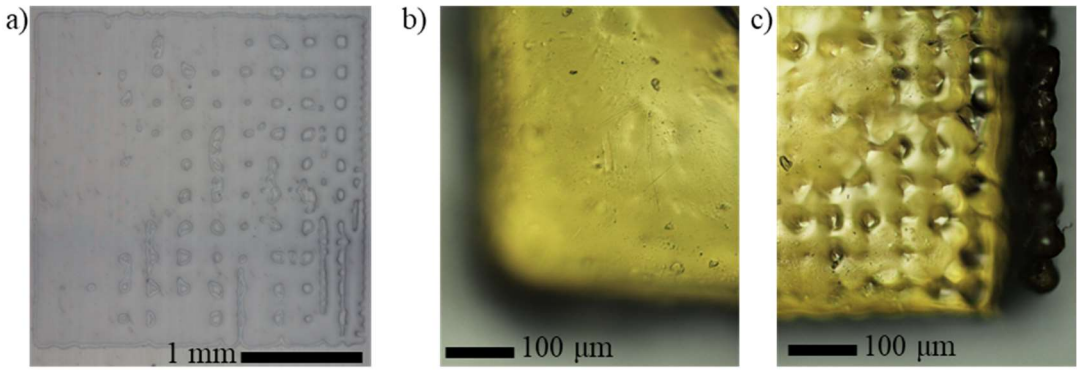

Figure 5.6: *Optical images showing the non-uniformity of $Ink_{Di,EGDPEA}$ when printed with a Spectra SE-128 printhead at an elevated substrate temperature, T_{sub} = 70 °C.* ***(a)*** *A single layer of ink with 1-pixel holes spaced 3 pixels apart, which was printed left-to-right, causing the holes on the left to close up, and* ***(b)*** *the top-left corner and* ***(c)*** *top-right corner a 400-layer print of a continuous polymer block, also printed left-to-right, where drops on the right-hand side have not been able to merge before being pinned.*

5.2.2 Thermal Stability

The glass transition temperature (T_g) of a polymer is a key parameter for its thermal stability. When curing from a liquid to a solid, cross-linking bonds are formed which reduce the free space the polymer chains occupy, and therefore there is some shrinkage. When the next layer is printed on top and cured, it reacts with the preceding layer, and also shrinks, creating in-plane compressive forces in the lower layer and in-plane tensile forces in the upper layer. These forces build up with each layer, with the total effect of the forces at the end of the print to cause the print to bend upwards. If the polymer is above its T_g during the process of printing, post-processing (especially sintering), then there is sufficient thermal energy for the polymer chains to move to accommodate these forces, thus warping the polymer to allow the residual stresses to relax. Two of the dielectric inks are homopolymers: $Ink_{Di,TPGDA}$ has T_g = 55 °C [290], and $Ink_{Di,ACMO}$ has T_g = 142 °C [291]. $Ink_{Di,ND}$ is a proprietary mixture of monomers,

but the overall T_g = 162 °C [205]. $Ink_{Di,EGDPEA}$ is a copolymer of EGDPEA and TCDMDA, so its T_g can be estimated using the Fox equation:

$$\frac{1}{T_g} = \frac{w_1}{T_{g,1}} + \frac{w_2}{T_{g,2}} \quad (5.1)$$

where w is the weight fraction of the given monomer, and T_g is calculated in kelvin [292]. A homopolymer of EGDPEA has T_g = 19 °C, and TCDMDA has T_g = 160 °C [293], so the overall glass transition temperature of $Ink_{Di,EGDPEA}$ is T_g = 39.3 °C. Since the two monomers are well soluble in each other and thoroughly mixed prior to jetting, it is expected that the polymer chains formed will be a random copolymer of the two monomers, hence this averaging method is applicable. If the monomers were insoluble, it would be expected that significant separation would occur resulting in two values T_g, but this is not expected since the ink is stable at room temperature without separation for >6 months. The chosen sintering temperature for the AgNP inks is T_{sint} = 140 °C, so $Ink_{Di,ACMO}$ and $Ink_{Di,ND}$ have the required thermal properties for co-printing with the AgNP inks.

5.3 Summary

Three AgNP inks were investigated for their printability, composition, and electrical conductivity. All three were found to be printable in both the Xaar-128 and Spectra SE-128 AA printheads when heated to T_h = 40 °C. $Ink_{Ag,ND}$ has the highest silver content, and joint-lowest ligand content alongside $Ink_{Ag,XTPL}$, and $Ink_{Ag,ANP}$ has both the lowest silver content and highest ligand content. The nanoparticle morphology also differed between the three inks. $Ink_{Ag,ND}$ has the widest distribution of particle sizes, with a slightly angular morphology alongside the highest mean diameter, and nanoparticles in $Ink_{Ag,XTPL}$ have a similar morphology, but a narrower distribution of

sizes with the smallest mean diameter. $Ink_{Ag,ANP}$ contains mostly spherical particles with a narrow size distribution except for a few rod-like particles, and a similar mean diameter to $Ink_{Ag,ND}$. AFM of the sintered inks showed that $Ink_{Ag,ND}$ had qualitatively better tessellation, but imaging of $Ink_{Ag,ANP}$ was difficult due to a large amount of organic matter on the surface, likely the excess ligand.

Despite these differences in composition, there was little difference in electrical performance between the three inks. $Ink_{Ag,XTPL}$ has a slightly higher in-plane conductivity than the other two ($Ink_{Ag,ND}$ $\sigma_{xy} = (1.05 \pm 0.05) \times 10^7$ S m^{-1}, $Ink_{Ag,XTPL}$ $\sigma_{xy} = (1.65 \pm 0.07) \times 10^7$ S m^{-1}, and $Ink_{Ag,ANP}$ exhibits $\sigma_{xy} = (0.9 \pm 0.3) \times 10^7$ S m^{-1}), but worse vertical conductivity ($Ink_{Ag,ND}$ $\sigma_z = (4 \pm 1) \times 10^6$ S m^{-1}, $Ink_{Ag,XTPL}$ $\sigma_z = (2.1 \pm 0.4) \times 10^6$ S m^{-1}, and $Ink_{Ag,ANP}$ $\sigma_z = (4.5 \pm 0.9) \times 10^6$ S m^{-1}). This contradicts the current literature, which had found a three orders of magnitude anisotropy with $Ink_{Ag,ANP}$, but with a different printed geometry (a large square instead of a single-drop micropillar). The discrepancy is likely due to differences in evaporation rate changing the distribution of the insulating ligand within the structure, showing that micropillars are a superior form factor if high σ_z is required.

Four dielectric inks with potential as a supportive matrix for complex silver geometries were investigated for their printability, dielectric properties, and thermal stability. All four were found to be printable over a wide range of temperatures, in both Xaar-128 and Spectra SE-128 AA printheads. At an elevated substrate temperature of T_{sub} = 70 °C, the inks spread out slowly, so the timing of the UV-pinning effects the layer morphology. When printing left-to-right, the ink on the left has more time to spread, leading to a more even layer, but small holes can close up. Ink on the right may have insufficient time to merge, leading to a bumpy surface.

Therefore, the swathe order must be alternated between layers, so that this anisotropy can be averaged out over the course of a print.

$Ink_{Di,ACMO}$ had the highest $\varepsilon_r = 3.36$ but also the highest tan $\delta_E = 0.055$ at 10 GHz, so it is unsuitable for applications at such frequencies. $Ink_{Di,TPGDA}$ also has a large tan $\delta_E = 0.024$ ($\varepsilon_r = 2.78$) at 10 GHz, but $Ink_{Di,ND}$ and $Ink_{Di,EGDPEA}$ have the lowest tan δ_E of 0.013 and 0.016, respectively, with the same $\varepsilon_r = 2.76$. Therefore, $Ink_{Di,ND}$ and $Ink_{Di,EGDPEA}$ are the best options for applications in the microwave frequency regime. However, $Ink_{Di,EGDPEA}$ has a $T_g = 39.3$ °C below that used for sintering the silver, so it can be expected to warp, as does $Ink_{Di,TPGDA}$ ($T_g = 55$ °C). $Ink_{Di,ACMO}$ and $Ink_{Di,ND}$ have a sufficiently high T_g (142 °C and 162 °C respectively) to be unlikely to warp at $T_{sint} = 140$ °C, although it is very close for $Ink_{Di,ACMO}$. Overall, $Ink_{Di,ND}$ has the best combination of dielectric properties and thermal stability for use as a supporting matrix to silver nanoparticles in microwave-frequency applications.

6 OFF THE GRID

This chapter reports on a novel printing strategy, Off the Grid (OtG), which enables refined positioning of individual droplets compared to the traditional printing strategy. This enables printing structures with feature position control smaller than the size of a single droplet, enhancing the shape fidelity of intricate designs. This strategy is extended to layer-filling patterns for improved layer coverage and customisable inter-layer positioning to control surface morphology. To exemplify the applicability of this strategy, OtG is used to produce functional designs, such as conformable circuitry and miniaturised antennae. OtG is initially developed for AgNP inks, but is transferable to different materials, including polymers on inkjet platforms, to molten metals on a MetalJet printer.

The work described in this chapter was published in Nelson-Dummett et al., "Off the Grid: A new strategy for material-jet 3D printing with enhanced sub-droplet resolution", *Additive Manufacturing Letters, 8 (2024) 100185*.

6.1 Introduction

Material jetting 3D printers typically operate on an image and spacing model, where the pattern for droplet placement is encoded as an image, with pixels representing desired positions for discrete droplets. Planar geometry is controlled primarily by the spacing of adjacent droplets [294], taking into account their size and coalescence behaviour [295–300] to form a continuous film [301]. If the spacing is not optimised, material overflow or scalloped edges and gaps are observed [237]. Since pixels are binary and equal in size, this limits the final design resolution to be equal to the drop spacing. Further, uneven distribution of material observed in traditional jetting arises from fluid dynamics, such as the coffee-ring effect, [302–306] which in turn affects

the surface morphology, shape fidelity and functional properties of printed layers. Despite the significant need to control the geometric precision and surface quality of layers deposited by material jetting [223,307,308], particularly for applications in electronics, to date there is no established strategy to address the limitations of the image-and-spacing model that can be applied to various materials and commercial printers.

6.2 Off the Grid Theory

In inkjet printing, discrete adjacent droplets are deposited using a grid with a nominal spacing required for merging (S_n) which defines the image resolution. This approach is preferred over a continuous, g-coded path for the printhead, because it allows for many nozzles (100s or 1000s in a single row, depending on the printhead) to be firing simultaneously at high frequencies, increasing the print speed. Aligning that many nozzles to a pattern with a non-linear path would be extremely complex, or often impossible. Therefore, an idealised pattern must be approximated by an aliased rendering, producing errors in curves and thin traces (**Figure 6.1a**). Take as an example printing several single-drop-wide lines using $\text{Ink}_{\text{Ag,XTPL}}$ onto PET at T_{sub} = 100 °C with the Samba cartridge, which requires S_n = 20 μm. A bitmap cannot contain a coordinate halfway between two pixels, so the spacing between these lines (encoded in the whitespace of the image) must be an integer multiple of 20 μm (**Figure 6.1b**).

Consider setting the drop spacing parameter in the printer to 4 μm. Normally this would cause the material to overflow. However, if the bitmap were created such that only every 5$^{\text{th}}$ pixel in the lines were black, drops would still be ejected at spatial intervals of 20 μm, but now the distance separating the lines can be any integer multiple of 4 μm – a 5-fold improvement (**Figure 6.1c**). In this latter scenario,

S_n = 20 µm but we have introduced a refined spacing, S_r = 4 µm, which creates a refinement factor to quantify the OtG improvement of $F_r = S_n / S_r = 5$. This control over the spacing between features is an example of controlling the negative space of a print, i.e. all of the area where the printed material isn't deposited, which is often of equal importance to controlling the geometry of the material itself. Traditionally, the negative space of the printed material is represented by the whitespace in the bitmap, so called because the colour of those pixels is literally white when displayed on a computer screen. This is not always the case in OtG, because the black pixels now only represent the position of the centre of a drop, not its full physical extent. Therefore, a white pixel close to a black pixel may represent an area that is covered by material once it is printed. Such a pixel is still referred to as whitespace, because it is coloured white, but would not represent negative space in the final print, because it is covered with material from a drop centred on an adjacent black pixel.

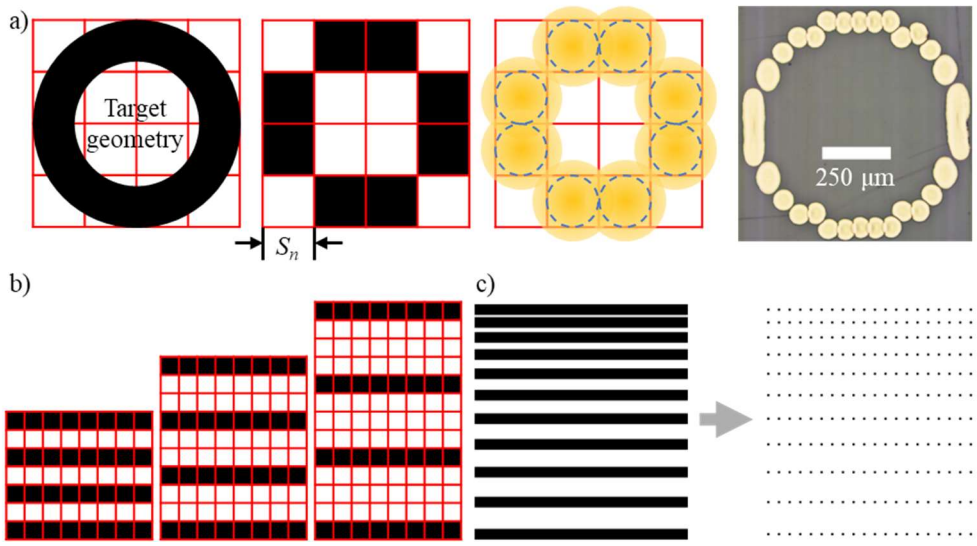

Figure 6.1: (a) *Schematic showing the rasterization that occurs when representing a small, thin annulus with a bitmap, which is required translate the smooth circle onto a fixed grid of pixels (as shown by the red grid). The yellow circles show the real-size extent of the drops, and the dashed circles show the radius required for good merging (S_n). Some pixels are only diagonally adjacent to their neighbours, which increases the distance between the drops to the extent that gaps can appear, as shown in the optical image on the right, printed using $Ink_{Ag.ND}$. Some merging between drops in a single swathe can help to smooth this out, but - especially with smaller circles – this leads to poor shape fidelity and worsens the diagonal-neighbour problem.* ***(b)*** *Schematic showing the bitmaps required to print horizontal lines with vertical gaps between them. The gaps can only be an integer number of pixels wide, leading to little control over the spacing.* ***(c)*** *Illustration of how greater control can be achieved by using a smaller pixel size, combined with extra whitespace to counteract overfilling.*

Inkjet printing generally has an optimal range of jetting frequencies, f_n, dependent on the ink and the printhead, so to keep the number of drops ejected per second the same for OtG, the refined jetting frequency ($f_r = f_n \times F_r$) is needed. Thus, if an OtG pattern has the same number of swaths as a traditional design, the printing time is unaffected; print time is only expected to increase if the use of droplet positioning increases the number of printable swathes in a design. For some rectilinear designs (e.g. **Figure 6.1c**), the number of swathes is likely to be the same for OtG and traditional printing, but even something as simple as a circle is likely to require more swathes since drops no longer line up in the primary print direction. For example, a traditional annulus has four distinct columns with drops (**Figure 6.1a**) compared to seven distinct columns with OtG (**Figure 6.2b**). However, many printers support rotating the printhead to change the effective nozzle spacing perpendicular to the print direction, which can mitigate this issue, although it is less likely that all nozzles will align with a printable column in OtG.

If the additional print time is acceptable, the additional whitespace can also be used to better represent outlines and thin features (**Figure 6.2a**). Calculating optimal droplet positions is simple for well-defined geometry. For example, with a single-drop-wide circular outline of diameter d, the x- and y- coordinates of the i^{th} drop are:

$$x_i = d\cos(\theta_i)\,;\, y_i = d\sin(\theta_i), \text{ where } \theta_i = \frac{2\pi i}{\text{round}\left(\frac{d}{S_n}\right)} \tag{6.1}$$

To convert a spatial coordinate (x) to a pixel coordinate (p), which requires $p \in \mathbb{Z}^+$:

$$p_i = \text{round}\left(\frac{x_i - x_{min}}{S_r}\right) + 1 \tag{6.2}$$

where x_{min} is the smallest value of $x_i \; \forall \; i$ and the pixels are indexed from the bottom left starting at (p, q) = (1, 1). The same equation can be used to convert from spatial

coordinate y to pixel coordinate q. To make a filled circle, concentric circle outlines can be combined with d decreasing by $2S_n$ each time (a decrease of $2F_r$ in pixels), and rotating such that the first point is angled halfway between the first two points of the previous circle (**Figure 6.2b**).

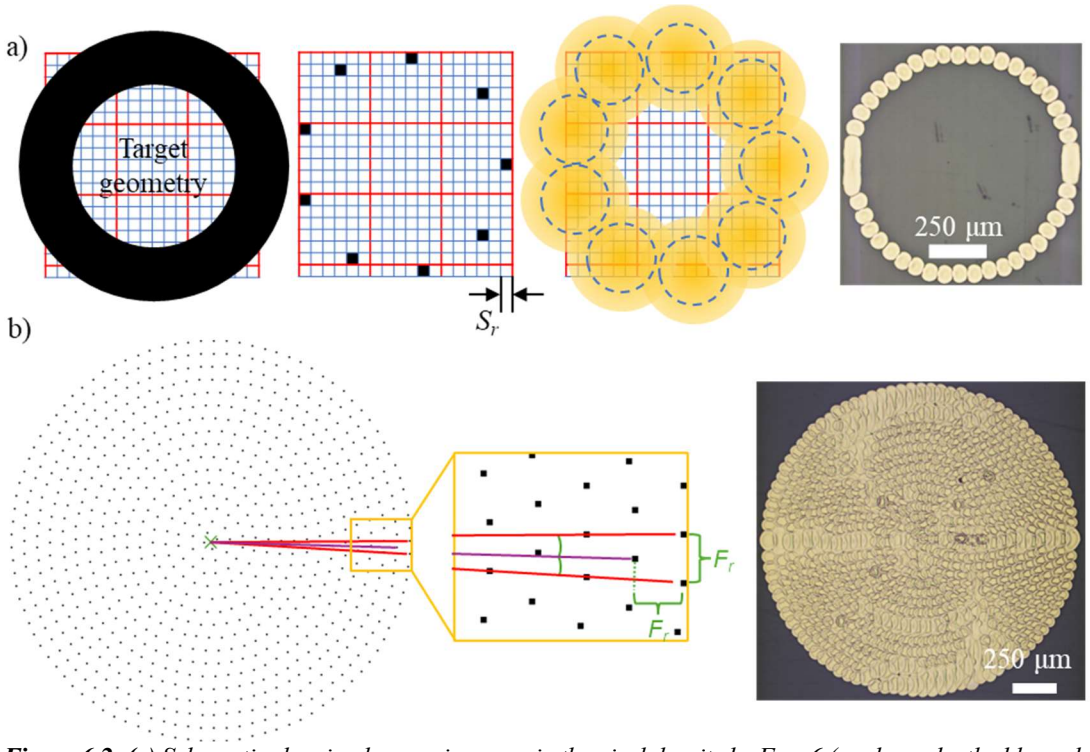

Figure 6.2: (a) *Schematic showing how an increase in the pixel density by F_r = 6 (as shown by the blue sub-grid, which has a size of S_r) removes the issues of rasterization when printing annuli, particularly the gaps that can occur due to diagonally neighbouring pixels. Overfilling is avoided by distributing black pixels around the diameter with sufficient whitespace. The optical image on the right shows the resulting print with $Ink_{Ag,ND}$.* ***(b)*** *Diagram for creating well-filled circles by creating concentric annuli (centred on the green ×), with an angular offset (demonstrated by the construction in the yellow inset) between neighbouring annuli to account for improved circle packing akin to 2D hexagonal close-pack patterns. The resulting prints with $Ink_{Ag,ND}$ are shown on the right.*

MATLAB software was produced to generate OtG bitmaps, for shapes including polygons, circles, electrocardiogram traces, and parametric curves. Closed shapes can be generated as single-drop outlines or filled with any 2D lattice of points (e.g. square or hexagonal lattices), hyper-uniform Poisson noise [309], or by spiralling in from the outline until completely filled. The code for this can be found in the Supplementary Information, and justifications for each type of filling are presented and discussed below.

However, calculations for intricate shapes can be complex, so a second method was developed to fit more closely with the existing workflow of users creating bitmaps in standard drawing software or converting slices of STL files into successive bitmaps for each layer. Therefore, the OtG software needed a method to convert such bitmaps to be OtG compatible. First, the user scales up the resolution of their existing bitmap by F_r, then uses the increased resolution to improve the design as desired (**Figure 6.3**). This higher-resolution input image is run through one of three algorithms to calculate which pixels should be "turned off" (i.e. set to white) to avoid the problems of overfilling, whilst keeping as close to the original geometry as possible.

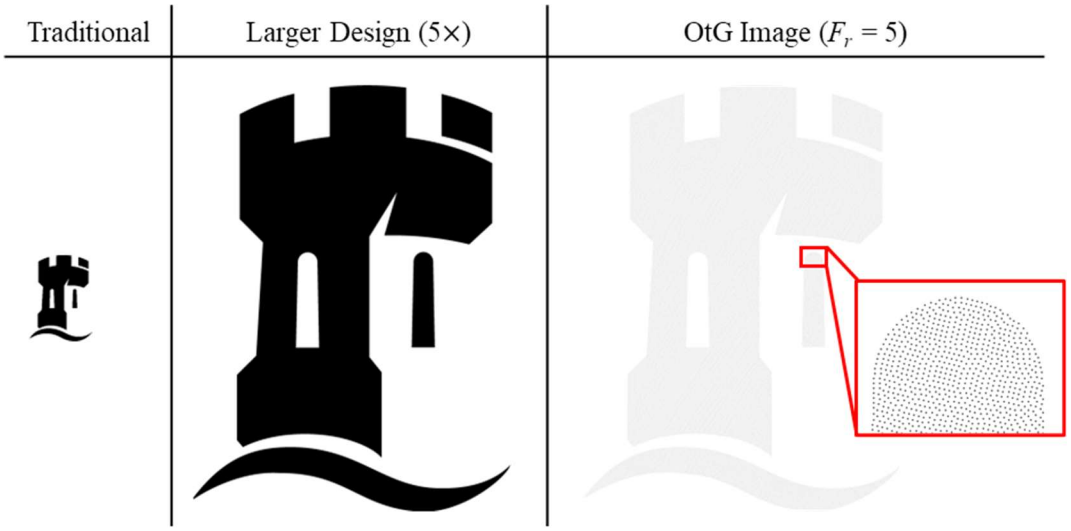

Figure 6.3: *Off the Grid (OtG) bitmap conversion demonstrated using the University of Nottingham castle logo and the window scan algorithm with F_r = 5 on a circular window. The traditional design is increased in size by a factor of F_r and improved by taking advantage of the higher resolution to make the input image for the OtG algorithm. The input image is then run through the chosen algorithm to create the required whitespace for the OtG image.*

Three algorithms were developed: window scan, edge scan, and mixed. The first two are described in more detail below, and mixed is the application of edge scan for a set number of iterations, before finishing with window scan.

6.2.1 Window Scan Algorithm

The window scan algorithm uses a window of pixels with side length F_r to determine where in the image a drop can fit, starting at the top-left and finishing at the bottom-

right. To approximate a circular drop, the pixels in the window are weighted according to how much of each pixel a circle with a diameter of F_r pixels (i.e. the largest circle that would fit in the window) would cover (**Figure 6.4a**). For designs with predominantly rectangular shapes, a window where all the values are 1, referred to as a square drop window, was found to be useful. At each step in the scan, the total window's value, V_{total}, is calculated as

$$V_{total} = \sum_{i=1}^{F_r^2} \frac{V_{image,\,i} + V_{window,\,i}}{F_r^2} \tag{6.3}$$

where $V_{image,i}$ is the value of the ith pixel from the image in the window's area (black = 0, white = 1) and $V_{window,i}$ is the value of the ith pixel of the window itself. If V_{total} is less than or equal to the threshold (a user-tuneable parameter between 1 and 2), then a black pixel is placed at the window's position in the output OtG image. The value of each of the window's pixels are also added to the corresponding pixels in the input image to avoid double-counting. The window then moves to the next position, and the process repeats over all possible window positions (**Figure 6.4b**).

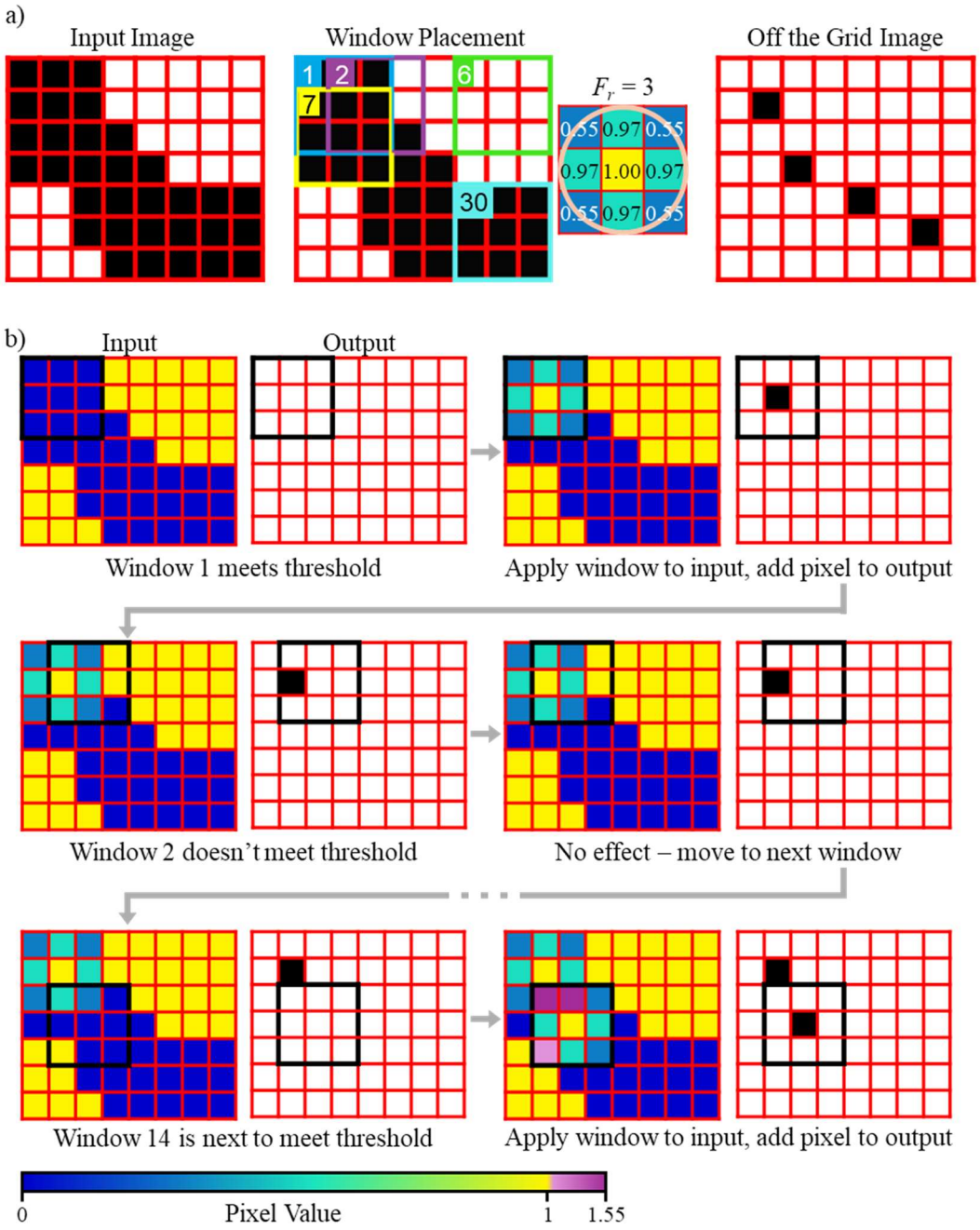

Figure 6.4: (a) *A diagram of the order in which windows will be considered for an 8x7 pixel input image, with the corresponding circular window for $F_r = 3$. The final output is displayed on the right.* ***(b)*** *A schematic for the first 14 iterations of the window scan algorithm, which starts with the window in the top left corner. This position meets the threshold as defined in* ***Eq. 6.3****, so a black pixel is added to the output image in the corresponding position, and the values of the drop window are added to the input image to avoid overlapping. Consequently, the next window position, one pixel to the right, doesn't meet the threshold, so no further action is taken. The window positions continue to be scanned through until one meets the threshold again at position 14, where the input and output are modified as necessary. This process is repeated until all window positions have been considered.*

This algorithm has many similarities to those used in error diffusion dithering [310], a process used to turn greyscale images into black-and-white whilst retaining the look of the image as closely as possible. The process is called error diffusion because local errors in the dithering are pushed away to be averaged out in other areas. By convention, they are pushed to the right and down, in a similar that the OtG window scan algorithm travels to the right and down. The primary difference between the two is that, in effect, the error to be diffused in the OtG algorithm cannot travel more than one window's size away from its point of origin, whereas there is no limit to how far it could travel in the dithering algorithms. This potentially mimics the effect of material being pinned, e.g. through evaporation, which is relevant for evaporative inks but may be less appropriate for inks which are pinned after the entire layer is printed, e.g. some UV curable inks. For both dithering and the OtG algorithms, this error diffusion has the effect that the bottom-right edges of features typically have more unwanted artefacts than the top-left edges. Since edge fidelity is often important in IJP of functional devices, the edge scan algorithm was developed to fix this issue.

6.2.2 Edge Scan Algorithm

The edge scan algorithm works similarly to the window scan algorithm, except the scan order is different. Here, the window is centred only on pixels at the edges of the design (i.e. where a black pixel is adjacent to a white pixel), going anticlockwise and starting with the top-leftmost black pixel. Once all of the edge pixels have been scanned over, a new set of edge pixels is calculated, taking into account pixels turned white during the scan and treating pixels previously considered as edge pixels as white so the algorithm gradually progresses towards the centre. These new edge pixels are scanned in the same way, until all black pixels have either been turned white or considered as edge pixels.

To keep the analogy with dithering algorithms, the error diffusion here effectively occurs from the edges of features inwards towards their centres. Therefore, it is expected that edge fidelity will be improved, but at the cost of less even coverage in the middle. This will likely be a more apparent problem for inks which are pinned quickly, but fluid flow from slowly pinned inks may counteract this issue.

6.2.3 Mixed Algorithm

The mixed algorithm first runs the edge scan algorithm for a user-chosen number of iterations, rather than running until the entire image has been converted. Any pixels which haven't been covered during this step are then processed using the window scan algorithm. The two steps are combined into the same OtG image. The result is a band of pixels around any edges in the design which have been placed using the edge scan algorithm, with the pixels which fill in the centre being placed with the window scan algorithm.

6.3 Algorithm Accuracy

To quantify how well the OtG image represents the desired geometry, a simplified simulation of the final print is run (**Figure 6.5**) which approximates how much coverage a pixel would have assuming a drop is centred on each black pixel of the OtG image. This is achieved by placing an appropriately sized drop window, at the coordinates of the black pixels in the OtG image (**Figure 6.5**). The coverage is compared to an image representing the idealised design, where a white or black pixel in the input image should have a coverage of zero or one, respectively.

The 3 categories of coverage error are: (i) having any amount of ink on white pixels (*over-white*), (ii) having too little ink on black pixels (*under-black*), and (iii) having too much ink on black pixels (*over-black*). To account for ink spreading and merging,

larger continuous areas of the same type of error are penalised more (e.g. a large gap where there should be ink counts as a larger error than several smaller, disconnected gaps with the same total area). The coverage error is the difference between the ideal and calculated coverage, and the types of coverage error can be weighted differently to help optimise the algorithm parameters for a given design. The final value is normalised by the total inked area of the design.

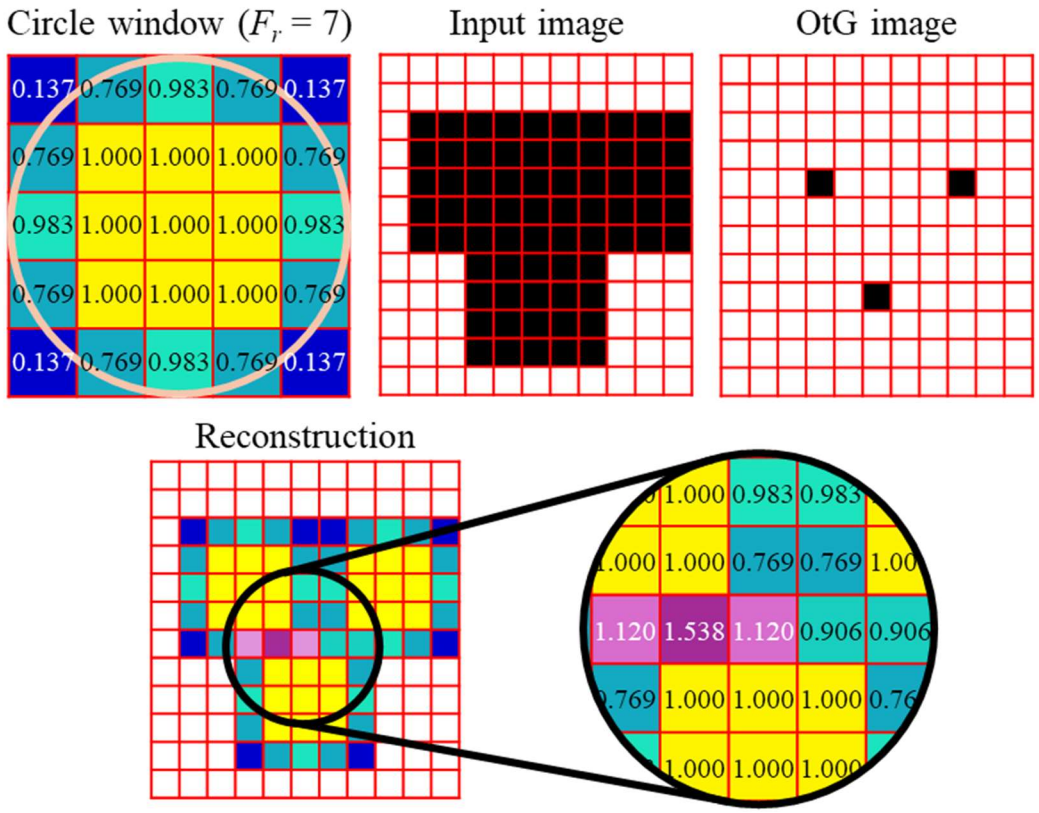

Figure 6.5: *A schematic to show the estimation of the quality of the OtG image conversion, calculated from the difference in ink coverage between the input image (i.e. where a black pixel should have a coverage of 1, and a white pixels a coverage of 0) and the reconstructed image based on the OtG image. The coverage error is the sum of these differences at each pixel, normalised by the total inked area of the design. The reconstruction is made by centring a window of appropriate size, in this case for a 7-pixel-wide circular drop, on each black pixel in the OtG image, and summing their contributions.*

Three bitmap images were used to test the optimal application of the different algorithms and their input parameters: a circle, an equilateral triangle, and a hall bar test design (**Figure 6.6a**). The three algorithms, as described above, are called window scan, edge scan, and mixed, and have input parameters of window shape, refinement, thresholds, and error weights. The values used are shown in **Table 6-1**. When

performing the error analysis, a target design image with a resolution of 1 μm per pixel was used, and the shape of the reconstruction window was the same as the shape of the window used during OtG conversion.

Each algorithm was applied to each test bitmap, and where ranges of parameter values are indicated every possible combination of parameters was tested (see Supplementary Information for the code). Further, each bitmap was produced at a high resolution (1 μm per pixel), so it could be scaled to test the effect of the overall size of a design on the efficacy of a given algorithm, always using S_n = 20 μm. The design size (**Table 6-1**) indirectly refers to the scale factor for resizing these images; at the largest design size, the circle has a diameter of 600 μm, the equilateral triangle has a side-length of 600 μm, and the Hall bar geometry (**Figure 6.6a**) is 1.5 mm wide.

Table 6-1: *An OtG image was generated for each test design for every combination of the parameters in this table. The design size refers to the circle's diameter and the triangle's side-length in microns and acts as a scale factor for the hall bar, which is 1.5 mm tall for the largest size. All ranges are closed intervals.*

Parameter	**Values**
Algorithm	Window scan, mixed, edge scan
Window shape	Square, Circular
Refinement	1-10, intervals of 1
Threshold	1-1.5, intervals of 0.05
Error weights	All 1
S_n	20 μm
Design size	400-600, intervals of 10

The lowest coverage error for each of the three designs was achieved with a mixed strategy (**Figure 6.6b**). Increasing refinement generally decreases the coverage error (**Figure 6.6c**), although certain values do not allow for drops to line up neatly with the design which leads to a higher error compared to the lower refinement (e.g. the hall bar with refinement of 3 averages an error of 0.12, compared to 0.09 with a refinement

of 2 because it is an even number of drops wide in most places). The same effect is true of the total size of the design for a given refinement (**Figure 6.6d**). Square drop windows appear to be better due to the decrease in the under-black error, but in reality the circular drops would spread out more than is accounted for in the model.

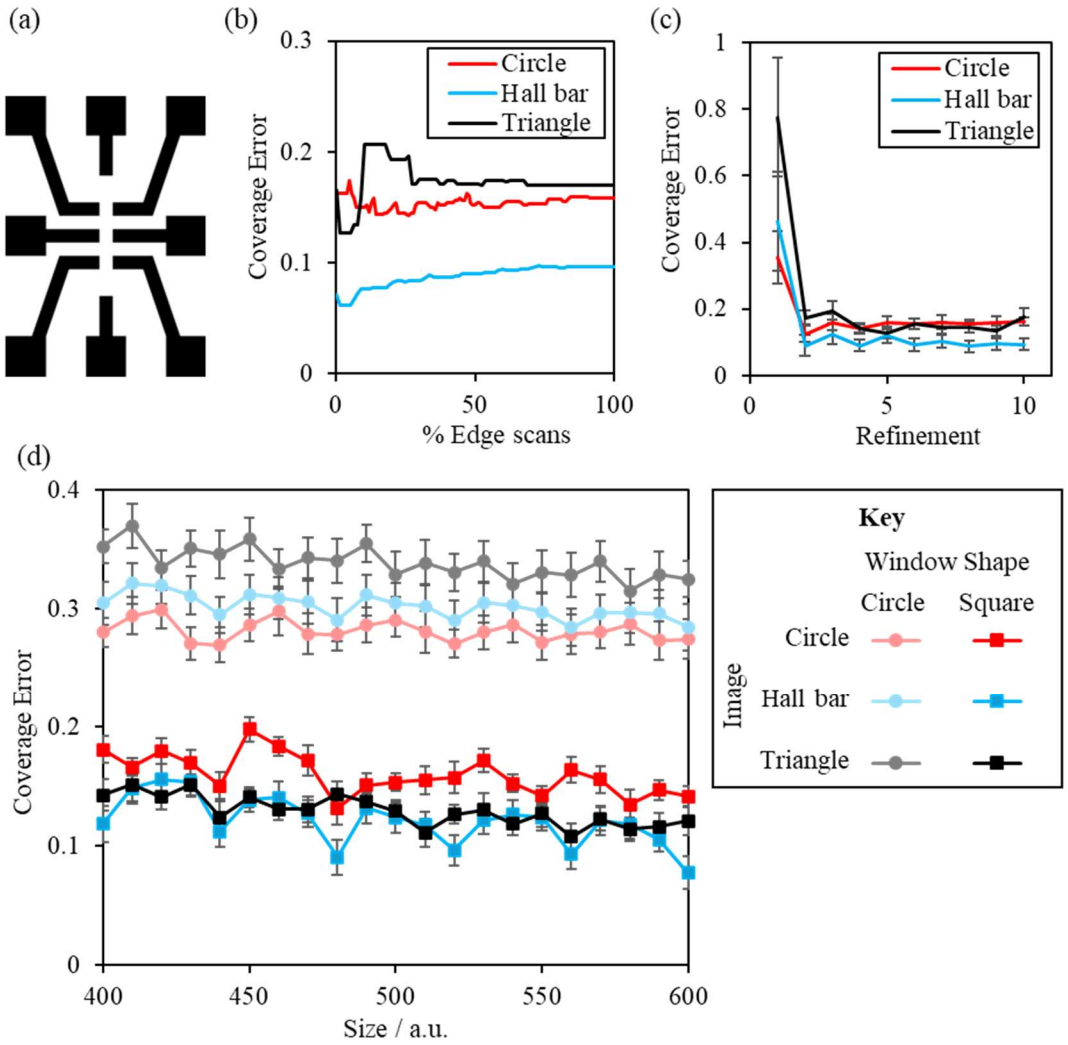

Figure 6.6: ***(a)*** *Bitmap of the hall bar design used for coverage error testing. Graphs of the coverage error for images of a circle, hall bar, and triangle varying with* ***(b)*** *percentage of edge scans used (0 = window scan algorithm, 100 = edge scan algorithm) for size = 500, refinement = 10, and threshold = 1,* ***(c)*** *refinement with threshold = 1 and square drop windows, and* ***(d)*** *size of the image, which is also split into square and circular drop shapes, with refinement = 5 and threshold = 1. Here, the error bars represent the standard deviation in the coverage error across all possible values for the percentage of edge scans used for each given data point. In (c) and (d) the lines are a guide for the eye.*

The threshold has the opposite effect (**Figure 6.7a**), since the increase in over-black errors outweighs the decrease under-black. However, this is due to the error weights all being identical – in the case where a broken circuit must be avoided, under-black

errors could be emphasised, which would lead to higher thresholds being optimal (**Figure 6.7b**). The threshold can therefore act to control the amount of material deposited within the geometry of the print, with the increase in coverage error for large continuous areas of the same category of error approximating the effect of flooding an area with too much material. This does not directly simulate the effect of material distribution on the surface topology, however a coverage error of zero would be achieved by perfectly even distribution of material, which is assumed in this model to be the most desirable state.

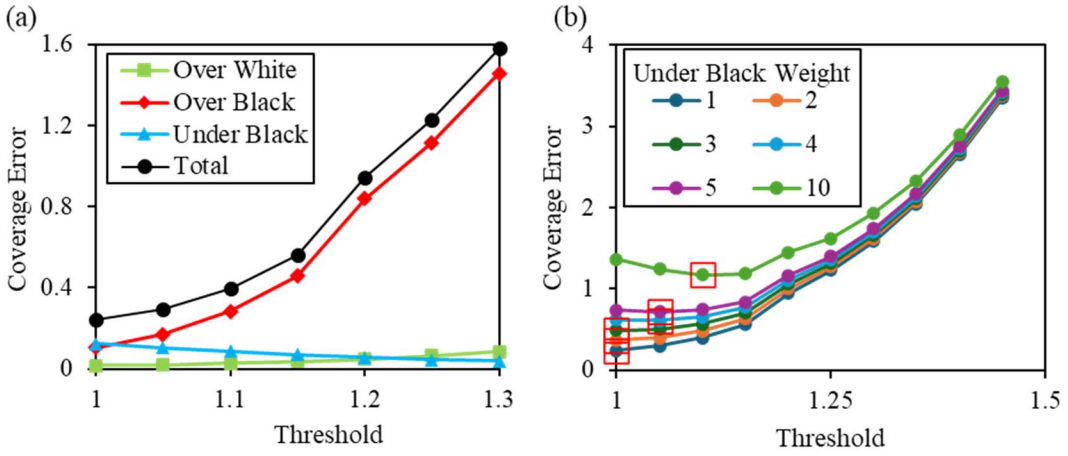

Figure 6.7: *Graphs showing* ***(a)*** *the effect of threshold on the different categories of coverage error, and* ***(b)*** *how varying the weight of under-black error (whilst keeping the other weights = 1), effects the optimal threshold value (as highlighted by the red box).*

6.4 Analysis of Printed Patterns using OtG

This section demonstrates successful inkjet deposition of structures designed with the OtG strategy. The majority of this work was done with $Ink_{Ag,ND}$ and $Ink_{Ag,XTPL}$ on PET to facilitate the image analysis, but OtG works with other materials, as shown at the end of the section.

A custom MATLAB script was developed to extract the centres and radii of the overlapping drops in microscope images of the prints. It uses MATLAB's built-in *imfindcircle* command, with the default arguments except for *RadiusRange=[25,40]*

and *EdgeThreshold=0*. The user could manually delete or add mis-identified or non-identified circles as well. The parameters were optimised to minimise the number of drops that weren't detected, without requiring too much manual deletion (**Figure 6.8**).

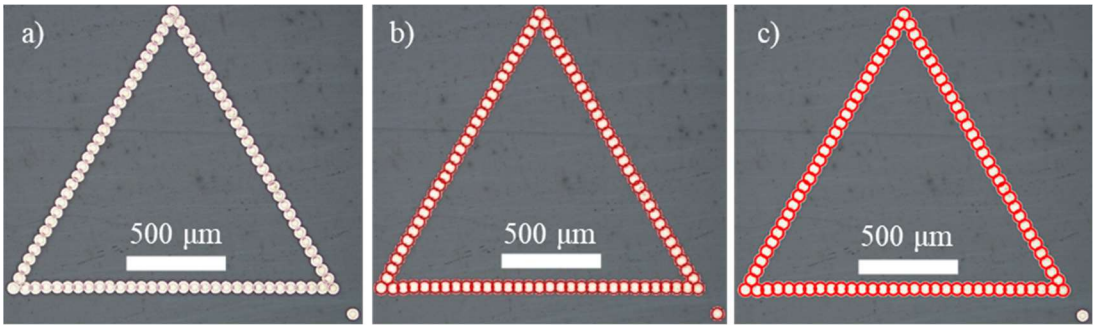

Figure 6.8: *Optical images with overlays from MATLAB showing the steps for detecting drops of* $Ink_{Ag,XTPL}$ *on PET.* ***(a)*** *A microscope image is taken with a known pixel size, then* ***(b)*** *all bright circles in the image are detected using MATLAB, before* ***(c)*** *erroneous circles (bottom-right corner) are removed manually by the user if necessary.*

6.4.1 Improving Shape Fidelity

OtG can greatly improve the accuracy of the outline of printed shapes, approaching the inherent limit due to the printer's motor- and timing accuracy. The aliasing effect of converting geometry to a bitmap is the major cause of shape fidelity error, and OtG can nearly remove it entirely. In triangles and circles, it was found that using the traditional printing strategy occasionally caused drops to merge, resulting in diameters up to ~70 µm, which also limits shape fidelity. In contrast, using OtG resulted in all drops drying individually with diameters of ~50 µm, as expected for individual droplets (**Figure 6.9a**).

The shape fidelity error is quantified by measuring the median distance, δ_{drop}, between the centres of the drops and straight lines or circles fitted to the droplet positions (**Figure 6.9b**), representative of the ideal design. The findings are presented in **Table 6-2** below.

Table 6-2: *OtG shape fidelity error (δ_{drop}) for the three shapes tested. Since δ_{drop} cannot be negative, the distribution is positively skewed, so values are quoted as the mean + difference to upper quartile/ – difference to lower quartile.*

	δ_{drop} / µm	
Shape (angle to printing direction)	**Traditional**	**Off the Grid**
Right-facing triangles (±60° and 90°)	14 +5/-4	0.8 +0.7/-0.4
Upwards triangles (±30°),	2 +2/-1	0.8 +0.7/-0.4
Circle	7 +9/-4	3 +2/-1

Significant enhancement is observed for all shapes deposited using the OtG strategy (**Figure 6.9c**), with δ_{drop} approaching the droplet-placement accuracy limit of the printer (δ_{drop} ~ 0.5 µm, measured for the square array of well-spaced drops). A refinement of $F_r = 8$ was chosen to optimise the hexagonal array positioning, since the perpendicular distance between rows of hexagonal close pack is, $\sqrt{3}/2$ and $8\times\sqrt{3}/2 = 6.93$ is the closest to an integer without producing bitmaps whose pixels are smaller than the precision of the LP50. This ensures the least rounding error when converting the positions to pixel coordinates, which are integers.

The measured δ_{drop} for all OtG lines is the sum of the printer and bitmap inaccuracies, whereas the measured traditional δ_{drop} is more complex. For lines at ±30°, the measured value is lower than expected from the bitmap inaccuracy (anticipated to match the ±60° lines), since adjacent drops on the same print swath merge, bringing their overall centre closer to the ideal position and creating a strongly bi-modal distribution of drop sizes. Thus, for all investigated shapes, the fidelity of the printed shape produced using the OtG strategy is improved by at least 5-fold compared to traditional printing. The only exception is where the shape required a

printed swath that allows for drop merging, which can improve the fidelity of the traditional strategy, but causes a bimodal drop-size distribution.

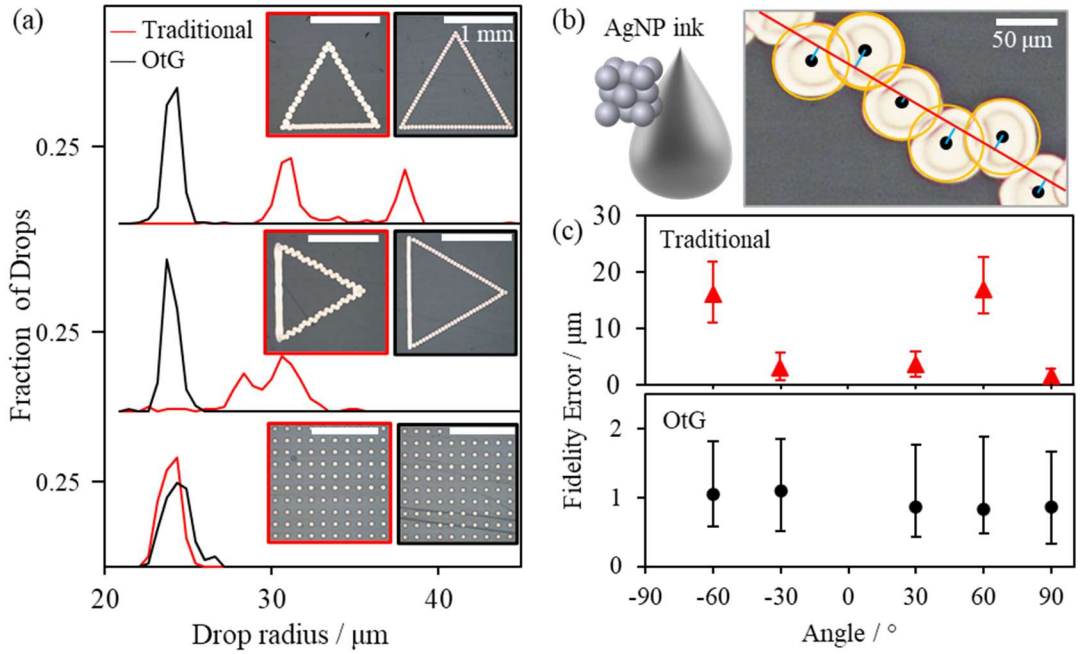

Figure 6.9: (a) *Distribution of drop radii extracted from optical microscopy images of shapes printed using traditional (red lines) and OtG (black lines) strategies, and (insets) corresponding optical images. All shapes were printed using $Ink_{Ag,ND}$. The baseline for the triangles is 31 drops long, and the nominal drop spacing chosen such that the angled lines are continuous. To eliminate gaps between the diagonal pixels in the traditional print, the size of the triangle had to be reduced. The scalebar is 1 mm.* ***(b)*** *Cartoon of a AgNP ink drop, and a representative optical image of a line of printed drops. The centres of the drops are fitted to a line. The upwards triangle has lines printed at ±30° and at 90° to the primary printing direction (vertical), and the rightwards triangle has lines printed at ±60° (the drops in the vertical line merge and so cannot be extracted).* ***(c)*** *Dependence of shape fidelity, defined as the median distance between the drop centre and the fitted line, on the angle of the print. The error bars represent the interquartile range.*

Whilst OtG enables high-fidelity single-drop paths, these designs are inherently vulnerable to breakages when a nozzle clogs or simply mis-fires. Therefore, it is advisable to print multiple layers with a nozzle step-over to reduce the likelihood of catastrophic breaks in continuity.

6.4.2 Alternative Shape-Filling Motifs

Surface finish and filling of shapes can also be controlled using OtG, aiming to reduce print-induced topology errors by unlocking alternative drop-packing motifs or offset layers. It is generally most desirable to have an even surface topology, i.e. a flat surface of even thickness throughout. This is quantified by the areal root mean square

deviation factor, *Sq*, which measures the root mean square deviation of the actual surface from a theoretical flat plane. This is a good one-number measurement of the flatness of a surface, although other application-specific can be used such as the existence of sharp protruding features (which can cause concentrations in electrical fields), or the spatial frequency of undulations in the surface (which can cause frequency-specific artefacts).

Triangles and circles were used again with traditional and OtG variations, the latter of which was split into ordered filling (hexagonal packing for triangles, concentric packing for circles) and Poisson-noise random filling [309], with both using the same outline and F_r as presented in **Chapter 6.4.1** (**Figure 6.10**). Offsets between layers were chosen such that they corresponded with drop positioning as far away as possible from the centres of drops on the previous layer (i.e. in the interstices of the previous layer), whilst retaining the motif of the fill type. Random filling simply used a different random generation for the offset layers. Further, hexagonal close pack has three distinct options, akin to the close-pack planes of a face-centred cubic crystal. Where necessary, hexagonal-filled prints are labelled using A for the first layer, then the following options for offset layers are distinguished as B and C.

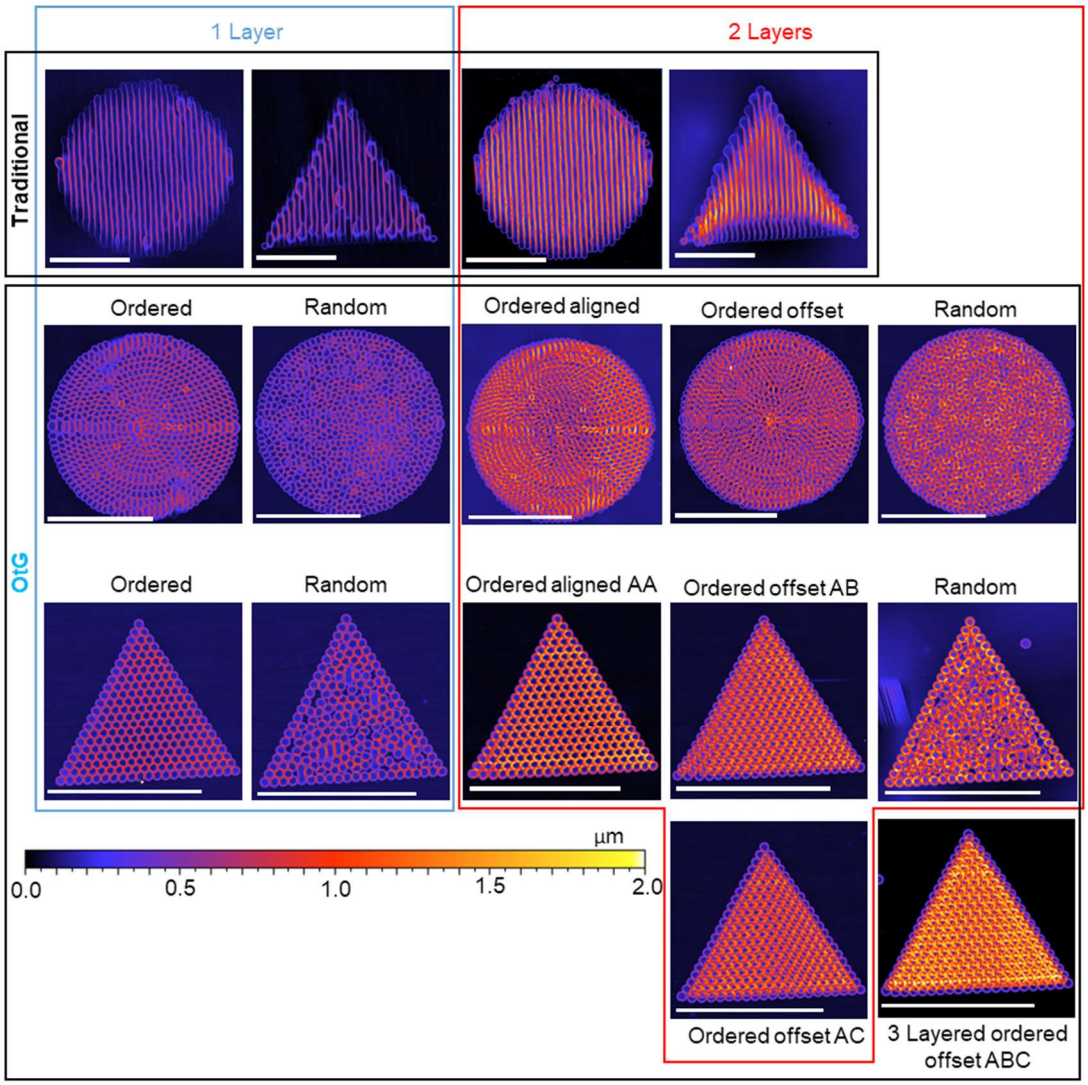

Figure 6.10: *Colour graded height maps of specimens printed using traditional and OtG designs and varying fill strategies. Specimens are grouped by pattern strategy and number of layers, with fill strategies annotated. Scale bar is 1 mm.*

Surface analysis by Coherence Scanning Interferometry (CSI) of the ordered OtG prints confirmed fully filled areas with uniform regular surface texture, with period corresponding to the drop diameter. In contrast, for traditionally printed shapes we observed overflow or under-filled spaces. For one printed layer (n_L =1), the areal root mean square deviation factor, *Sq*, was found to be comparable for all strategies, both for triangles and for circles, and is mostly defined by the coffee ring effect observed in AgNP inks (triangles: traditional *Sq* = 0.27 µm, ordered OtG *Sq* = 0.32 µm, random OtG *Sq* = 0.26 µm; circles: traditional *Sq* = 0.23 µm, ordered OtG *Sq* = 0.23 µm, random OtG *Sq* = 0.22 µm; **Figure 6.11**).

To investigate opportunities for control of surface texture with the OtG strategy, shapes were printed with drops in the second layer either aligned with the drops in the first layer or offset by S_n. Traditional and aligned $OtG_{ordered}$ shapes with n_L =2 displayed a ~2-fold increase in *Sq* (**Figure 6.11**, traditional *Sq* = 0.49 μm, aligned ordered OtG triangles *Sq* = 0.51 μm, aligned ordered OtG circles *Sq* = 0.34 μm). For offset OtG patterns, a small increase of roughness was observed for n_L = 1 and n_L =2 samples (**Figure 6.11**, offset $OtG_{ordered}$ triangles *Sq* = 0.36 μm, $OtG_{ordered}$ circles *Sq* = 0.30 μm,).

We envisage that the small increase of *Sq* in offset patterns is due to the ring-like height profile of individual drops resulting from the coffee-ring effect. For $Ink_{Ag,ND}$ the OtG strategy allows manipulation and enhancement of local geometry and shape filling, but no significant improvement in surface waviness. In contrast, for inks with weaker coffee-ring effects, the OtG technique (F_r = 2) can be used to reduce surface waviness (*Sa* reduced by 2.5×), as was previously demonstrated for PEDOT:PSS patterns [8].

For both one- and two-layer prints, the randomised fill did not fully cover the internal area of either the triangle or the circle. The likelihood of an uncovered patch will decrease as more random layers are printed, however this method seems unsuitable for only a few layers, unless the minimum allowed drop spacing is decreased to increase drop density. However, this would lead to overfilling of certain patches.

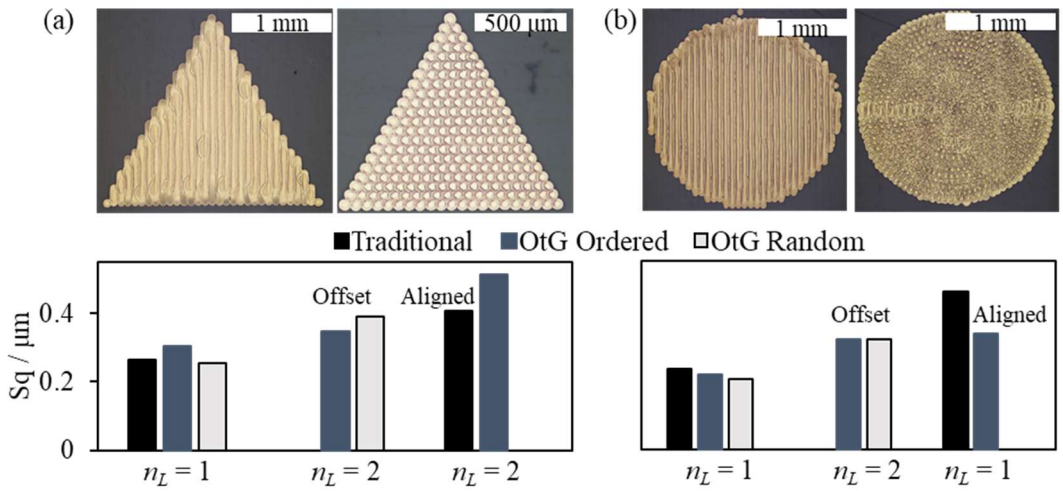

Figure 6.11: *Representative optical images and corresponding surface maps of shapes printed using $Ink_{Ag,ND}$, acquired using coherence scanning interferometry (CSI) for* ***(a)*** *equilateral triangles and* ***(b)*** *circles printed using traditional (left image of each pair) and OtG (right image of each pair) strategies. The bar charts show surface roughness estimated from CSI analysis of triangles and circles printed with different numbers of layers, n_L, using the traditional strategy, and an ordered or randomized OtG strategy. In the ordered OtG approach, the drops are placed in hexagonal close pack for the equilateral triangle, and in concentric rings order for the circle.*

6.4.3 Increasing Spatial Control

The sub-droplet resolution enabled by the OtG strategy can also be used to achieve increased control of the separation distance between printed features. We demonstrate that the smallest separation between printed silver lines with traditional deposition, $\Delta_{edge} = 40$ µm, can be improved significantly with the OtG strategy down to $\Delta_{edge} = 2.5$ µm, whilst also increasing the number of available increments in gap size by a factor equal to F_r (**Figure 6.12, Figure 6.13)**. For the LP50, $F_r = 10$ was chosen as the largest F_r studied in **Chapter 6.3**. In the Dimatix software, the smallest drop spacing is $S_r = 5$ µm, limiting F_r to a maximum of 6 to achieve the required $S_n = 30$ µm.

In the LP50, the printed horizontal silver lines where the on-centre gap between the drop at each end, Δ_{centre}, was 67 µm or less ($S_n = 60.5$ µm), the gap was closed, with an electrical resistance of 20 Ω, equal to that of a continuous line. For $\Delta_{centre} \geq 85$ µm ($\Delta_{edge} \geq 2.5$ µm), the resistance across the printed gap is over 10 MΩ (**Figure 6.12**), confirming effective material separation. A Δ_{centre} of 12 and 18 µm is transitional, producing variation between 3 replicates, with some closed gaps (electrical resistance,

R < 100 Ω) and some open gaps (R > 10 MΩ). This was also investigated for other combinations of line and gap orientation, with similar improvements attained by the OtG strategy (**Figure 6.13**), on both the LP50 and the Dimatix printers.

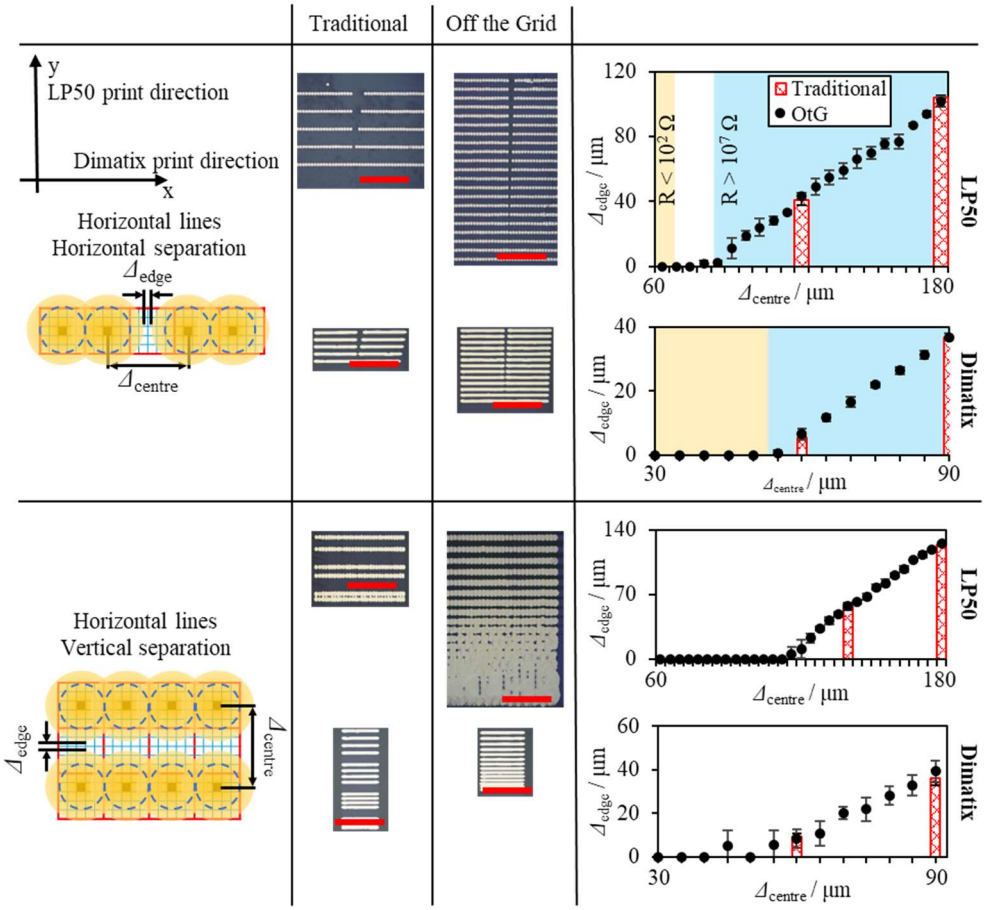

Figure 6.12: *Summary of the increased control over whitespace that OtG allows for horizontal lines. The schematics on the left define the measured separation (Δ_{edge}) and the on-centre line spacing (Δ_{centre}). Also shown are representative optical images of printed lines from traditional and OtG methods, from the LP50 ($Ink_{Ag,ND}$) and Dimatix ($Ink_{Ag,XTPL}$) printers. Shaded areas on the graphs represent the range of Δ_{edge} where electrical resistance measurements confirmed effective droplet separation for in-line gaps (blue, $R > 10^7$ Ω) and where low resistance was measured (yellow, $R < 10^2$ Ω) confirming overlapping droplets. The ideal drop spacing for the LP50 was S_n = 60.5 µm, and for the Dimatix was S_n = 30 µm. The scale bars in red are all 1 mm.*

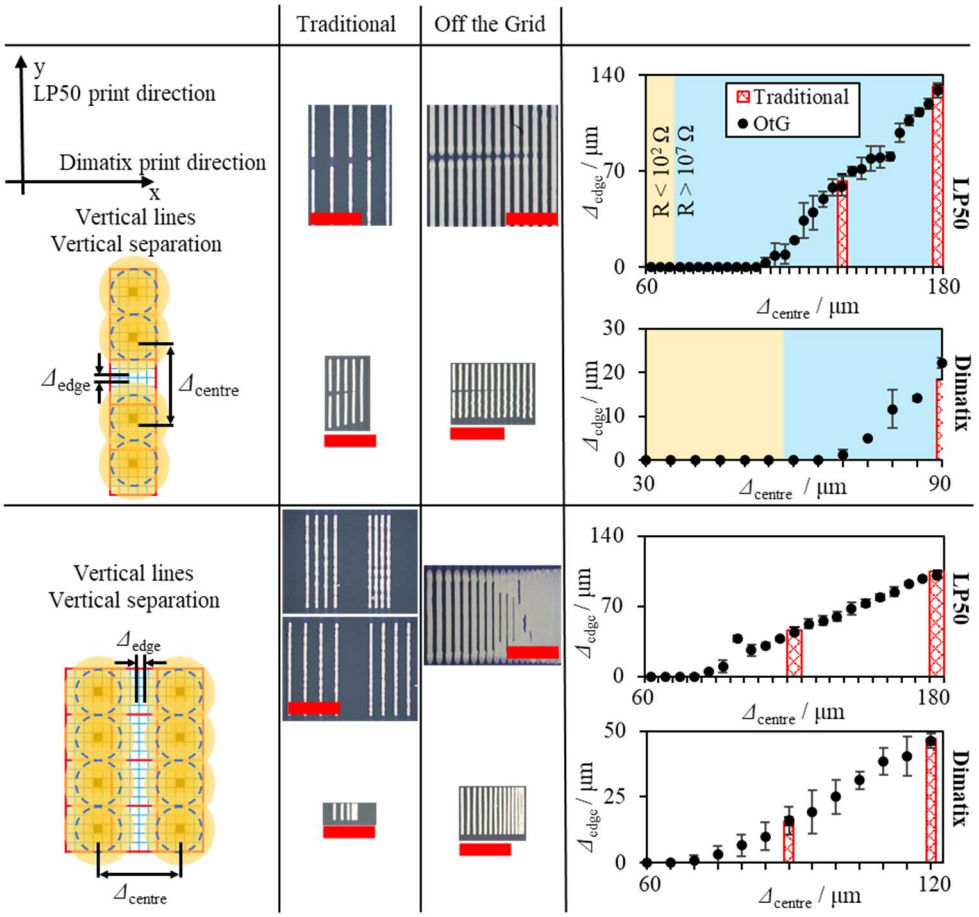

Figure 6.13: *Summary of the increased control over whitespace that OtG allows for vertical lines. The schematics on the left define the measured separation (Δ_{edge}) and the on-centre line spacing (Δ_{centre}). Also shown are representative optical images of printed lines from traditional and OtG methods, from the LP50 ($Ink_{Ag,ND}$) and Dimatix ($Ink_{Ag,XTPL}$) printers. Shaded areas on the graphs represent the range of Δ_{edge} where electrical resistance measurements confirmed effective droplet separation for in-line gaps (blue, $R > 10^7$ Ω) and where low resistance was measured (yellow, $R < 10^2$ Ω) confirming overlapping droplets. The ideal drop spacing for the LP50 was S_n = 60.5 µm, and for the Dimatix was S_n = 30 µm. The scale bars in red are all 1 mm.*

6.4.4 Off the Grid for Functional Designs

To demonstrate the practical potential of the OtG strategy, we produced high density patterns and intricate shapes. We selected a design for flexible electrocardiogram (ECG) pads and printed it on a flexible PET substrate, using traditional and OtG designs of single-pixel-wide traces. The ECG pad designs produced with the traditional printing strategy (**Figure 6.14a**, top), have several discontinuous areas and short circuit points are also observed, whereas the OtG patterns achieved a high-quality trace despite single droplet linewidth and high packing density. Whilst OtG enables the printing of such fine circuits, it is important to consider reliability if it is

to be adopted by industry. Therefore, circuit design should take into consideration the possibility of missed jets, by either thickening the trace width or employing multiple printed layers so that a random missed droplet will be filled in on subsequent layers. On the other hand, very narrow gaps (less than the diameter of the drops), are susceptible to short circuit if an errant drop lands in them, so larger gaps might be employed to improve reliability at the cost of taking up more space. Therefore, whilst OtG removes the constraint of pixellation, other design considerations still need to be taken into account and can restrict the potential geometry of the overall part.

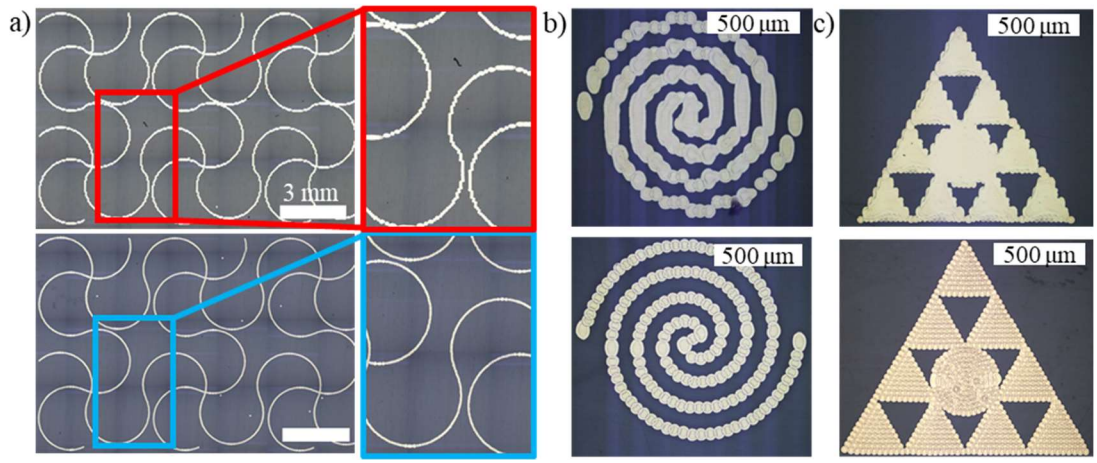

Figure 6.14: *Optical microscopy images of printed* ***(a)*** *electrocardiogram (ECG) pad traces,* ***(b)*** *an Archimedean spiral antenna, and* ***(c)*** *an X-band Sierpinski triangle antenna. In all cases, samples are printed with* $Ink_{Ag,ND}$ *using traditional (top) and OtG (bottom) strategies. The OtG triangular sections in (c) are printed with* S_n *= 60 µm, and the circular section with* S_n *= 53 µm.*

We further confirm the benefits of OtG with examples of a wideband Archimedean spiral antenna (**Figure 6.14b**) [311] and fractal antenna designed for C- and X-band applications (**Figure 6.14c**) [312]. For the Archimedean spiral, when using the traditional strategy there was no S_n that simultaneously prevented discontinuities without also over-filling and short-circuiting the inner portions of the pattern. In contrast, the OtG strategy achieved a high-quality print without discontinuities or over-filling, and a reduced variation in trace thickness necessary to antenna quality. Similarly, the OtG fractal antenna presents significant improvement over the traditional printing for achieving the desired geometry, increasing shape fidelity and

consistency of connections between antenna segments. Further, it was found that the triangles of the fractal antenna were ideally printed at S_n = 420 DPI (60.5 μm; F_r = 8, S_r = 3360 DPI, or 7.6 μm), whereas the central circle is ideally printed at S_n = 480 DPI (52.9 μm; F_r = 8, S_r = 3840 DPI, or 6.6 μm). Despite their dissimilar ideal droplet spacing, OtG allows these two components to be combined into a single bitmap and printed concurrently (**Figure 6.14c**). The OtG pattern of the circle was redrawn with F_r = 7 and replaced the circular section of the original F_r = 8 bitmap. With S_r = 3360 DPI, this resulted in the ideal S_n = 3360 / 7 = 480 DPI (52.9 μm) for the circle, without affecting the triangles. Thus, OtG enables designs to contain variable droplet spacing encoded into the bitmap, useful for local control of material distribution and coverage control. It is expected that this would translate to improved functionality, as has previously been shown for split-ring resonators (**Chapter 2.2.2.2**), but this was not explicitly tested.

The strategy reported here is transferable to different materials, from NP based inks to polymers, and across different material jetting platforms. Similar improvements in positioning accuracy were achieved using AgNP based inks printed with PiXDRO LP50 and Fujifilm Dimatix DMP-2800 printers. Improved curvature and pattern definition was achieved with the UV-curable polymers on LP50 e.g., $Ink_{Di,ND}$ (**Figure 6.15a**). The surface tension causes necking in the sharp point of the design when printed with the traditional strategy [237], which can be compensated for and removed with the OTG strategy.

The OtG strategy was also successfully used in the group for MetalJet printing (work performed by Dr N. Gilani). Densification of parts is a critical factor, where presence of pores between adjacent droplets affects mechanical properties of the printed structures and introduces strength-reducing defects. OtG has been used

successfully to replace the traditional square grid droplet spacing with hexagonal packing, as demonstrated for MetalJet Sn structures, resulting in improved part density and reduced porosity post-sintering (**Figure 6.15b**).

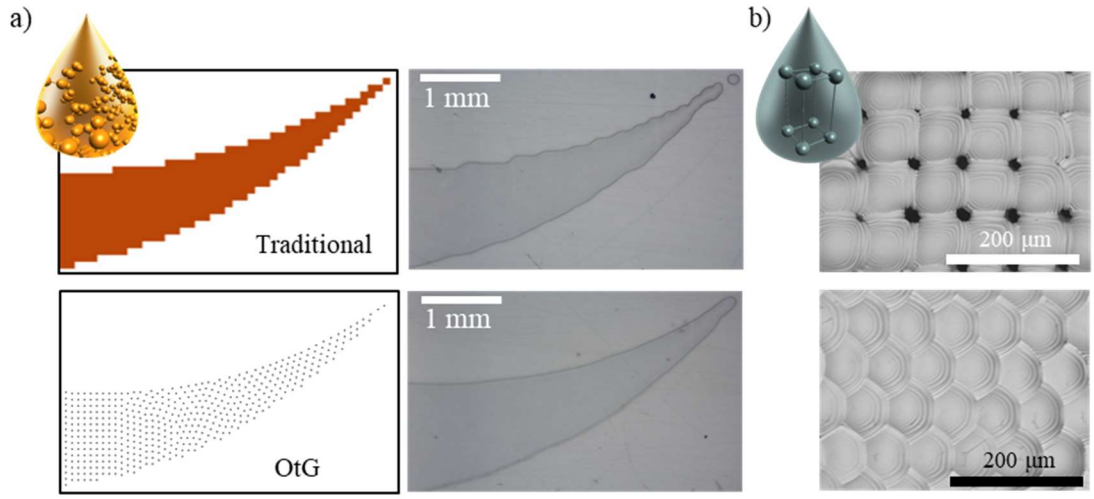

Figure 6.15: *Cartoon and optical images of* ***(a)*** *inkjet-printed* $Ink_{Di,ND}$ *and* ***(b)*** *Tin deposited using MetalJet with traditional (top) and OtG (bottom) strategies. The bitmaps in (a) are those used for the print.*

6.5 Summary

A novel printing methodology, Off the Grid, was developed to increase the precision and flexibility in placement of drops during inkjet printing. It is fully integrated with the bitmap-based representation used in most printers, so is compatible across multiple printing systems and with many different inks. A suite of MATLAB tools was developed to aid the creation of Off the Grid compatible bitmaps, including making well-defined geometries (e.g. circles, triangles, parametric lines etc.) from scratch and the ability to convert regular bitmaps.

The accuracy of these conversion algorithms was explored in detail, finding that the optimal approach is to follow the edges of a design first, before filling in the remaining centre. Further, the lowest threshold parameter is optimal when each category of coverage error is weighted equally, but higher thresholds are favoured if suppressing under-black errors is important.

When printing, the fluid dynamics of merging droplets complicates the analysis of shape fidelity, but it was found the Off the Grid can lead to a 5-fold improvement in the shape fidelity of circles and triangles, to the extent that further improvement is limited by the accuracy of the printer. Multiple shape filling patterns were demonstrated to fit well with the intended geometry (hexagonal fill for triangles, circling fill for circles) or break up repetitive roughness patterns using random noise (Poisson fill). However, the actual surface roughness wasn't improved when using silver nanoparticle inks due to the dominance of the coffee-ring effect. Control over whitespace was also shown to improve greatly, allowing for many more options when printing finely spaced detail.

The primary drawbacks come from the increased number of swathes which OtG requires, which thus increases the print time for all but the simplest rectilinear designs. To this end, it may be necessary to take a mixed approach, where certain areas of a design utilise OtG for its high fidelity (e.g. around the edges of a complicated shape), but where possible use the traditional approach for improved speed (e.g. to fill in the centre). Further, enabling the printing of single-drop-wide designs does not solve the issue of reliability inherent in such designs. If a nozzle gets blocked or mis-fires, it could cause a point of failure such as a break in a circuit. Therefore, these designs will require multiple layers to be printed with a nozzle stepover regardless of using a traditional or OtG approach.

Overall, the benefits of OtG came together to improve the functionality of ECG traces and two antenna designs, by eliminating short-circuits, improving shape fidelity, and allowing dynamic drop spacing withing a single image. OtG is inherently portable to commercial printers with no need for hardware upgrades, which greatly increases its scope for impact, particularly in applications where sharp features due to

aliasing can negatively affect performance. There is no equivalent technology which achieves similar improvements without requiring fully customised setups. Further, this study paves the way for inkjet printing to access uniquely complex 3D geometries, as shown in the next chapter.

7 3D STRUCTURES AND DEVICES

This chapter describes the printing of complex 3D structures from silver nanoparticle inks, including self-supporting overhangs and multimaterial designs. This work is based on single-drop-micropillars, which are created by pinning silver drops with high temperatures which force rapid evaporation of the carrier solvent. Small offsets for successive layers allow for overhanging designs including strut-based lattices and helices, useful for high surface area electrodes, reflect-arrays, or microwave-frequency metamaterials. Further, a dielectric was simultaneously printed to enable floating silver elements.

7.1 Introduction

Due to the liquid nature of the ink and thin layers, early inkjet printing research was focussed on 2D planar and heterostructure devices [263]. The first complex 3D shapes were for polymer prototyping, such as Stratasys Objet, but functional materials relied on flexible substrates, origami, or only partial use of inkjet printing to achieve taller structures [71,184]. More recently, research [40,41,138] and industrial [168] efforts have created conductive structures several millimetres tall. The results presented here adds to this work by producing complex structures in a more scalable way without requiring – but not excluding – a supportive matrix, using the novel Off the Grid strategy to enable higher-resolution designs than have been previously achievable.

7.2 Printing Vertical Micropillars

One of the simplest vertical structures is the single-drop micropillar, for example to be used as a narrow vertical interconnect in a PCB or to be printed in arrays. Heating the substrate ensures rapid evaporation of the ink solvent, preventing overflow. The maximum substrate temperature on the unmodified LP50 printer is T_{sub} = 70 °C, at

which $Ink_{Ag,XTPL}$ has a contact angle of 11° on PET and forms a disc with 90 µm diameter and a maximum thickness of 0.4 µm. As expected for a nanoparticle ink, there is a significant coffee ring effect. Identical drop diameters and coffee-ring effects were also formed on Kapton, glass (bare or coated with ITO or gold), PEN, aSi, and PTFE. As more drops are deposited on top of each other, the diameter gradually decreases (and thickness increases) with each layer up to $n_L = 10$, where it reaches an equilibrium diameter of 50 µm and an average thickness of 1.2 µm (**Figure 7.1a,b**). At this point the edge is ~2.5× taller than the centre, and there is no clear delineation between the layers when cross sectioned under SEM (**Figure 7.1c**). The positioning must be sufficiently precise that the drops do not form a collapsed pile, which was found to only be possible on the LP50 printer with Spectra SE-128 AA printheads.

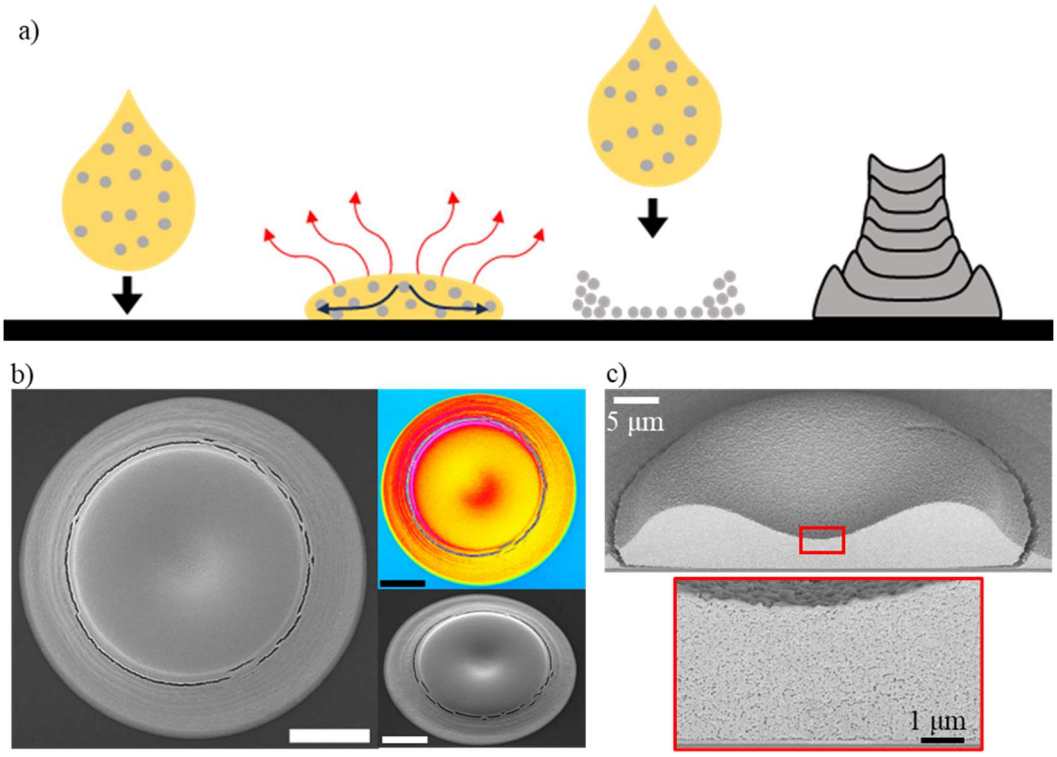

Figure 7.1: (a) *Schematic of AgNP (grey circles) ink deposition onto a heated substrate followed by solvent evaporation and drying. Internal flow drives the AgNPs towards the edge leading to a coffee ring shape, which acts as a template for consecutive droplets. SEM images of* ***(b)*** *an 11-layer micropillar, where the coffee ring effect is clearly present, including smaller insets which are false-colour (top) and tilted at 40° (bottom) to more clearly show the indent, and* ***(c)*** *a 10-layer micropillar cross-sectioned by FIB, including an inset to show the internal structure and the connectivity of the nanoparticles. The sample was not sintered.*

The pillars produced can terminate either with a hemispherical or ring-shaped tip, the latter being indicative of continued coffee ring effect, depending on the temperature of the tip. The pillars have low thermal conductivity prior to sintering [37,313], so cooling from the surrounding air and from evaporation of the ink solvent, combined with heating the base via the substrate, creates a thermal gradient in the pillar, with the base being hot and cooler towards the tip. Therefore, the drops forming the base of the pillar are in direct contact with the heated substrate, so are expected to have a higher evaporation rate compared to those forming the higher sections of the pillar. The formation of the coffee ring effect can be explained in the context of competing diffusion processes and depends on the timescale of evaporation compared to the timescale of the diffusion of nanoparticles within the given volume. This is ultimately determined by the substrate temperature, solvent composition, solid weight content and the solubility of the nanoparticles. If the nanoparticles are highly soluble, increasing the tip temperature favours coffee-ring formation, due to the increased speed of solvent flow during evaporation, which in turn transports nanoparticles to the edge faster [251]. Alternatively, if the nanoparticles are poorly soluble, a dome tip is favoured at higher temperatures, because the drop's surface descends more quickly than the nanoparticles can diffuse out to form a ring. This creates a quasi-solid layer where particle movement is interrupted, hence favouring domed morphologies [252].

To investigate which diffusion process dominates when printing with the AgNP inks, 5×5 pillar arrays were printed with T_{sub} = 50-70 °C and n_L = 10-50, so that lower T_{sub} and higher n_L (i.e. further from the heated substrate) will result in lower temperatures at the tip for the final layer. With structures printed using all three AgNP inks, a hotter tip was observed to favour the coffee-ring effect (**Figure 7.2**), which implies that the nanoparticles are soluble in the solvent [253]. Array size also has a

small impact, since larger arrays allow for more time for the pillar to thermally equilibrate with the heated substrate between instances of a new drop being deposited and cooling the tip through evaporation. Since all three AgNP inks have similar vertical electrical conductivity, it is expected that they have similar thermal conductivity [313] and therefore similar tip temperatures for a given T_{sub} and n_L. When T_{sub} = 50 °C, the evaporation rate is insufficient to form micropillars with n_L > 10, instead forming a puddle, particularly in the centre of the array, since the edges can draw heat from adjacent areas of the substrate, whereas the centre gets the most cooling from the evaporation of the of the ink's solvent.

For simple vertical interconnects in circuitry, the tip geometry is likely to have little impact on performance. However, for applications which require the control of electric fields, such as antennas or metamaterials, tend to avoid features with a high radius of curvature, as that can cause unwanted concentrations of the electric field. Therefore, a smoothly domed tip would be preferred. Alternatively, applications may be found for the ringed tip, such as filling them with a photo-active material to create a highly directional response.

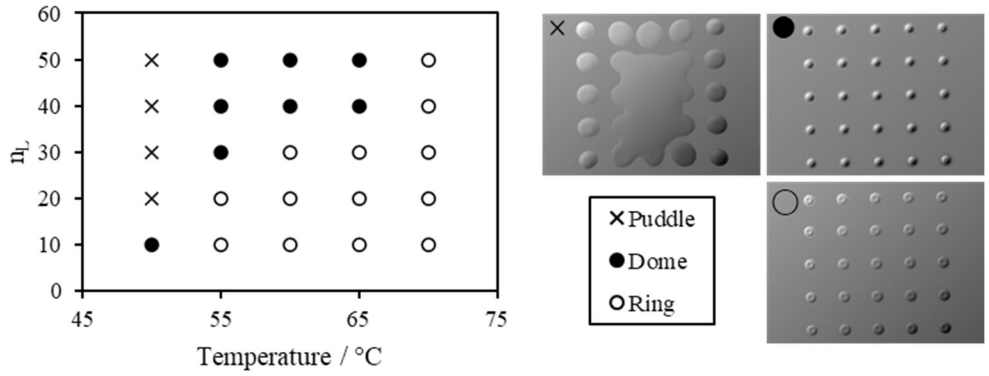

Figure 7.2: *The manner in which temperature and the number of layers (n_L) affect the pillar's tip morphology. Colder tips (i.e. with lower T_{sub} or larger numbers of layers) form domes, whereas hotter tips form the coffee ring. If T_{sub} is too low, the pillars cannot form at all, and collapse into a puddle. This is more pronounced in the centre since the edges of the array can be kept slightly hotter by heat conduction from elsewhere on the substrate. The SEM images are representative of the three morphologies: puddle (×, image shown is 40 layers at T_{sub} = 50 °C), domed (●, image shown is 40 layers at T_{sub} = 60 °C), and coffee ring (◯, image shown is 10 layers at T_{sub} = 65 °C)*

The micropillar structures with $n_L > 10$ are cylindrical with parallel sides and height ≤ 4 mm (**Figure 7.3a)**. After $n_L = 3500$ we observe some deviation in the positioning of the droplets, affecting the quality of the pillars, likely attributable to a small difference between the input and actual layer heights. When a large 5% overestimate in the layer height is used, a 1 mm pillar experiences sufficient inaccuracy that the top ~300 µm have drops landing on the sides rather than on top, effectively increasing its diameter up to 2× (**Figure 7.3b**). With optimised printing, high-quality micropillar arrays were successfully formed up to 39 × 39 pillars, as well as in a 2.5D photonic cavity design. This incorporates a point defect (i.e., a missing central pillar) where radiation with a frequency in the band gap of the pillar array structure would be trapped. The design shown, with 200 µm spacing (**Figure 7.3c**), would have a very narrow band gap at 18.2-18.7 THz. The designs can be produced over an area of at least 40 mm × 40 mm with pillar spacings as small as 100 µm, with larger arrays decreasing the number of defect states within the band gap, and smaller pillars increasing the frequency of the bandgap [181].

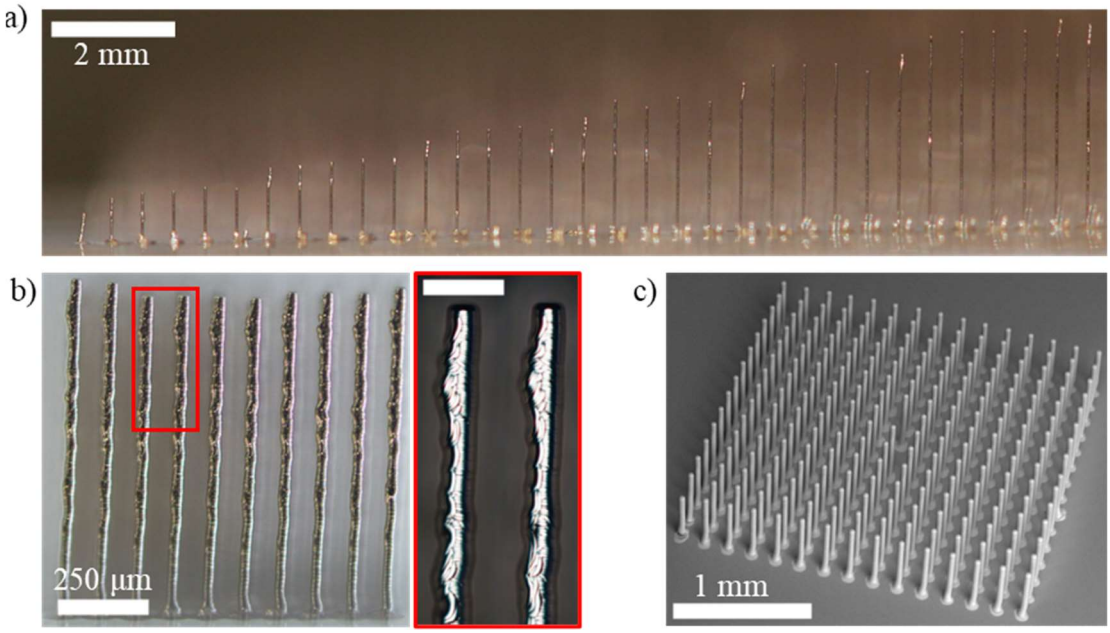

Figure 7.3: (a) *Optical images of printed pillars with a diameter of 50 µm and nL=500-4000. SEM image of a 15 x 15 pillar array with 500 layers forming the structure of a photonic cavity metamaterial by leaving out the centremost pillar.*

7.3 Freestanding Overhangs

To form free-standing, overhanging structures (**Figure 7.4**), drops in consecutive layers are deposited using the Off the Grid strategy [314] as well as an origin offset to achieve sub-droplet accuracy. A layer-by-layer offset of δ_{layer} = 2 µm is achievable with $Ink_{Ag,ND}$, although the failure rate for a 200 layer tilted micropillar is around 25%, whereas a maximum offset of δ_{layer} = 1 µm is stable with $Ink_{Ag,XTPL}$. However, due to the higher silver content of $Ink_{Ag,ND}$, the equilibrium layer height is 2.8 µm, so δ_{layer} = 1 µm is a less steep overhang (20° from the vertical for $Ink_{Ag,ND}$ compared to 40° for $Ink_{Ag,XTPL}$). It can also be seen that where a leaning pillar is printed on top of a vertical pillar, there is a curve instead of a sharp corner at the interface, implying that surface tension plays an important role in holding the ink in place until evaporation can pin it permanently. The diameter of the overhanging pillars is identical to that of the vertical pillars. However, the surface is extremely reflective, so optical microscope images are unable to clearly capture this due to the very high dynamic range between the central strip if the pillar, where light is directly reflected back to the camera, and edges of the pillar, where light is entirely reflected away due to the curvature.

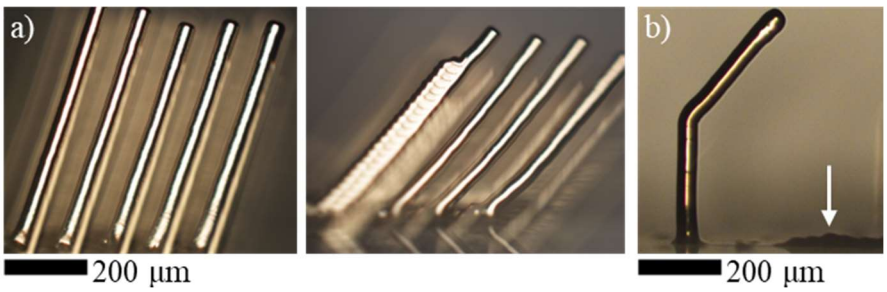

Figure 7.4: *Optical images of leaning micropillars using* ***(a)*** *$Ink_{Ag,ND}$ with a 1µm (left) and 2 µm (right) offset, and* ***(b)*** *$Ink_{Ag,XTPL}$, starting with a vertical pillar, then a 1 µm offset. The white arrow is pointing to a deposit formed from an attempted 2 µm overhang which was not able to form cohesively.*

More complex 3D structures were successfully created (**Figure 7.5a-f**). One 3D lattice was created with internal holes as small as 150 µm and highly repeatable

precision over a length of 8.75 mm, using an array of 8 × 35 pillars with a total of 1000 layers for a height of 1.15 mm and δ_{layer} = 1 μm (**Figure 7.5a-c**). The same number of layers was also used to produce a series of 10 tripods, with an isosceles-triangle base which was 500 μm wide and 700 μm tall (**Figure 7.5b, d**). Lattices were also inkjet printed with a unit cell of octahedrally arranged struts of potential interest for applications requiring high surface area, such as catalysis and battery electrodes. It was designed as a cuboid unit cell with X and Y side lengths of 500 μm, which required 707 layers for each strut to fully span the body diagonal with δ_{layer} = 1 μm and therefore would have a height of 848 μm. However, where the struts crossed in the centre of the unit cell created a hump, which appears to have caused subsequent drops to slide down before restarting the formation of the pillars at a lower height, so the final height of the printed structure is 777 μm (**Figure 7.5e-g**). To create lattices with pillars leaning in different directions, each direction of pillar is treated as a separate array. For example, a single layer of the octahedral lattice was printed in 4 separate parts, each a square array of drops with 500 μm spacing. The first array is printed with a 1 μm offset from the origin in the direction 45° clockwise from the Y axis. The following three are printed with an equal offset at angles of 135°, 225°, and 315°. The offset distance from the origin is increased by 1 μm per full layer. This approach is highly tailored to the specific geometry of the lattice, requiring a custom print script to be written each time. However, the principle can be extended to any geometry that can be sectioned into pillar-like structures.

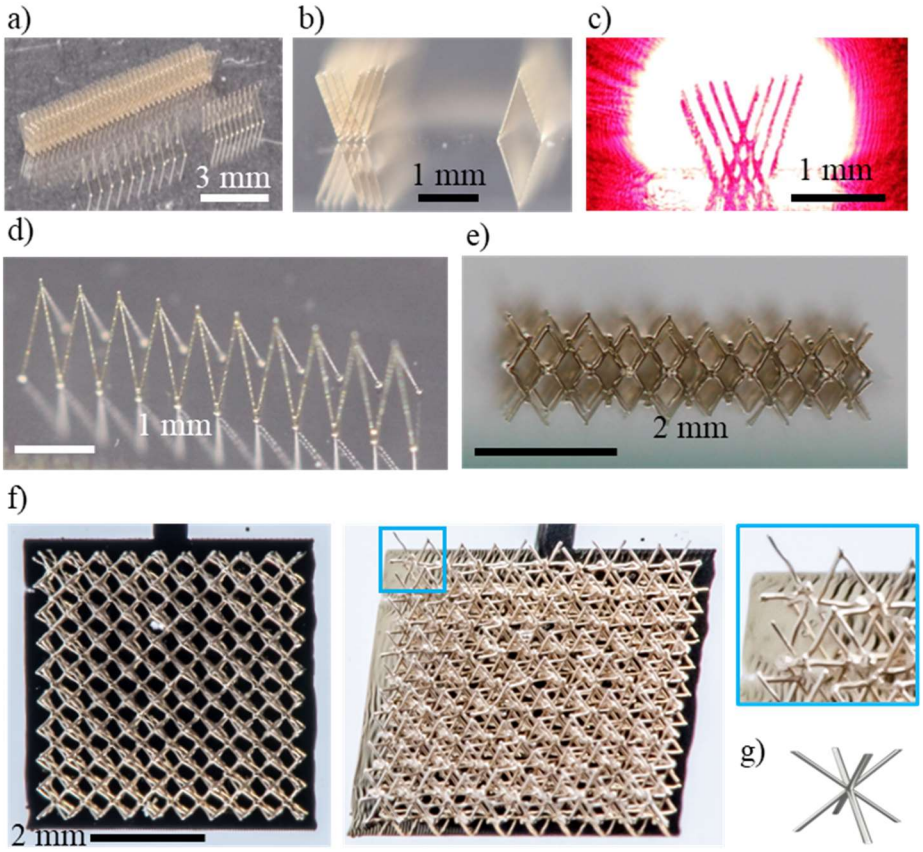

Figure 7.5: *Representative images of AgNP IJP structures formed from micropillars into* ***(a-d)*** *tripods and a length of 8 x 35 intersecting pillars spanning 8.75 mm, where the long, self-intersecting structure has been illuminated with a red laser beam along its length, and* ***(e,f)*** *an octahedral strut lattice printed on a single layer of inkjet-printed silver. A computer render of the unit cell of the lattice is shown in* ***(g)****.*

The direction of the offset can be altered during the printing process to create curved designs, without affecting the diameter of the pillar. An array of spiral micro-antennae designs was formed over an area of 3mm x 5mm and using 1000 layers of $\text{Ink}_{\text{Ag,ND}}$ on a copper substrate to ensure maximum heat conductivity. Using a radius of r = 250 µm, the x- and y-positions for a drop on the i^{th} layer (relative to the central axis) are $\Delta x_i = r\sin\big((i-1)\theta\big)$ and $\Delta y_i = r\cos\big((i-1)\theta\big)$, where θ is the subtended angle for δ_{layer} = 1 µm (**Figure 7.6a**). The tip is terminated with a ring, since the copper substrate has very high thermal conductivity, which enables higher heat flow into the silver, and the spirals are widely spaced (1 mm) which decreases the effect of neighbouring spirals cooling down the substrate by evaporation, both of which increases the tip temperature.

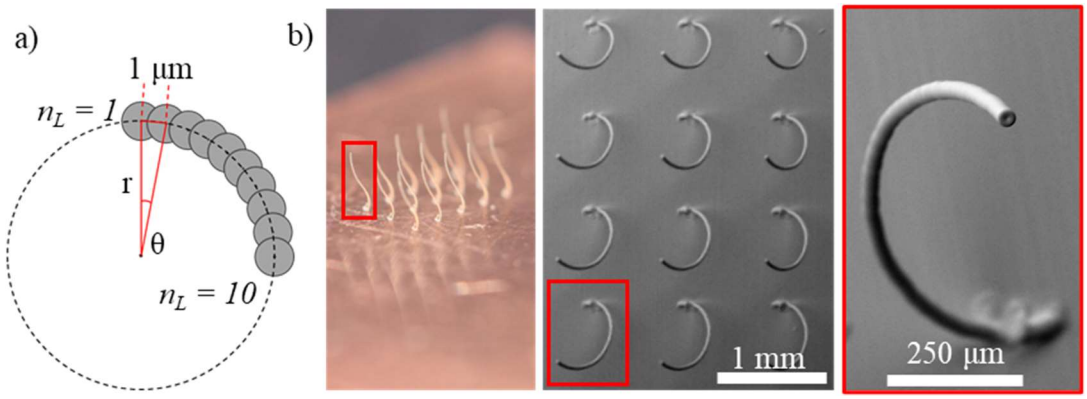

Figure 7.6: (a) *Schematic showing the construction of the first 10 layers of a helix with radius r and overlap between adjacent droplets of 1 µm. The angle subtended between the centres of two adjacent drops is θ, and the drops are not to scale here to aid clarity.* ***(b)*** *Optical and SEM images of an array of helices formed with r = 250 µm. The red square marks the same spiral shown from different perspectives.*

7.4 Printing Multimaterial Devices

Larger offsets than 1 µm between adjacent droplets in successive layers lead to the collapse of the pillars, necessitating a supportive matrix of some kind. Further geometries, such as those including floating elements or horizontal connections, are also impossible without support. The support material can also increase the dielectric contrast, which is vital for high functionality of metamaterials. In a photonic cavity, increasing the dielectric contrast increases the band gap of the pillar array, which allows for a wider range of frequencies that can be trapped, as well as helping to compensate for inaccuracies in the manufacturing process [181].

To utilise floating elements, Dr Tom Whittaker and Prof William Whittow (Wireless Communications Research Group, University of Loughborough) designed anisotropic metamaterials for use with signals around 10 GHz **(Figure 7.7a**). They consist of a 3D cross of silver, with different arm lengths of 1 mm, 0.75 mm, and 0.5 mm tip-to-tip. The cross section of each arm is square with a side length of 0.2 mm. Depending on the orientation of the crosses relative to the signal direction, the incoming wave experiences a different cross-sectional area of silver vs polymer, altering the overall relative permittivity. Most important is the length of the arm which

is parallel to the polarisation of the electric field. This initial design is meant as a proof of concept that the dielectric constant can be manipulated in this way, and so the chosen geometry does not require OtG or micropillar constructions to simplify the process.

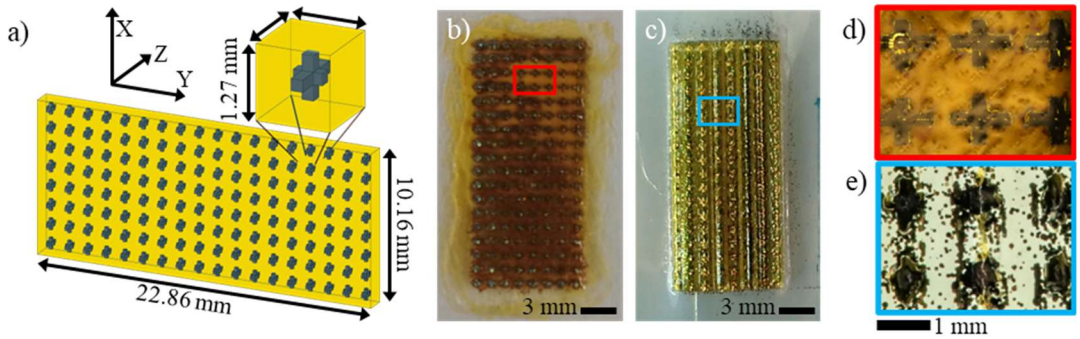

Figure 7.7: (a) *Diagram of the design for an anisotropic dielectric waveguide for operation around 10 GHz. The 3D crosses can be reoriented to alter the cross-sectional-area of silver (grey) vs dielectric (yellow) experienced by a wave travelling through the waveguide, depending on the direction of the wave. Optical images of the design are presented in* ***(b)*** *using* $Ink_{Ag,XTPL}$ *and* $Ink_{Di,TPGDA}$ *with Spectra SE-128 printheads, and* ***(c)*** *using* $Ink_{Ag,XTPL}$ *and* $Ink_{Di,EGDPEA}$ *with Xaar-128 printheads. Higher magnification images of the coloured insets are shown in* ***(d)*** *corresponding to image (b), and in* ***(e)*** *corresponding to image (c).*

The first print used the Spectra SE-128 AA printheads, due to their good accuracy when printing the $Ink_{Ag,XTPL}$. To allow for sufficient drying speed of the silver ink, whilst minimising the negative effect of heating on the polymer ink, T_{sub} = 70 °C was chosen. $Ink_{Di,TPGDA}$ was chosen because it is the most stable ink, although it has a relatively high loss tangent (**Chapter 5.2)**, and only 6 nozzles were sufficiently functional which increased the print time to a total of 5 days. Despite this, the polymer portion of the print was still of poor quality, likely due to changes in the $Ink_{Di,TPGDA}$ rheology as the head was held close to the heated substrate, although the silver printing was excellent **(Figure 7.7b, d**).

To improve the polymer quality, the Xaar-128 printheads were used, keeping the $Ink_{Ag,XTPL}$, but switching the polymer to $Ink_{Di,EGDPEA}$ for its improved dielectric properties. These printheads had >120 nozzles working, along with a larger drop volume, decreasing the print time to around 4 hours, and the heads themselves have a

much wider operational range of ink rheology. The increased rate of ink deposition required T_{sub} = 90 °C to sufficiently dry the silver ink, along with a 5 s wait between layers which likely also helped to keep the polymer ink cooler. The polymer print quality was very good, but the silver printing was poor (**Figure 7.7c, e**). This is likely due to the tendency of all of the AgNP inks to slightly wet the nozzle plate of the Xaar-128 printhead, which subsequently dries and interferes with proper jetting.

However, printing the samples in the Nano Dimension Dragonfly, using $Ink_{Ag,ND}$ and $Ink_{Di,ND}$ (printing performed by Mr Jacek Wojcik, Manufacturing Technology Centre, Coventry) was highly successful, forming clear interfaces between the materials with no satellite droplets and straight, orthogonal sides to the polymer matrix (**Figure 7.8a**). The silver arms are oriented in WG1 as X = 0.75 mm, Y = 1 mm, Z = 0.25 mm; in WG2 as X = 0.75 mm, Y = 0.25 mm, Z = 1 mm; and in WG3 as X = 0.25 mm, Y = 1 mm, Z = 0.75 mm, where the input signal is travelling in the Z-direction, with the electric field polarised in the X-direction This correlates well to the measurements and simulation of the relative dielectric constant (ε_r) of each waveguide-sized sample. Therefore, WG1 and WG2, which have the same arm length X = 0.75 mm, have very similar properties: for WG1 $\varepsilon_r = 3.45 \pm 0.02$, and for WG2 $\varepsilon_r = 3.41 \pm 0.02$. By contrast, WG3, with arm length X = 0.25 mm, has a significantly lower $\varepsilon_r = 3.11 \pm 0.02$. The measured values are close to the simulated values, with the exception of the very small separation in ε_r between WG1 and WG2, which were simulated to exhibit very similar properties. Furthermore, magnetic anisotropy was also observed due to the induced eddy current generated on the silver elements. The most likely cause of these small discrepancies is largely attributed to the anisotropic conductivity of the silver, since such anisotropy is not supported in the simulation software used.

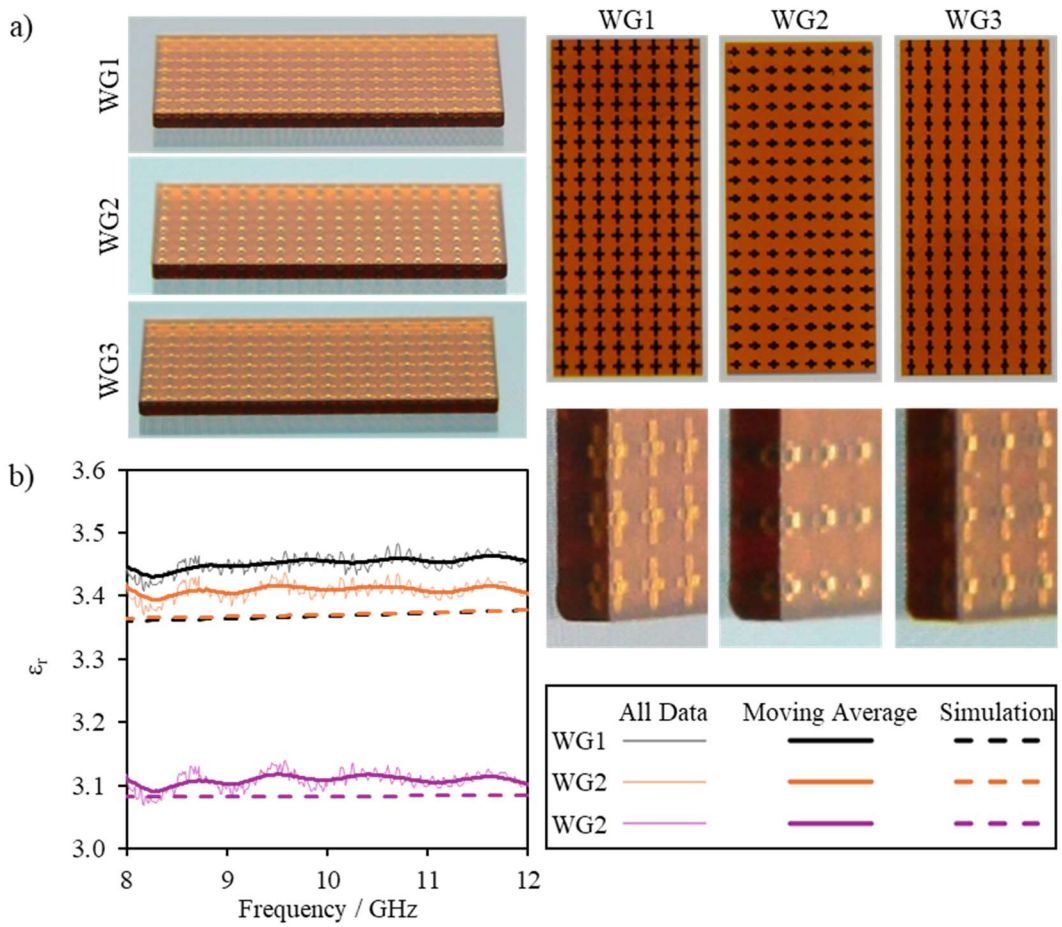

Figure 7.8: (a) *Optical images of three waveguide-sized samples (WG) printed on the Nano Dimension Dragonfly printer, from various angles. The silver arms are oriented in WG1 as X = 0.75 mm, Y = 1 mm, Z = 0.25 mm; in WG2 as X = 0.75 mm, Y = 0.25 mm, Z = 1 mm; and in WG3 as X = 0.25 mm, Y = 1 mm, Z = 0.75 mm.* ***(b)*** *The measured relative dielectric constant (ε_r) of each waveguide (solid lines) and the simulated values (dashed lines). The incoming signal travelled along the Z direction, with the electric field polarised in the X direction.*

This anisotropic dielectric is presented as a proof of concept that dielectric constant can be manipulated by altering the silver cross section experienced by a wave passing through. By utilising Off the Grid strategies, it should be possible to create devices whose properties vary at different points, such as graded dielectrics or complex waveguides. Further, use of the complex 3D structures demonstrated earlier in this chapter could unlock significantly more design freedom for these structures, if OtG can be successfully implemented into the Nano Dimension Dragonfly printer.

7.5 Summary

Micropillars were successfully printed from AgNPs by utilising a high substrate temperature $T_{sub} \geq 55$ °C to pin the silver. It was found that they reach an equilibrium diameter of 50 μm after 10 layers, which is independent of the substrate material. The pillars have straight, parallel sides, and can be terminated with a coffee ring or a dome shape – depending on the tip temperature – where higher temperatures favour coffee ring formation. They can be printed up to a height of 4 mm in large arrays, whose placing can be manipulated to mimic photonic crystal structures.

Further, these micropillars can tilt by up to 40° from the vertical whilst remaining unsupported, by applying a small lateral offset between subsequent layers of the pillars. Combining tilts in different directions allows for the construction of complex 3D shapes, including tripods, strut-based octahedral lattices, and helices, which could be utilised in a variety of applications including high-surface-area electrodes and reflectarrays.

Combining the silver with a polymer matrix increases the dielectric contrast and enables the construction of floating elements. The Nano Dimension Dragonfly printer was used to print anisotropic dielectrics for use at 8-12 GHz. The silver took the form of an array of anisotropic crosses with different arm lengths in each orthogonal direction. The length of the arm parallel to the polarisation of the electric field of an input signal had a large effect on the relative dielectric constant of the material as a whole: a decrease in length from 0.75 mm to 0.25 mm led to a 10% drop in the dielectric constant. Combined with the freedom of geometry allowed by inkjet printing, this opens the door to unique control over GHz communications within waveguides by freely altering the distribution and orientation of the silver inclusions.

8 DISCUSSION

The core aim of this PhD thesis was to enable inkjet printing of complex, 3D structures for use in electronics, antennas and metamaterials, with a view towards industrial adoption. This requires high resolution and electrical conductivity, as well as a method for printing more complex 3D geometries to be developed.

8.1 Material Optimisation

The first key research challenge was optimising the material properties of the print, particularly with reference to the electrical conductivity of printed silver. IJP printing is competitive with other AM process [134,135] in the horizontal plane, but its vertical conductivity is reported to be 3 orders of magnitude lower vertically [37]. In this work, optimised processing parameters led to over doubling of the horizontal conductivity (to $\sigma_{xy} = 2.9 \times 10^7$ S m^{-1}) compared with the literature values ($\sigma_{xy} = 8 \times 10^6$ S m^{-1}), and it was shown that the anisotropy was reduced to only 1 order of magnitude. However, it is unclear if this anisotropy reduction is due to the novel geometry presented in this work (i.e., a micropillar instead of a square block) or improved measurement technique (i.e., being able to account for probe contact resistance).

Further, several existing dielectric materials were investigated for use as a supporting matrix for floating silver elements, and print strategies were developed to reduce structural anisotropy in the print. It was found that Nano Dimension's proprietary ink and a mixture of EGDPEA and TCDMDA had the best combination of dielectric properties (ε_r = 2.76 for both), especially a low loss tangent ($\tan \delta_E = 0.013$ and 0.016 respectively), and resistance to the high temperatures to withstand the post processing requirements of the silver ink.

8.2 Unsupported 3D Structures

The second key research challenge came from the liquid nature of the ink. 3D geometries often require at least a small amount of overhang, which requires pinning the ink rapidly before it can run down the sides. This had been achieved with high substrate temperatures for vertical pillars >10 drops wide [41], as well as for single drop pillars which could even support some overhang using a highly customised system that only a single pillar at a time [40]. This work showed a novel use of the coffee ring effect, which is usually avoided in most inkjet printing circumstances, to create a template which restricted ink flow for long enough to evaporate the solvent. This growth mechanism was investigated in detail, showing how the equilibrium diameter of the micropillars was independent of the ink's solvent, and that the tip morphology (ringed or domed) depended on the temperature profile, with higher temperatures favouring ringed morphologies. This technique enables the printing of large arrays of pillars, with diameters of 50 μm and heights up 4 mm, with unsupported overhangs of up to 40°, which can be combined into helices and strut-based lattices, the latter of which are entirely novel within the IJP literature.

8.3 Printing Strategy for Enhanced Resolution

Many of the more complex geometries required a higher resolution than is traditionally available with IJP. Therefore, a novel method for processing the data fed to the printer was developed called Off the Grid. This also tackled the next key research challenge of enabling higher-accuracy reproductions of antenna- or metamaterial geometries. IJP traditionally utilises bitmap representation, in part due to its graphical printing origins, but also because it enables the very fast swathe-by-swathe approach with many nozzles (often 100s or 1000s), instead of the g-code approach of few (often 1) nozzles that process such as FDM use [1,2]. However, this results in significant

aliasing of otherwise smoothly curved or angled geometry, which is known to significantly reduce the performance of such devices [129,189].

The OtG strategy was shown to completely remove this aliasing effect, such that the error in droplet placement was entirely due to the motors and nozzle-timing inaccuracies, resulting in a 10-20× improvement depending on drop size and which printer was used. It can also be used to produce different filling motifs, which improves the surface morphology, especially with inks which don't pin too rapidly and allow some degree of fluid flow. These improvements were made using OtG algorithms akin to dithering algorithms, but there is still some error in the material coverage in the final print which needs improvement. Further, whilst visually improved prints of functional designs, such as antennas, were demonstrated, their functionality was no tested.

8.4 Multimaterial Printing

The final key research challenge addressed in this project was the production of multimaterial, 3D prints utilising a dielectric support matrix for the silver. Some simple examples have been shown in the literature before, but they were either non-functional designs, very simple geometries, or not simultaneous printing (i.e. the entire silver structure was printed first, followed by dielectric encapsulation) [41,315,316]. The Nano Dimension Dragonfly printer, however, has shown to be capable of excellent geometric freedom in this regard, and so a novel design for an anisotropic dielectric material was developed with the University of Loughborough. The initial proof-of-concept utilised floating 3D silver crosses with different arm lengths, whose orientation adjusted the relative dielectric constant between 3.11 and 3.45 at frequencies of 8-12 GHz. The printing was unsuccessful on the LP50 printer, dues to

poor jetting stability over very long print times, but the print quality on the Nano Dimension was excellent. The geometry used was designed to be highly flexible so that OtG could be applied and enable complex behaviour such as smoothly graded changes in the dielectric constant or the inclusion of waveguides. However, these designs were not produced due to time constraints.

The work presented here has demonstrated a new ability for inkjet printing to create fully 3D structures without requiring supporting material, by combining an optimised printing strategy with a novel method for improving drop placement resolution. Alongside a better understanding of the properties of conductive and dielectric inks, single material structures such as complex 3D lattices and helices were printed, and a multimaterial anisotropic dielectric was developed. Overall, this work has demonstrated that inkjet printing has the ability to print a wide variety of structures which could open the door to ever more customised and able electronic devices.

9 CONCLUSIONS AND FUTURE WORK

Many of the aims set out for this thesis have been met, but there is still significant work that could build on what has been presented. The first section of work on material optimisation identified $Ink_{Di,EGDPEA}$ and $Ink_{Di,ND}$ were as good support materials for their dielectric properties and compatibility with the silver's post-processing requirements. However, there is a wide array of other polymers which could be explored, rather than the fairly limited selection studied in this project.

Secondly, a reduction of the anisotropy in the silver's conductivity to 1 order of magnitude, a significant improvement over the literature. However, silver is not necessarily the ideal material for metamaterials – there are many other materials which may be less lossy in frequencies of interest that might also be able to support micropillar creation, so long as there is sufficient heat conductivity to keep the tip of the pillar hot.

On a more granular level, the problem of anisotropic conductivity is still far from solved. The organic ligand is so far necessary to the stability of the ink but is also the cause of the problem. Removing such molecules from the layer during the print is likely necessary, but burning it off with, for example, infrared radiation may make it impossible to co-print other, more delicate, materials such as a dielectric matrix. It is probable that a combination of novel nanoparticle-stabilising methods and processing conditions is required to solve this issue.

Next, a novel strategy to enhance printing resolution was developed. This successfully removed aliasing errors from the printing process whilst retaining compatibility with regular inkjet printers. However, the Off the Grid method is still relatively undeveloped as a potential tool for use by all users of inkjet printing. The

current version struggles with complex, narrow geometry, and so could benefit from existing algorithms such as those used to plot the paths for FDM heads or SLS lasers. It could also be extended to 3D to adjust droplet positioning to compensate for layers above and below. Ideally, it would also account for the spreading and solidifying behaviour of a specific ink. Currently, the algorithm assumes that the most even distribution of drops within the boundaries of the design is optimal, but this doesn't account for drop merging, contractions due to curing, print order, or printer accuracy. Ideally, there would be an iterative process where the drop placements are adjusted slightly to achieve the ideal layer topology and shape fidelity according to fluid simulation, to create the highest possible quality of inkjet printing.

The unsupported 3D structures made from single-drop-wide micropillars were highly successful, with heights up to 4 mm and overhangs up to 40° from the vertical. This work has only been done a single pillar at a time with highly customised setups, and not with the ability to produce extended lattices as shown in this thesis. However, there is a need to characterise the new structures and optimise the resulting performance. For example, the strut-based octahedral lattice is promising for high-surface-area electrodes, but the full advantages of such a geometry is still not explored. There are many lattice types, as well as the potential for interweaving electrically disconnected lattices, which could be investigated to maximise parameters such as power and energy density in supercapacitors.

Multimaterial structures were also produced, with an anisotropic dielectric that was best produced with the Nano Dimension Dragonfly printer. However, this design was limited to that printer's capabilities without further modifications. More complex designs would require integrating the advancements shown in this work with Off the Grid and micropillars into that high-performance printer and materials system.

Similarly to the unsupported structures, a full accounting anisotropic dielectric could be performed, utilising the Off the Grid strategy to enhance functionality. Small deviations from the theoretical geometry can create defect states in the band gap of these structures, which severely limits performance. A full study on the accuracy with which inkjet printing produces such lattices, and the consequent losses in the efficiency of the system, is needed.

Overall, the project was successful in pushing the boundaries of 3D inkjet printing for electronic materials, be it through enabling higher resolution or with truly 3D complex structures. Many novel geometries were presented, including a new approach to a spatially controllable, multimaterial anisotropic dielectric. The next stage of research will be to characterise the overall functional improvements that these printing strategies could create and create new devices to exploit those improvements.

10 REFERENCES

[1] Le HP. Progress and Trends in Ink-jet Printing Technology. Journal of Imaging Science and Technology 1998;42:49–62. https://doi.org/10.2352/J.ImagingSci.Technol.1998.42.1.art00007.

[2] Cummins G, Desmulliez MPY. Inkjet printing of conductive materials: a review. Circuit World 2012;38:193–213. https://doi.org/10.1108/03056121211280413.

[3] Bastola A, He Y, Im J, Rivers G, Wang F, Worsley R, et al. Formulation of functional materials for inkjet printing: a pathway towards fully 3D printed electronics. Materials Today Electronics 2023:100058. https://doi.org/10.1016/j.mtelec.2023.100058.

[4] Yuk H, Lu B, Lin S, Qu K, Xu J, Luo J, et al. 3D printing of conducting polymers. Nat Commun 2020;11:1604. https://doi.org/10.1038/s41467-020-15316-7.

[5] Bihar E, Corzo D, Hidalgo TC, Rosas-Villalva D, Salama KN, Inal S, et al. Fully Inkjet-Printed, Ultrathin and Conformable Organic Photovoltaics as Power Source Based on Cross-Linked PEDOT:PSS Electrodes. Adv Mater Technol 2020;5:2000226. https://doi.org/10.1002/admt.202000226.

[6] Weng B, Shepherd R, Chen J, Wallace GG. Gemini surfactant doped polypyrrole nanodispersions: An inkjet printable formulation. J Mater Chem 2011;21:1918–24. https://doi.org/10.1039/c0jm02595j.

[7] Brannelly NT, Killard AJ. A Printed and Microfabricated Sensor Device for the Sensitive Low Volume Measurement of Aqueous Ammonia. Electroanalysis 2017;29:162–71. https://doi.org/10.1002/elan.201600556.

[8] Rivers G, Austin JS, He Y, Thompson A, Gilani N, Roberts N, et al. Stable large area drop-on-demand deposition of a conductive polymer ink for 3D-printed electronics, enabled by bio-renewable co-solvents. Addit Manuf 2023;66:103452. https://doi.org/10.1016/J.ADDMA.2023.103452.

[9] Ahn BY, Walker SB, Slimmer SC, Russo A, Gupta A, Kranz S, et al. Planar and Three-Dimensional Printing of Conductive Inks. Journal of Visualized Experiments 2011. https://doi.org/10.3791/3189.

[10] Maattanen A, Ihalainen P, Pulkkinen P, Wang S, Tenhu H, Peltonen J. Inkjet-printed gold electrodes on paper: characterization and functionalization. ACS Appl Mater Interfaces 2012;4:955–64. https://doi.org/10.1021/am201609w.

[11] Rager MS, Aytug T, Veith GM, Joshi P. Low-Thermal-Budget Photonic Processing of Highly Conductive Cu Interconnects Based on CuO Nanoinks: Potential for Flexible Printed Electronics. ACS Appl Mater Interfaces 2016;8:2441–8. https://doi.org/10.1021/acsami.5b12156.

[12] Altay BN, Turkani VS, Pekarovicova A, Fleming PD, Atashbar MZ, Bolduc M, et al. One-step photonic curing of screen-printed conductive Ni flake electrodes for use in flexible electronics. Sci Rep 2021;11:3393. https://doi.org/10.1038/s41598-021-82961-3.

[13] Curtis CJ, Miedaner A, Van Hest MFAM, Ginley DS. Aluminum Films And Patterned Contacts Using Organometallic Precursor Inks. US-2010209594-A1, 2007.

[14] Qin Y, Alam AU, Howlader MMR, Hu NX, Deen MJ. Inkjet Printing of a Highly Loaded Palladium Ink for Integrated, Low-Cost pH Sensors. Adv Funct Mater 2016;26:4923–33. https://doi.org/10.1002/adfm.201600657.

[15] Lakhdar Y, Tuck C, Binner J, Terry A, Goodridge R. Additive manufacturing of advanced ceramic materials. Prog Mater Sci 2021;116:100736. https://doi.org/10.1016/j.pmatsci.2020.100736.

[16] Kholghi Eshkalak S, Chinnappan A, Jayathilaka WADM, Khatibzadeh M, Kowsari E, Ramakrishna S. A review on inkjet printing of CNT composites for smart applications. Appl Mater Today 2017;9:372–86. https://doi.org/10.1016/j.apmt.2017.09.003.

[17] Desai JA, Mazumder S, Hossain RF, Kaul AB. Inks of dielectric h-BN and semiconducting WS2 for capacitive structures with graphene. Journal of Vacuum Science & Technology B, Nanotechnology and Microelectronics: Materials, Processing, Measurement, and Phenomena 2020;38:52201. https://doi.org/10.1116/6.0000092.

[18] Brown E, Yan P, Tekik H, Elangovan A, Wang J, Lin D, et al. 3D printing of hybrid MoS2-graphene aerogels as highly porous electrode materials for sodium ion battery anodes. Mater Des 2019;170:107689. https://doi.org/10.1016/j.matdes.2019.107689.

[19] Worsley R, Pimpolari L, McManus D, Ge N, Ionescu R, Wittkopf JA, et al. All-2D Material Inkjet-Printed Capacitors: Toward Fully Printed Integrated Circuits. ACS Nano 2019;13:54–60. https://doi.org/10.1021/acsnano.8b06464.

[20] Chen Z, Li Z, Li J, Liu C, Lao C, Fu Y, et al. 3D printing of ceramics: A review. J Eur Ceram Soc 2019;39:661–87. https://doi.org/10.1016/j.jeurceramsoc.2018.11.013.

[21] Clark EA, Alexander MR, Irvine DJ, Roberts CJ, Wallace MJ, Yoo J, et al. Making tablets for delivery of poorly soluble drugs using photoinitiated 3D inkjet printing. Int J Pharm 2020;578. https://doi.org/10.1016/j.ijpharm.2019.118805.

[22] Kao H-LL, Cho C-LL, Chang L-CC, Chen C-BB, Chung W-HH, Tsai Y-CC. A fully inkjet-printed strain sensor based on carbon nanotubes. Coatings 2020;10:792. https://doi.org/10.3390/COATINGS10080792.

[23] Wang Y, Gong S, Wang SJ, Simon GP, Cheng W. Volume-invariant ionic liquid microbands as highly durable wearable biomedical sensors. Mater Horiz 2016;3:208–13. https://doi.org/10.1039/c5mh00284b.

[24] Tran VT, Wei Y, Du H. On-substrate joule effect heating by printed micro-heater for the preparation of ZnO semiconductor thin film. Micromachines (Basel) 2020;11:490. https://doi.org/10.3390/MI11050490.

[25] Cadilha Marques G, Tahoori M, Aghassi-Hagmann J, Sukuramsyah AM, Arnal Rus A, Bolat S, et al. Fabrication and Modeling of pn-Diodes Based on Inkjet Printed Oxide Semiconductors. IEEE Electron Device Letters 2020;41:187–90. https://doi.org/10.1109/LED.2019.2956346.

[26] Minemawari H, Yamada T, Matsui H, Tsutsumi JY, Haas S, Chiba R, et al. Inkjet printing of single-crystal films. Nature 2011;475:364–7. https://doi.org/10.1038/nature10313.

[27] Wang F, Gosling JH, Trindade GF, Rance GA, Makarovsky O, Cottam ND, et al. Inter-Flake Quantum Transport of Electrons and Holes in Inkjet-Printed Graphene Devices. Adv Funct Mater 2021;31:2007478. https://doi.org/10.1002/adfm.202007478.

[28] Yan H, Chen Z, Zheng Y, Newman C, Quinn JR, Dötz F, et al. A high-mobility electron-transporting polymer for printed transistors. Nature 2009;457:679–86. https://doi.org/10.1038/nature07727.

[29] Saleh E, Woolliams P, Clarke B, Gregory A, Greedy S, Smartt C, et al. 3D inkjet-printed UV-curable inks for multi-functional electromagnetic applications. Addit Manuf 2017;13:143–8. https://doi.org/10.1016/j.addma.2016.10.002.

[30] He Y, Foralosso R, Trindade GF, Ilchev A, Ruiz-Cantu L, Clark EA, et al. A Reactive Prodrug Ink Formulation Strategy for Inkjet 3D Printing of Controlled Release Dosage Forms and Implants. Adv Ther (Weinh) 2020;3:1900187. https://doi.org/10.1002/adtp.201900187.

[31] Nayak L, Mohanty S, Nayak SK, Ramadoss A. A review on inkjet printing of nanoparticle inks for flexible electronics. J Mater Chem C Mater 2019;7:8771–95. https://doi.org/10.1039/C9TC01630A.

[32] Derby B, Reis N. Inkjet Printing of Highly Loaded Particulate Suspensions. MRS Bull 2003;28:815–8. https://doi.org/10.1557/mrs2003.230.

[33] FAQ - Elephantech n.d. https://www.elephantech.co.jp/en/faq/ (accessed May 24, 2021).

[34] PV Nano Cell - Homepage n.d. https://www.pvnanocell.com/ (accessed May 24, 2021).

[35] Sv B, Printer PCB, Rivet PCB, Sv B, Printer PCB, Epoxy S. BotFactory SV2 PCB Printer 2018:2–4. https://www.botfactory.co/page/botfactory-sv2-pcb-printer (accessed May 24, 2021).

[36] Nano-Dimension. DragonFly LDM System 2020. https://www.nano-di.com/dragonfly-ldm-3d-printer (accessed May 24, 2021).

[37] Trindade GF, Wang F, Im J, He Y, Balogh A, Scurr D, et al. Residual polymer stabiliser causes anisotropic electrical conductivity during inkjet printing of metal nanoparticles. Commun Mater 2021;2:47. https://doi.org/10.1038/s43246-021-00151-0.

[38] Kirchebner B, Rehekampff C, Tröndle M, Lechner P, Volk W. Analysis of salts for use as support structure in metal material jetting. Production Engineering 2021;15:855–62. https://doi.org/10.1007/s11740-021-01055-1.

[39] He Y, Zhang F, Saleh E, Vaithilingam J, Aboulkhair N, Begines B, et al. A Tripropylene Glycol Diacrylate-based Polymeric Support Ink for Material Jetting. Addit Manuf 2017;16:153–61. https://doi.org/10.1016/j.addma.2017.06.001.

[40] Ko SH, Chung J, Hotz N, Nam KH, Grigoropoulos CP. Metal nanoparticle direct inkjet printing for low-temperature 3D micro metal structure fabrication. Journal of Micromechanics and Microengineering 2010;20:125010. https://doi.org/10.1088/0960-1317/20/12/125010.

[41] Sowade E, Polomoshnov M, Willert A, Baumann RR. Toward 3D-Printed Electronics: Inkjet-Printed Vertical Metal Wire Interconnects and Screen-Printed Batteries. Adv Eng Mater 2019;21:1900568. https://doi.org/10.1002/adem.201900568.

[42] British Standards Institution. BS EN ISO-ASTM 52950-2021 2021.

[43] Bourell DL. Perspectives on Additive Manufacturing. Annu Rev Mater Res 2016;46:1–18. https://doi.org/10.1146/annurev-matsci-070115-031606.

[44] Chatham CA, Long TE, Williams CB. A review of the process physics and material screening methods for polymer powder bed fusion additive manufacturing. Prog Polym Sci 2019;93:68–95. https://doi.org/10.1016/j.progpolymsci.2019.03.003.

[45] Dejene ND, Lemu HG. Current Status and Challenges of Powder Bed Fusion-Based Metal Additive Manufacturing: Literature Review. Metals (Basel) 2023;13:424. https://doi.org/10.3390/met13020424.

[46] Rafiee M, Farahani RD, Therriault D. Multi-Material 3D and 4D Printing: A Survey. Advanced Science 2020;7. https://doi.org/10.1002/advs.201902307.

[47] Seekaew Y, Lokavee S, Phokharatkul D, Wisitsoraat A, Kerdcharoen T, Wongchoosuk C. Low-cost and flexible printed graphene-PEDOT:PSS gas sensor for ammonia detection. Org Electron 2014;15:2971–81. https://doi.org/10.1016/j.orgel.2014.08.044.

[48] Sciacca G, Sinico M, Cogo G, Bigolaro D, Pepato A, Esposito J. Experimental and numerical characterization of pure copper heat sinks produced by laser

powder bed fusion. Mater Des 2022;214:110415. https://doi.org/10.1016/j.matdes.2022.110415.

[49] Bansal A, Panagamuwa CJ, Whittow WG. Full 360° beam steering millimetre-wave leaky-wave antennas coupled with bespoke 3D-printed dielectric lenses for 5G base stations. Electron Lett 2023;59. https://doi.org/10.1049/ell2.12775.

[50] Im J, Liu Y, Hu Q, Trindade GF, Parmenter C, Fay M, et al. Strategies for Integrating Metal Nanoparticles with Two-Photon Polymerization Process: Toward High Resolution Functional Additive Manufacturing. Adv Funct Mater 2023;33. https://doi.org/10.1002/adfm.202211920.

[51] Espera AH, Dizon JRC, Chen Q, Advincula RC. 3D-printing and advanced manufacturing for electronics. Progress in Additive Manufacturing 2019;4:245–67. https://doi.org/10.1007/s40964-019-00077-7.

[52] Perera ATK, Wu K, Wan WY, Song K, Meng X, Umezu S, et al. Modified polymer 3D printing enables the formation of functionalized micro-metallic architectures. Addit Manuf 2023;61:103317. https://doi.org/10.1016/j.addma.2022.103317.

[53] Borenstein A, Hanna O, Attias R, Luski S, Brousse T, Aurbach D. Carbon-based composite materials for supercapacitor electrodes: a review. J Mater Chem A Mater 2017;5:12653–72. https://doi.org/10.1039/c7ta00863e.

[54] Wang G, Zhang L, Zhang J. A review of electrode materials for electrochemical supercapacitors. Chem Soc Rev 2012;41:797–828. https://doi.org/10.1039/c1cs15060j.

[55] Hu J, Jiang Y, Cui S, Duan Y, Liu T, Guo H, et al. 3D-Printed Cathodes of LiMn1−xFexPO4 Nanocrystals Achieve Both Ultrahigh Rate and High Capacity for Advanced Lithium-Ion Battery. Adv Energy Mater 2016;6:1600856. https://doi.org/10.1002/aenm.201600856.

[56] O'Keefe S, Li Y, Luscombe CK. Solution processed low-k dielectric core-shell nanoparticles for additive manufacturing of microwave devices. J Appl Polym Sci 2017;134. https://doi.org/10.1002/app.45335.

[57] Li W-D, Wang C, Jiang Z-H, Chen L-J, Wei Y-H, Zhang L-Y, et al. Stereolithography based additive manufacturing of high-k polymer matrix composites facilitated by thermal plasma processed barium titanate microspheres. Mater Des 2020;192:108733. https://doi.org/10.1016/j.matdes.2020.108733.

[58] Khosravani MR, Reinicke T. 3D-printed sensors: Current progress and future challenges. Sens Actuators A Phys 2020;305:111916. https://doi.org/10.1016/j.sna.2020.111916.

[59] Wang X, Zhang M, Zhang L, Xu J, Xiao X, Zhang X. Inkjet-printed flexible sensors: From function materials, manufacture process, and applications perspective. Mater Today Commun 2022;31:103263. https://doi.org/10.1016/J.MTCOMM.2022.103263.

[60] Kang T-KK. Inkjet printing of highly sensitive, transparent, flexible linear piezoresistive strain sensors. Coatings 2021;11:1–8. https://doi.org/10.3390/coatings11010051.

[61] Zheng Z, Kim N, Wong WS, Yeow JTW. Inkjet-printed CMUT humidity sensors with high sensitivity and low hysteresis. Sens Actuators B Chem 2021;327:128920. https://doi.org/10.1016/j.snb.2020.128920.

[62] Wang H-C, Hong Y, Chen Z, Lao C, Lu Y, Yang Z, et al. ZnO UV Photodetectors Modified by Ag Nanoparticles Using All-Inkjet-Printing. Nanoscale Res Lett 2020;15:176. https://doi.org/10.1186/s11671-020-03405-x.

[63] Sliz R, Lejay M, Fan JZ, Choi M-J, Kinge S, Hoogland S, et al. Stable Colloidal Quantum Dot Inks Enable Inkjet-Printed High-Sensitivity Infrared Photodetectors. ACS Nano 2019;13:11988–95. https://doi.org/10.1021/acsnano.9b06125.

[64] Austin JS, Xiao W, Wang F, Cottam ND, Rivers G, Ward EB, et al. Developing colloidal nanoparticles for inkjet printing of devices with optical properties tuneable from the UV to the NIR. J Mater Chem C Mater 2024;12:10992–1000. https://doi.org/10.1039/D4TC01917B.

[65] Chu S, Chen W, Fang Z, Xiao X, Liu Y, Chen J, et al. Large-area and efficient perovskite light-emitting diodes via low-temperature blade-coating. Nat Commun 2021;12:147. https://doi.org/10.1038/s41467-020-20433-4.

[66] Ho SJ, Hsu HC, Yeh CW, Chen HS. Inkjet-Printed Salt-Encapsulated Quantum Dot Film for UV-Based RGB Color-Converted Micro-Light Emitting Diode Displays. ACS Appl Mater Interfaces 2020;12:33346–51. https://doi.org/10.1021/acsami.0c05646.

[67] Hermerschmidt F, Mathies F, Schröder VRF, Rehermann C, Morales NZ, Unger EL, et al. Finally, inkjet-printed metal halide perovskite LEDs-utilizing

seed crystal templating of salty PEDOT:PSS. Mater Horiz 2020;7:1773–81. https://doi.org/10.1039/d0mh00512f.

[68] Alex-Amor A, Palomares-Caballero Á, Moreno-Núñez J, Tamayo-Domínguez A, García-García C, Fernández-González JM. Ultrawideband inkjet-printed monopole antennas for energy harvesting application. Microw Opt Technol Lett 2021;63:1719–26. https://doi.org/10.1002/mop.32803.

[69] Farooqui MF, Shamim A. 3-D Inkjet-Printed Helical Antenna with Integrated Lens. IEEE Antennas Wirel Propag Lett 2017;16:800–3. https://doi.org/10.1109/LAWP.2016.2604497.

[70] Helena D, Ramos A, Varum T, Matos JN. Antenna Design Using Modern Additive Manufacturing Technology: A Review. IEEE Access 2020;8:177064–83. https://doi.org/10.1109/ACCESS.2020.3027383.

[71] Kimionis J, Isakov M, Koh BS, Georgiadis A, Tentzeris MM. 3D-Printed Origami Packaging with Inkjet-Printed Antennas for RF Harvesting Sensors. IEEE Trans Microw Theory Tech 2015;63:4521–32. https://doi.org/10.1109/TMTT.2015.2494580.

[72] Jung S, Sou A, Banger K, Ko DH, Chow PCY, McNeill CR, et al. All-inkjet-printed, all-air-processed solar cells. Adv Energy Mater 2014;4:1400432. https://doi.org/10.1002/aenm.201400432.

[73] Han GD, Bae K, Kang EH, Choi HJ, Shim JH. Inkjet Printing for Manufacturing Solid Oxide Fuel Cells. ACS Energy Lett 2020;5:1586–92. https://doi.org/10.1021/acsenergylett.0c00721.

[74] Park JS, Choi HJ, Han GD, Koo J, Kang EH, Kim DH, et al. High–performance protonic ceramic fuel cells with a PrBa0.5Sr0.5Co1.5Fe0.5O5+δ cathode with palladium–rich interface coating. J Power Sources 2021;482:229043. https://doi.org/10.1016/j.jpowsour.2020.229043.

[75] Chung S, Cho K, Lee T. Recent Progress in Inkjet-Printed Thin-Film Transistors. Advanced Science 2019;6:1801445. https://doi.org/10.1002/advs.201801445.

[76] Chen S, Li Y, Lin Y, He P, Long T, Deng C, et al. Inkjet-printed top-gate thin-film transistors based on InGaSnO semiconductor layer with improved etching resistance. Coatings 2020;10:1–9. https://doi.org/10.3390/coatings10040425.

[77] Fang Y, Wu X, Lan S, Zhong J, Sun D, Chen H, et al. Inkjet-Printed Vertical Organic Field-Effect Transistor Arrays and Their Image Sensors. ACS Appl Mater Interfaces 2018;10:30587–95. https://doi.org/10.1021/acsami.8b06625.

[78] Tung CW, Hou CH, Lin HT, Zheng Y, Huang YP, Liao YF, et al. In situ Observation of Electrodeposited Bimetallic p-Si Micropillar Array Photocathode for Solar-Driven Hydrogen Evolution. Solar RRL 2020;4:1–10. https://doi.org/10.1002/solr.202000028.

[79] Zhang F, Saleh E, Vaithilingam J, Li Y, Tuck CJ, Hague RJM, et al. Reactive material jetting of polyimide insulators for complex circuit board design. Addit Manuf 2019;25:477–84. https://doi.org/10.1016/j.addma.2018.11.017.

[80] Shimoda T, Morii K, Seki S, Kiguchi H. Inkjet Printing of Light-Emitting Polymer Displays. MRS Bull 2003;28:821–7. https://doi.org/10.1557/mrs2003.231.

[81] Barrett G, Omote R. Projected-capacitive touch technology. Inf Disp (1975) 2010;26:16–21. https://doi.org/10.1002/j.2637-496x.2010.tb00229.x.

[82] Han T, Kundu S, Nag A, Xu Y. 3D Printed Sensors for Biomedical Applications: A Review. Sensors 2019;19:1706. https://doi.org/10.3390/s19071706.

[83] Zhang S, Cai L, Li W, Miao J, Wang T, Yeom J, et al. Fully Printed Silver-Nanoparticle-Based Strain Gauges with Record High Sensitivity. Adv Electron Mater 2017;3. https://doi.org/10.1002/aelm.201700067.

[84] Subramanya SB, Nagarjuna Neella, Anantha Prasad MG, Nayak MM. Study and tailoring of screen-printed resistive films for disposable strain gauges. Sens Actuators A Phys 2019;295:380–95. https://doi.org/10.1016/j.sna.2019.06.008.

[85] Muth JT, Vogt DM, Truby RL, Mengüç Y, Kolesky DB, Wood RJ, et al. Embedded 3D Printing of Strain Sensors within Highly Stretchable Elastomers. Advanced Materials 2014;26:6307–12. https://doi.org/10.1002/adma.201400334.

[86] Abas M, Rahman K. Fabrication of flex sensors through direct ink write technique and its electrical characterization. Applied Physics A 2016;122:972. https://doi.org/10.1007/s00339-016-0507-8.

[87] Kim S, Oh J, Jeong D, Park W, Bae J. Consistent and Reproducible Direct Ink Writing of Eutectic Gallium–Indium for High-Quality Soft Sensors. Soft Robot 2018;5:601–12. https://doi.org/10.1089/soro.2017.0103.

[88] Agarwala S, Goh GL, Dinh Le T-S, An J, Peh ZK, Yeong WY, et al. Wearable Bandage-Based Strain Sensor for Home Healthcare: Combining 3D Aerosol Jet

Printing and Laser Sintering. ACS Sens 2019;4:218–26. https://doi.org/10.1021/acssensors.8b01293.

[89] Zhao J, Zhang Y, Huang Y, Xie J, Zhao X, Li C, et al. 3D Printing Fiber Electrodes for an All-Fiber Integrated Electronic Device via Hybridization of an Asymmetric Supercapacitor and a Temperature Sensor. Advanced Science 2018;5. https://doi.org/10.1002/advs.201801114.

[90] Courbat J, Kim YB, Briand D, de Rooij NF. Inkjet printing on paper for the realization of humidity and temperature sensors. 2011 16th International Solid-State Sensors, Actuators and Microsystems Conference, IEEE; 2011, p. 1356–9. https://doi.org/10.1109/TRANSDUCERS.2011.5969506.

[91] Dankoco MD, Tesfay GY, Benevent E, Bendahan M. Temperature sensor realized by inkjet printing process on flexible substrate. Mater Sci Eng B Solid State Mater Adv Technol 2016;205:1–5. https://doi.org/10.1016/j.mseb.2015.11.003.

[92] Barmpakos D, Segkos A, Tsamis C, Kaltsas G. A Disposable Inkjet-Printed Humidity and Temperature Sensor Fabricated on Paper. Proc West Mark Ed Assoc Conf 2018;2:977. https://doi.org/10.3390/proceedings2130977.

[93] Vuorinen T, Niittynen J, Kankkunen T, Kraft TM, Mäntysalo M. Inkjet-printed graphene/PEDOT:PSS temperature sensors on a skin-conformable polyurethane substrate. Sci Rep 2016;6:35289. https://doi.org/10.1038/srep35289.

[94] Dua V, Surwade SP, Ammu S, Agnihotra SR, Jain S, Roberts KE, et al. All-Organic Vapor Sensor Using Inkjet-Printed Reduced Graphene Oxide.

Angewandte Chemie 2010;122:2200–3. https://doi.org/10.1002/ange.200905089.

[95] Bali C, Brandlmaier A, Ganster A, Raab O, Zapf J, Hübler A. Fully Inkjet-Printed Flexible Temperature Sensors Based on Carbon and PEDOT: PSS. Mater Today Proc 2016;3:739–45. https://doi.org/10.1016/j.matpr.2016.02.005.

[96] Sajid M, Gul JZ, Kim SW, Kim HB, Na KH, Choi KH. Development of 3D-Printed Embedded Temperature Sensor for Both Terrestrial and Aquatic Environmental Monitoring Robots. 3D Print Addit Manuf 2018;5:160–9. https://doi.org/10.1089/3dp.2017.0092.

[97] Mannoor MS, Jiang Z, James T, Kong YL, Malatesta KA, Soboyejo WO, et al. 3D Printed Bionic Ears. Nano Lett 2013;13:2634–9. https://doi.org/10.1021/nl4007744.

[98] Su C-K, Yen S-C, Li T-W, Sun Y-C. Enzyme-Immobilized 3D-Printed Reactors for Online Monitoring of Rat Brain Extracellular Glucose and Lactate. Anal Chem 2016;88:6265–73. https://doi.org/10.1021/acs.analchem.6b00272.

[99] Loo AH, Chua CK, Pumera M. DNA biosensing with 3D printing technology. Analyst 2017;142:279–83. https://doi.org/10.1039/C6AN02038K.

[100] Lawes S, Sun Q, Lushington A, Xiao B, Liu Y, Sun X. Inkjet-printed silicon as high performance anodes for Li-ion batteries. Nano Energy 2017;36:313–21. https://doi.org/10.1016/j.nanoen.2017.04.041.

[101] Gu Y, Wu A, Sohn H, Nicoletti C, Iqbal Z, Federici JF. Fabrication of rechargeable lithium ion batteries using water-based inkjet printed cathodes. J

Manuf Process 2015;20:198–205. https://doi.org/10.1016/j.jmapro.2015.08.003.

[102] Zhao Y, Zhou Q, Liu L, Xu J, Yan M, Jiang Z. A novel and facile route of ink-jet printing to thin film SnO2 anode for rechargeable lithium ion batteries. Electrochim Acta 2006;51:2639–45. https://doi.org/10.1016/j.electacta.2005.07.050.

[103] Lacey SD, Kirsch DJ, Li Y, Morgenstern JT, Zarket BC, Yao Y, et al. Extrusion-Based 3D Printing of Hierarchically Porous Advanced Battery Electrodes. Advanced Materials 2018;30. https://doi.org/10.1002/adma.201705651.

[104] Fu K, Wang Y, Yan C, Yao Y, Chen Y, Dai J, et al. Graphene Oxide-Based Electrode Inks for 3D-Printed Lithium-Ion Batteries. Advanced Materials 2016;28:2587–94. https://doi.org/10.1002/adma.201505391.

[105] Sun K, Wei T, Ahn BY, Seo JY, Dillon SJ, Lewis JA. 3D Printing of Interdigitated Li-Ion Microbattery Architectures. Advanced Materials 2013;25:4539–43. https://doi.org/10.1002/adma.201301036.

[106] Zhang F, Wei M, Viswanathan V V, Swart B, Shao Y, Wu G, et al. 3D printing technologies for electrochemical energy storage. Nano Energy 2017;40:418–31. https://doi.org/10.1016/j.nanoen.2017.08.037.

[107] Reyes C, Somogyi R, Niu S, Cruz MA, Yang F, Catenacci MJ, et al. Three-Dimensional Printing of a Complete Lithium Ion Battery with Fused Filament Fabrication. ACS Appl Energy Mater 2018;1:5268–79. https://doi.org/10.1021/acsaem.8b00885.

[108] Sztymela K, Bienia M, Rossignol F, Mailley S, Ziesche S, Varghese J, et al. Fabrication of modern lithium ion batteries by 3D inkjet printing: opportunities and challenges. Heliyon 2022;8:e12623. https://doi.org/10.1016/j.heliyon.2022.e12623.

[109] Ho CC, Murata K, Steingart DA, Evans JW, Wright PK. A super ink jet printed zinc-silver 3D microbattery. Journal of Micromechanics and Microengineering 2009;19:094013. https://doi.org/10.1088/0960-1317/19/9/094013.

[110] Pang Y, Cao Y, Chu Y, Liu M, Snyder K, MacKenzie D, et al. Additive Manufacturing of Batteries. Adv Funct Mater 2020;30:1906244. https://doi.org/10.1002/adfm.201906244.

[111] Tang X, Zhou H, Cai Z, Cheng D, He P, Xie P, et al. Generalized 3D Printing of Graphene-Based Mixed-Dimensional Hybrid Aerogels. ACS Nano 2018;12:3502–11. https://doi.org/10.1021/acsnano.8b00304.

[112] Sun G, An J, Chua CK, Pang H, Zhang J, Chen P. Layer-by-layer printing of laminated graphene-based interdigitated microelectrodes for flexible planar micro-supercapacitors. Electrochem Commun 2015;51:33–6. https://doi.org/10.1016/j.elecom.2014.11.023.

[113] Sajedi-Moghaddam A, Rahmanian E, Naseri N. Inkjet-Printing Technology for Supercapacitor Application: Current State and Perspectives. ACS Appl Mater Interfaces 2020;12:34487–504. https://doi.org/10.1021/acsami.0c07689.

[114] Diao J, Yuan J, Ding A, Zheng J, Lu Z. Flexible Supercapacitor Based on Inkjet-Printed Graphene@Polyaniline Nanocomposites with Ultrahigh Capacitance. Macromol Mater Eng 2018;303. https://doi.org/10.1002/mame.201800092.

[115] Constantine A. Balanis. Antenna theory: Analysis and Design. 4th Edition. John Wiley & Sons; 2016.

[116] Hasan MdR, Riheen MA, Sekhar P, Karacolak T. An Ink-jet Printed Flexible Monopole Antenna for Super Wideband Applications. 2020 IEEE Texas Symposium on Wireless and Microwave Circuits and Systems (WMCS), IEEE; 2020, p. 1–4. https://doi.org/10.1109/WMCS49442.2020.9172396.

[117] AlSabbagh HM, Elwi TA, Al-Naiemy Y, Al-Rizzo HM. A compact triple-band metamaterial-inspired antenna for wearable applications. Microw Opt Technol Lett 2020;62:763–77. https://doi.org/10.1002/mop.32067.

[118] Li Y, Rongwei Z, Staiculescu D, Wong CP, Tentzeris MM. A Novel Conformal RFID-Enabled Module Utilizing Inkjet-Printed Antennas and Carbon Nanotubes for Gas-Detection Applications. IEEE Antennas Wirel Propag Lett 2009;8:653–6. https://doi.org/10.1109/LAWP.2009.2024104.

[119] Monne MA, Grubb PM, Stern H, Subbaraman H, Chen RT, Chen MY. Inkjet-Printed graphene-based 1 x 2 phased array antenna. Micromachines (Basel) 2020;11:1–12. https://doi.org/10.3390/MI11090863.

[120] Bihar E, Corzo D, Hidalgo TC, Rosas-Villalva D, Salama KN, Inal S, et al. Fully Inkjet-Printed, Ultrathin and Conformable Organic Photovoltaics as Power Source Based on Cross-Linked PEDOT:PSS Electrodes. Adv Mater Technol 2020;5. https://doi.org/10.1002/admt.202000226.

[121] Dodoo-Arhin D, Howe RCT, Hu G, Zhang Y, Hiralal P, Bello A, et al. Inkjet-printed graphene electrodes for dye-sensitized solar cells. Carbon N Y 2016;105:33–41. https://doi.org/10.1016/j.carbon.2016.04.012.

[122] Jung S, Sou A, Banger K, Ko D, Chow PCY, McNeill CR, et al. All-Inkjet-Printed, All-Air-Processed Solar Cells. Adv Energy Mater 2014;4. https://doi.org/10.1002/aenm.201400432.

[123] Pi X, Zhang L, Yang D. Enhancing the Efficiency of Multicrystalline Silicon Solar Cells by the Inkjet Printing of Silicon-Quantum-Dot Ink. The Journal of Physical Chemistry C 2012;116:21240–3. https://doi.org/10.1021/jp307078g.

[124] Mathies F, Eggers H, Richards BS, Hernandez-Sosa G, Lemmer U, Paetzold UW. Inkjet-Printed Triple Cation Perovskite Solar Cells. ACS Appl Energy Mater 2018;1:1834–9. https://doi.org/10.1021/acsaem.8b00222.

[125] Mathies F, Abzieher T, Hochstuhl A, Glaser K, Colsmann A, Paetzold UW, et al. Multipass inkjet printed planar methylammonium lead iodide perovskite solar cells. J Mater Chem A Mater 2016;4:19207–13. https://doi.org/10.1039/C6TA07972E.

[126] Wang F, Gosling JH, Trindade GF, Rance GA, Makarovsky O, Cottam ND, et al. Inter-Flake Quantum Transport of Electrons and Holes in Inkjet-Printed Graphene Devices. Adv Funct Mater 2021;31:2007478. https://doi.org/10.1002/adfm.202007478.

[127] Han X, Yang Y, Xu Y, Hong X, Tang Z, Zhang H, et al. 3D micro-nano printing technology as a transformative tool apply for microneedle drug delivery. J Drug Deliv Sci Technol 2024;96:105709. https://doi.org/10.1016/j.jddst.2024.105709.

[128] Huddy JE, Tiwari AP, Zhao H, Li Y, Scheideler WJ. Graph Theory Design of 3D Printed Conductive Lattice Electrodes. Adv Mater Technol 2023;8. https://doi.org/10.1002/admt.202300180.

[129] Askari M, Hutchins DA, Thomas PJ, Astolfi L, Watson RL, Abdi M, et al. Additive manufacturing of metamaterials: A review. Addit Manuf 2020;36:101562. https://doi.org/10.1016/j.addma.2020.101562.

[130] Derby B. Inkjet printing of functional and structural materials: Fluid property requirements, feature stability, and resolution. Annu Rev Mater Res 2010;40:395–414. https://doi.org/10.1146/annurev-matsci-070909-104502.

[131] Stratasys. What is PolyJet Technology for 3D Printing? | Stratasys 2019. https://www.stratasys.com/polyjet-technology (accessed May 24, 2021).

[132] Sele CW, von Werne T, Friend RH, Sirringhaus H. Lithography-Free, Self-Aligned Inkjet Printing with Sub-Hundred-Nanometer Resolution. Advanced Materials 2005;17:997–1001. https://doi.org/10.1002/adma.200401285.

[133] Bromberg V, Ma S, Singler TJ. High-resolution inkjet printing of electrically conducting lines of silver nanoparticles by edge-enhanced twin-line deposition. Appl Phys Lett 2013;102:214101. https://doi.org/10.1063/1.4807782.

[134] Seifert T, Sowade E, Roscher F, Wiemer M, Gessner T, Baumann RR. Additive manufacturing technologies compared: Morphology of deposits of silver ink using inkjet and aerosol jet printing. Ind Eng Chem Res 2015;54. https://doi.org/10.1021/ie503636c.

[135] Skylar-Scott MA, Gunasekaran S, Lewis JA. Laser-assisted direct ink writing of planar and 3D metal architectures. Proceedings of the National Academy of Sciences 2016;113:6137–42. https://doi.org/10.1073/pnas.1525131113.

[136] Ling S, Tian X, Zeng Q, Qin Z, Kurt SA, Tan YJ, et al. Tension-driven three-dimensional printing of free-standing Field's metal structures. Nat Electron 2024;7:671–83. https://doi.org/10.1038/s41928-024-01207-y.

[137] Park Y-G, An HS, Kim J-Y, Park J-U. High-resolution, reconfigurable printing of liquid metals with three-dimensional structures. Sci Adv 2019;5:2844. https://doi.org/10.1126/sciadv.aaw2844.

[138] Kullmann C, Schirmer NC, Lee M-T, Ko SH, Hotz N, Grigoropoulos CP, et al. 3D micro-structures by piezoelectric inkjet printing of gold nanofluids. Journal of Micromechanics and Microengineering 2012;22:055022. https://doi.org/10.1088/0960-1317/22/5/055022.

[139] Sadeq Saleh M, HamidVishkasougheh M, Zbib H, Panat R. Polycrystalline micropillars by a novel 3-D printing method and their behavior under compressive loads. Scr Mater 2018;149:144–9. https://doi.org/10.1016/j.scriptamat.2018.02.027.

[140] Sadeq Saleh M, Ritchie S, Nicholas M, Bezbaruah R, Reddy J, Chamanzar M, et al. CMU Array: A 3D Nano-Printed, Customizable Ultra-High-Density Microelectrode Array Platform. BioRxiv 2019:742346. https://doi.org/10.1101/742346.

[141] Saleh MS, Hu C, Panat R. Three-dimensional microarchitected materials and devices using nanoparticle assembly by pointwise spatial printing. Sci Adv 2017;3:1601986. https://doi.org/10.1126/sciadv.1601986.

[142] Saleh MS, Hu C, Brenneman J, Al Mutairi AM, Panat R. 3D printed three-dimensional metallic microlattices with controlled and tunable mechanical

properties. Addit Manuf 2021;39:101856. https://doi.org/10.1016/j.addma.2021.101856.

[143] Krall M, Brandstetter M, Deutsch C, Detz H, Andrews AM, Schrenk W, et al. Subwavelength micropillar array terahertz lasers. Opt Express 2014;22:274. https://doi.org/10.1364/OE.22.000274.

[144] Kunturu PP, Zachariadis C, Witczak L, Nguyen MD, Rijnders G, Huskens J. Tandem Si Micropillar Array Photocathodes with Conformal Copper Oxide and a Protection Layer by Pulsed Laser Deposition. ACS Appl Mater Interfaces 2019;11:41402–14. https://doi.org/10.1021/acsami.9b14408.

[145] Wang J, Liang R, Liu L, Shan B, Wang J, Xu J. Near-infrared light emitting diode array based on ordered Si micropillar/InGaZnO-nanofilm heterojunctions. 2016 IEEE International Conference on Electron Devices and Solid-State Circuits, EDSSC 2016, vol. 5, IEEE; 2016, p. 78–81. https://doi.org/10.1109/EDSSC.2016.7785214.

[146] Kameya Y, Yamaki H, Ono R, Motosuke M. Fabrication of micropillar TiO 2 photocatalyst arrays using nanoparticle-microprinting method. Mater Lett 2016;175:262–5. https://doi.org/10.1016/j.matlet.2016.04.013.

[147] Pariy IO, Ivanova AA, Shvartsman VV, Lupascu DC, Sukhorukov GB, Surmeneva MA, et al. Poling and annealing of piezoelectric Poly(Vinylidene fluoride) micropillar arrays. Mater Chem Phys 2020;239:122035. https://doi.org/10.1016/j.matchemphys.2019.122035.

[148] Gaysornkaew S, Tsumori F. Active control of surface profile by magnetic micropillar arrays. Jpn J Appl Phys 2021;60:SCCL02. https://doi.org/10.35848/1347-4065/abe698.

[149] Prehn R, Abad L, Sánchez-Molas D, Duch M, Sabaté N, del Campo FJ, et al. Microfabrication and characterization of cylinder micropillar array electrodes. Journal of Electroanalytical Chemistry 2011;662:361–70. https://doi.org/10.1016/j.jelechem.2011.09.002.

[150] Op de Beeck J, De Malsche W, Vangelooven J, Gardeniers H, Desmet G. Hydrodynamic chromatography of polystyrene microparticles in micropillar array columns. J Chromatogr A 2010;1217:6077–84. https://doi.org/10.1016/j.chroma.2010.07.031.

[151] Luo Y, Shao J, Chen S, Chen X, Tian H, Li X, et al. Flexible Capacitive Pressure Sensor Enhanced by Tilted Micropillar Arrays. ACS Appl Mater Interfaces 2019;11:17796–803. https://doi.org/10.1021/acsami.9b03718.

[152] Peng Y, Zang X, Zhu Y, Shi C, Chen L, Cai B, et al. Ultra-broadband terahertz perfect absorber by exciting multi-order diffractions in a double-layered grating structure. Opt Express 2015;23:2032. https://doi.org/10.1364/OE.23.002032.

[153] Li X, Shen Z, Tan Q, Hu W. High Efficient Metadevices for Terahertz Beam Shaping. Front Phys 2021;9:1–8. https://doi.org/10.3389/fphy.2021.659747.

[154] Chen C, Ran B, Wang Z, Zhao H, Lan M, Chen H, et al. Development of micropillar array electrodes for highly sensitive detection of biomarkers. RSC Adv 2020;10:41110–9. https://doi.org/10.1039/D0RA07694E.

[155] Kim DE. Dynamic Leidenfrost temperature behaviors on uniformly distributed micropillars. Exp Therm Fluid Sci 2020;111:109954. https://doi.org/10.1016/j.expthermflusci.2019.109954.

[156] Li S, Zhang L, Chen X. 3D-printed terahertz metamaterial absorber based on vertical split-ring resonator. J Appl Phys 2021;130. https://doi.org/10.1063/5.0056276.

[157] Grob L, Rinklin P, Zips S, Mayer D, Weidlich S, Terkan K, et al. Inkjet-printed and electroplated 3d electrodes for recording extracellular signals in cell culture. Sensors 2021;21. https://doi.org/10.3390/s21123981.

[158] Galliker P, Schneider J, Eghlidi H, Kress S, Sandoghdar V, Poulikakos D. Direct printing of nanostructures by electrostatic autofocussing of ink nanodroplets. Nat Commun 2012;3. https://doi.org/10.1038/ncomms1891.

[159] Lejeune M, Chartier T, Dossou-Yovo C, Noguera R. Ink-jet printing of ceramic micro-pillar arrays. J Eur Ceram Soc 2009;29. https://doi.org/10.1016/j.jeurceramsoc.2008.07.040.

[160] Cappi B, Ebert J, Telle R. Rheological properties of aqueous Si3N4 and MoSi 2 suspensions tailor-made for direct inkjet printing. Journal of the American Ceramic Society 2011;94. https://doi.org/10.1111/j.1551-2916.2010.04052.x.

[161] Grob L, Yamamoto H, Zips S, Rinklin P, Hirano-Iwata A, Wolfrum B. Printed 3D Electrode Arrays with Micrometer-Scale Lateral Resolution for Extracellular Recording of Action Potentials. Adv Mater Technol 2020;5. https://doi.org/10.1002/admt.201900517.

[162] Wang X, Guo Q, Cai X, Zhou S, Kobe B, Yang J. Initiator-integrated 3D printing enables the formation of complex metallic architectures. ACS Appl Mater Interfaces 2014;6. https://doi.org/10.1021/am4050822.

[163] An BW, Kim K, Lee H, Kim SY, Shim Y, Lee DY, et al. High-Resolution Printing of 3D Structures Using an Electrohydrodynamic Inkjet with Multiple Functional Inks. Advanced Materials 2015;27:4322–8. https://doi.org/10.1002/adma.201502092.

[164] Guo SZ, Heuzey MC, Therriault D. Properties of polylactide inks for solvent-cast printing of three-dimensional freeform microstructures. Langmuir 2014;30. https://doi.org/10.1021/la4036425.

[165] Rivers G, Lion A, Putri NRE, Rance GA, Moloney C, Taresco V, et al. Enabling high-fidelity personalised pharmaceutical tablets through multimaterial inkjet 3D printing with a water-soluble excipient. Mater Today Adv 2024;22:100493. https://doi.org/10.1016/j.mtadv.2024.100493.

[166] Saleh E, Zhang F, He Y, Vaithilingam J, Fernandez JL, Wildman R, et al. 3D Inkjet Printing of Electronics Using UV Conversion. Adv Mater Technol 2017;2:1700134. https://doi.org/10.1002/admt.201700134.

[167] Shamkhalichenar H, Bueche CJ, Choi J-W. Printed Circuit Board (PCB) Technology for Electrochemical Sensors and Sensing Platforms. Biosensors (Basel) 2020;10:159. https://doi.org/10.3390/bios10110159.

[168] Nano Dimension. Whitepapers - Nano Dimension. Https://WwwNano-DiCom/Resources/Whitepapers/ n.d. https://www.nano-di.com/resources/whitepapers/ (accessed August 29, 2024).

[169] Scott JGV. Digital printing for printed circuit boards. Circuit World 2005;31:34–41. https://doi.org/10.1108/03056120510603125.

[170] Kwon K-S, Rahman MdK, Phung TH, Hoath S, Jeong S, Kim JS. Review of digital printing technologies for electronic materials. Flexible and Printed Electronics 2020. https://doi.org/10.1088/2058-8585/abc8ca.

[171] HUMMINK. HUMMINK - The world's smallest fountain pen revolution. Https://HumminkCom/Worlds-Smallest-Fountain-Pen-Revolution/ 2024. https://hummink.com/worlds-smallest-fountain-pen-revolution/ (accessed October 8, 2024).

[172] Ji A, Chen Y, Wang X, Xu C. Inkjet printed flexible electronics on paper substrate with reduced graphene oxide/carbon black ink. Journal of Materials Science: Materials in Electronics 2018;29:13032–42. https://doi.org/10.1007/s10854-018-9425-1.

[173] Chen Y, Zhou L, Wei J, Mei C, Jiang S, Pan M, et al. Direct Ink Writing of Flexible Electronics on Paper Substrate with Graphene/Polypyrrole/Carbon Black Ink. J Electron Mater 2019;48:3157–68. https://doi.org/10.1007/s11664-019-07085-x.

[174] Abas M, Salman Q, Khan AM, Rahman K. Direct ink writing of flexible electronic circuits and their characterization. Journal of the Brazilian Society of Mechanical Sciences and Engineering 2019;41:563. https://doi.org/10.1007/s40430-019-2066-3.

[175] Zhang D, Chi B, Li B, Gao Z, Du Y, Guo J, et al. Fabrication of highly conductive graphene flexible circuits by 3D printing. Synth Met 2016;217:79–86. https://doi.org/10.1016/j.synthmet.2016.03.014.

[176] Hu M, Cai X, Guo Q, Bian B, Zhang T, Yang J. Direct Pen Writing of Adhesive Particle-Free Ultrahigh Silver Salt-Loaded Composite Ink for Stretchable

Circuits. ACS Nano 2016;10:396–404. https://doi.org/10.1021/acsnano.5b05082.

[177] Vaithilingam J, Saleh E, Tuck C, Wildman R, Ashcroft I, Hague R, et al. 3D-inkjet printing of flexible and stretchable electronics. Proceedings - 26th Annual International Solid Freeform Fabrication Symposium - An Additive Manufacturing Conference, SFF 2015, 2020, p. 1513–26.

[178] Paulsen JA, Renn M, Christenson K, Plourde R. Printing conformal electronics on 3D structures with Aerosol Jet technology. 2012 Future of Instrumentation International Workshop (FIIW) Proceedings, IEEE; 2012, p. 1–4. https://doi.org/10.1109/FIIW.2012.6378343.

[179] Voltera. NOVA Technical Datasheet. 2024.

[180] Im J, Trindade GF, Quach TT, Sohaib A, Wang F, Austin J, et al. Functionalized Gold Nanoparticles with a Cohesion Enhancer for Robust Flexible Electrodes. ACS Appl Nano Mater 2022;5:6708–16. https://doi.org/10.1021/acsanm.2c00742.

[181] Joannopoulos JD, Johnson SG, Winn JN, Meade RD. Photonic crystals: Molding the flow of light. 2nd ed. Princeton University Press; 2011.

[182] Younes B, Omi AI, Sagar MdSI, Sajeeb MMH, Karacolak T, Sekhar P. A Physically Compact Coplanar Waveguide (CPW)-fed Flexible Antenna for mmWave 5G Applications. 2022 12th International Conference on Electrical and Computer Engineering (ICECE), IEEE; 2022, p. 196–9. https://doi.org/10.1109/ICECE57408.2022.10088784.

[183] Yuxiao He, Oakley C, Chahal P, Albrecht J, Papapolymerou J. Aerosol Jet printed 24 GHz end-fire quasi-Yagi-Uda antenna on a 3-D printed cavity substrate. 2017 International Workshop on Antenna Technology: Small Antennas, Innovative Structures, and Applications (iWAT), IEEE; 2017, p. 179–82. https://doi.org/10.1109/IWAT.2017.7915352.

[184] Farooqui MF, Claudel C, Shamim A. An inkjet-printed buoyant 3-D lagrangian sensor for real-time flood monitoring. IEEE Trans Antennas Propag 2014;62:3354–9. https://doi.org/10.1109/TAP.2014.2309957.

[185] Njogu P, Sanz-Izquierdo B, Elibiary A, Jun SY, Chen Z, Bird D. 3D Printed Fingernail Antennas for 5G Applications. IEEE Access 2020;8:228711–9. https://doi.org/10.1109/ACCESS.2020.3043045.

[186] O'Reilly M, Renn MJ, Sessoms D. Aerosol Jet® Enabled 3D Antenna and Sensors for IoT Applications. International Symposium on Microelectronics 2015;2015:000203–9. https://doi.org/10.4071/isom-2015-WA14.

[187] Adams JJ, Duoss EB, Malkowski TF, Motala MJ, Ahn BY, Nuzzo RG, et al. Conformal Printing of Electrically Small Antennas on Three-Dimensional Surfaces. Advanced Materials 2011;23:1335–40. https://doi.org/10.1002/adma.201003734.

[188] Li S, Njogu P, Izquierdo BS, Gao S, Chen Z. 3D Printing Antennas for 5G and Millimeter Wave 6G Applications. 2022 IEEE 33rd Annual International Symposium on Personal, Indoor and Mobile Radio Communications (PIMRC), IEEE; 2022, p. 1–5. https://doi.org/10.1109/PIMRC54779.2022.9978007.

[189] Fan J, Zhang L, Wei S, Zhang Z, Choi S-K, Song B, et al. A review of additive manufacturing of metamaterials and developing trends. Materials Today 2021;50:303–28. https://doi.org/10.1016/j.mattod.2021.04.019.

[190] Ling K, Yoo M, Su W, Kim K, Cook B, Tentzeris MM, et al. Microfluidic tunable inkjet-printed metamaterial absorber on paper. Opt Express 2015;23:110. https://doi.org/10.1364/OE.23.000110.

[191] Kim H, Lee D, Lim S. A Fluidically Tunable Metasurface Absorber for Flexible Large-Scale Wireless Ethanol Sensor Applications. Sensors 2016;16:1246. https://doi.org/10.3390/s16081246.

[192] Hu BB, Nuss MC. Imaging with terahertz waves. Opt Lett 1995;20:1716. https://doi.org/10.1364/ol.20.001716.

[193] Ishigaki K, Shiraishi M, Suzuki S, Asada M, Nishiyama N, Arai S. Direct intensity modulation and wireless data transmission characteristics of terahertz-oscillating resonant tunnelling diodes. Electron Lett 2012;48:582. https://doi.org/10.1049/el.2012.0849.

[194] Takano K, Kawabata T, Hsieh C-F, Akiyama K, Miyamaru F, Abe Y, et al. Fabrication of Terahertz Planar Metamaterials Using a Super-Fine Ink-Jet Printer. Applied Physics Express 2010;3:016701. https://doi.org/10.1143/APEX.3.016701.

[195] Kashiwagi K, Xie L, Li X, Kageyama T, Miura M, Miyashita H, et al. Inkjet-printed silver-nanoparticle THz metamaterial. 2016 41st International Conference on Infrared, Millimeter, and Terahertz waves (IRMMW-THz), IEEE; 2016, p. 1–2. https://doi.org/10.1109/IRMMW-THz.2016.7758981.

[196] Zheng Z, Zheng Y, Luo Y, Yi Z, Zhang J, Liu Z, et al. A switchable terahertz device combining ultra-wideband absorption and ultra-wideband complete reflection. Physical Chemistry Chemical Physics 2022;24:2527–33. https://doi.org/10.1039/D1CP04974G.

[197] Walther M, Ortner A, Meier H, Löffelmann U, Smith PJ, Korvink JG. Terahertz metamaterials fabricated by inkjet printing. Appl Phys Lett 2009;95. https://doi.org/10.1063/1.3276544.

[198] Vogt DW, Leonhardt R. 3D-Printed Broadband Dielectric Tube Terahertz Waveguide with Anti-Reflection Structure. J Infrared Millim Terahertz Waves 2016;37:1086–95. https://doi.org/10.1007/s10762-016-0296-3.

[199] Oakley C, Kaur A, Byford JA, Chahal P. Aerosol-Jet Printed Quasi-Optical Terahertz Filters. 2017 IEEE 67th Electronic Components and Technology Conference (ECTC), IEEE; 2017, p. 248–53. https://doi.org/10.1109/ECTC.2017.233.

[200] Lin SY, Fleming JG, Hetherington DL, Smith BK, Biswas R, Ho KM, et al. A three-dimensional photonic crystal operating at infrared wavelengths. Nature 1998;394:251–3. https://doi.org/10.1038/28343.

[201] Rurup JD, Secor EB. Predicting Deposition Rate and Closing the Loop on Aerosol Jet Printing with In-Line Light Scattering Measurements. Adv Eng Mater 2023;25. https://doi.org/10.1002/adem.202201919.

[202] Optomec. 3D Printed Electronics - Aerosol Jet Technology - Optomec 2024. https://optomec.com/printed-electronics/aerosol-jet-technology/ (accessed October 8, 2024).

[203] Cicor. Printed Electronics | Cicor 2024. https://www.cicor.com/en/solutions/printed-electronics/ (accessed October 8, 2024).

[204] Rahman T, Renaud L, Heo D, Renn M, Panat R. Aerosol based direct-write micro-additive fabrication method for sub-mm 3D metal-dielectric structures. Journal of Micromechanics and Microengineering 2015;25:107002. https://doi.org/10.1088/0960-1317/25/10/107002.

[205] Nano-Dimension. Nano Dimension_Inks User Guide 2020:1–52.

[206] Antohe B V., Wallace DB. Acoustic Phenomena in a Demand Mode Piezoelectric Ink jet Printer. Journal of Imaging Science and Technology 2002;46:409–14. https://doi.org/10.2352/J.ImagingSci.Technol.2002.46.5.art00003.

[207] Martin GD, Hoath SD, Hutchings IM. Inkjet printing - The physics of manipulating liquid jets and drops. J Phys Conf Ser 2008;105. https://doi.org/10.1088/1742-6596/105/1/012001.

[208] Fromm JE. Numerical Calculation of the Fluid Dynamics of Drop-on-Demand Jets. IBM J Res Dev 1984;28:322–33. https://doi.org/10.1147/rd.283.0322.

[209] Duineveld PC, de Kok MM, Buechel M, Sempel A, Mutsaers KAH, van de Weijer P, et al. Ink-jet printing of polymer light-emitting devices. In: Kafafi ZH, editor. Organic Light-Emitting Materials and Devices V, vol. 4464, 2002, p. 59. https://doi.org/10.1117/12.457460.

[210] Stow CD, Hadfield MG. An experimental investigation of fluid flow resulting from the impact of a water drop with an unyielding dry surface. Proceedings of

the Royal Society of London A Mathematical and Physical Sciences 1981;373:419–41. https://doi.org/10.1098/rspa.1981.0002.

[211] Mundo C, Sommerfeld M, Tropea C. Droplet-wall collisions: Experimental studies of the deformation and breakup process. International Journal of Multiphase Flow 1995;21:151–73. https://doi.org/10.1016/0301-9322(94)00069-V.

[212] Kamyshny A, Magdassi S. Conductive nanomaterials for 2D and 3D printed flexible electronics. Chem Soc Rev 2019;48:1712–40. https://doi.org/10.1039/c8cs00738a.

[213] Liu Y-FF, Tsai M-HH, Pai Y-FF, Hwang W-SS. Control of droplet formation by operating waveform for inks with various viscosities in piezoelectric inkjet printing. Appl Phys A Mater Sci Process 2013;111:509–16. https://doi.org/10.1007/s00339-013-7569-7.

[214] Lamont CA, Eggenhuisen TM, Coenen MJJ, Slaats TWL, Andriessen R, Groen P. Tuning the viscosity of halogen free bulk heterojunction inks for inkjet printed organic solar cells. Org Electron 2015;17:107–14. https://doi.org/10.1016/j.orgel.2014.10.052.

[215] Matavž A, Frunză RC, Drnovšek A, Bobnar V, Malič B, Matavz A, et al. Inkjet printing of uniform dielectric oxide structures from sol–gel inks by adjusting the solvent composition. J Mater Chem C Mater 2016;4:5634–41. https://doi.org/10.1039/C6TC01090C.

[216] McManus D, Vranic S, Withers F, Sanchez-Romaguera V, Macucci M, Yang H, et al. Water-based and biocompatible 2D crystal inks for all-inkjet-printed

heterostructures. Nat Nanotechnol 2017;12:343–50. https://doi.org/10.1038/nnano.2016.281.

[217] Yang P, Zhang L, Kang DJ, Strahl R, Kraus T. High-Resolution Inkjet Printing of Quantum Dot Light-Emitting Microdiode Arrays. Adv Opt Mater 2020;8:1901429. https://doi.org/10.1002/adom.201901429.

[218] Wilson P, Lekakou C, Watts J. Electrical, morphological and electronic properties of inkjet printed PEDOT:PSS. 2012 12th IEEE International Conference on Nanotechnology (IEEE-NANO), IEEE; 2012, p. 1–6. https://doi.org/10.1109/NANO.2012.6322210.

[219] Kamyshny A, Ben-Moshe M, Aviezer S, Magdassi S. Ink-Jet Printing of Metallic Nanoparticles and Microemulsions. Macromol Rapid Commun 2005;26:281–8. https://doi.org/https://doi.org/10.1002/marc.200400522.

[220] Torrisi F, Hasan T, Wu W, Sun Z, Lombardo A, Kulmala TS, et al. Inkjet-printed graphene electronics. ACS Nano 2012;6:2992–3006. https://doi.org/10.1021/nn2044609.

[221] Fernandes IJ, Aroche AF, Schuck A, Lamberty P, Peter CR, Hasenkamp W, et al. Silver nanoparticle conductive inks: synthesis, characterization, and fabrication of inkjet-printed flexible electrodes. Sci Rep 2020;10:8878. https://doi.org/10.1038/s41598-020-65698-3.

[222] Shen W, Zhang X, Huang Q, Xu Q, Song W. Preparation of solid silver nanoparticles for inkjet printed flexible electronics with high conductivity. Nanoscale 2014;6:1622–8. https://doi.org/10.1039/C3NR05479A.

[223] Park YG, Yun I, Chung WG, Park W, Lee DH, Park JU. High-Resolution 3D Printing for Electronics. Advanced Science 2022;9:2104623. https://doi.org/10.1002/ADVS.202104623.

[224] Farraj Y, Grouchko M, Magdassi S. Self-reduction of a copper complex MOD ink for inkjet printing conductive patterns on plastics. Chemical Communications 2015;51:1587–90. https://doi.org/10.1039/C4CC08749F.

[225] Xu D, Sanchez-Romaguera V, Barbosa S, Travis W, de Wit J, Swan P, et al. Inkjet printing of polymer solutions and the role of chain entanglement. J Mater Chem 2007;17:4902. https://doi.org/10.1039/b710879f.

[226] He Y, Tuck CJ, Prina E, Kilsby S, Christie SDR, Edmondson S, et al. A new photocrosslinkable polycaprolactone-based ink for three-dimensional inkjet printing. J Biomed Mater Res B Appl Biomater 2017;105:1645–57. https://doi.org/10.1002/jbm.b.33699.

[227] Graddage N, Chu T-Y, Ding H, Py C, Dadvand A, Tao Y. Inkjet printed thin and uniform dielectrics for capacitors and organic thin film transistors enabled by the coffee ring effect. Org Electron 2016;29:114–9. https://doi.org/10.1016/j.orgel.2015.11.039.

[228] Rioboo R, Tropea C, Marengo M. OUTCOMES FROM A DROP IMPACT ON SOLID SURFACES. Atomization and Sprays 2001;11:12. https://doi.org/10.1615/AtomizSpr.v11.i2.40.

[229] Yarin AL. DROP IMPACT DYNAMICS: Splashing, Spreading, Receding, Bouncing…. Annu Rev Fluid Mech 2006;38:159–92. https://doi.org/10.1146/annurev.fluid.38.050304.092144.

[230] Schiaffino S, Sonin AA. Molten droplet deposition and solidification at low Weber numbers. Physics of Fluids 1997;9:3172–87. https://doi.org/10.1063/1.869434.

[231] Sirringhaus H, Kawase T, Friend RH, Shimoda T, Inbasekaran M, Wu W, et al. High-resolution inkjet printing of all-polymer transistor circuits. Science (1979) 2000;290:2123–6. https://doi.org/10.1126/science.290.5499.2123.

[232] Wang JZ, Zheng ZH, Li HW, Huck WTS, Sirringhaus H. Dewetting of conducting polymer inkjet droplets on patterned surfaces. Nat Mater 2004;3:171–6. https://doi.org/10.1038/nmat1073.

[233] Lee SH, Shin KY, Hwang JY, Kang KT, Kang HS. Silver inkjet printing with control of surface energy and substrate temperature. Journal of Micromechanics and Microengineering 2008;18:75014. https://doi.org/10.1088/0960-1317/18/7/075014.

[234] Lee S-H, Cho Y-J. Characterization of Silver Inkjet Overlap-printing through Cohesion and Adhesion. Journal of Electrical Engineering and Technology 2012;7:91–6. https://doi.org/10.5370/JEET.2012.7.1.91.

[235] Goo Y-S, Lee Y-I, Kim N, Lee K-J, Yoo B, Hong S-J, et al. Ink-jet printing of Cu conductive ink on flexible substrate modified by oxygen plasma treatment. Surf Coat Technol 2010;205:S369–72. https://doi.org/10.1016/j.surfcoat.2010.08.039.

[236] Boon KL, Xiao H. Transient contact angle of evaporating inkjet droplet on trans-parent polymer substrate. 2010 12th Electronics Packaging Technology Conference, IEEE; 2010, p. 240–5. https://doi.org/10.1109/EPTC.2010.5702640.

[237] Soltman D, Subramanian V. Inkjet-Printed Line Morphologies and Temperature Control of the Coffee Ring Effect. Langmuir 2008;24:2224–31. https://doi.org/10.1021/la7026847.

[238] Yen TM, Fu X, Wei T, Nayak RU, Shi Y, Lo Y-H. Reversing Coffee-Ring Effect by Laser-Induced Differential Evaporation. Sci Rep 2018;8:3157. https://doi.org/10.1038/s41598-018-20581-0.

[239] Zhang Z, Si T. Controllable assembly of silver nanoparticles based on the coffee-ring effect for high-sensitivity flexible strain gauges. Sens Actuators A Phys 2017;264:188–94. https://doi.org/10.1016/j.sna.2017.08.012.

[240] Cuk T, Troian SM, Hong CM, Wagner S. Using convective flow splitting for the direct printing of fine copper lines. Appl Phys Lett 2000;77:2063–5. https://doi.org/10.1063/1.1311954.

[241] Zhang Z, Zhang X, Xin Z, Deng M, Wen Y, Song Y. Controlled Inkjetting of a Conductive Pattern of Silver Nanoparticles Based on the Coffee-Ring Effect. Advanced Materials 2013;25:6714–8. https://doi.org/10.1002/adma.201303278.

[242] Zhang L, Liu H, Zhao Y, Sun X, Wen Y, Guo Y, et al. Inkjet Printing High-Resolution, Large-Area Graphene Patterns by Coffee-Ring Lithography. Advanced Materials 2012;24:436–40. https://doi.org/10.1002/adma.201103620.

[243] Smith P, Derby B, Reis N, Wallwork A, Ainsley C. Measured Anisotropy of Alumina Components Produced by Direct Ink-Jet Printing. Key Eng Mater 2004;264–268:693–6. https://doi.org/10.4028/www.scientific.net/KEM.264-268.693.

[244] Seerden KAM, Reis N, Evans JRG, Grant PS, Halloran JW, Derby B. Ink-Jet Printing of Wax-Based Alumina Suspensions. Journal of the American Ceramic Society 2001;84:2514–20. https://doi.org/10.1111/j.1151-2916.2001.tb01045.x.

[245] van den Berg AMJ, de Laat AWM, Smith PJ, Perelaer J, Schubert US. Geometric control of inkjet printed features using a gelating polymer. J Mater Chem 2007;17:677–83. https://doi.org/10.1039/B612158F.

[246] Park J, Moon J. Control of Colloidal Particle Deposit Patterns within Picoliter Droplets Ejected by Ink-Jet Printing. Langmuir 2006;22:3506–13. https://doi.org/10.1021/la053450j.

[247] Kim D, Jeong S, Park BK, Moon J. Direct writing of silver conductive patterns: Improvement of film morphology and conductance by controlling solvent compositions. Appl Phys Lett 2006;89:264101. https://doi.org/10.1063/1.2424671.

[248] Gibbs JW. On the equilibrium of heterogeneous substances. Transactions of the Connecticut Academy of Arts and Sciences 1878;3:343–524.

[249] de Gans B-J, Schubert US. Inkjet Printing of Well-Defined Polymer Dots and Arrays. Langmuir 2004;20:7789–93. https://doi.org/10.1021/la049469o.

[250] Zhang Y, Yang S, Chen L, Evans JRG. Shape Changes during the Drying of Droplets of Suspensions. Langmuir 2008;24:3752–8. https://doi.org/10.1021/la703484w.

[251] He P, Derby B. Inkjet printing ultra-large graphene oxide flakes. 2d Mater 2017;4:021021. https://doi.org/10.1088/2053-1583/aa629e.

[252] Li Y, Yang Q, Li M, Song Y. Rate-dependent interface capture beyond the coffee-ring effect. Sci Rep 2016;6:24628. https://doi.org/10.1038/srep24628.

[253] Zhang J, Milzetti J, Leroy F, Müller-Plathe F. Formation of coffee-stain patterns at the nanoscale: The role of nanoparticle solubility and solvent evaporation rate. J Chem Phys 2017;146:114503. https://doi.org/10.1063/1.4978284.

[254] Sommer AP, Ben-Moshe M, Magdassi S. Size-Discriminative Self-Assembly of Nanospheres in Evaporating Drops. J Phys Chem B 2004;108:8–10. https://doi.org/10.1021/jp0363747.

[255] Bhardwaj R, Fang X, Somasundaran P, Attinger D. Self-Assembly of Colloidal Particles from Evaporating Droplets: Role of DLVO Interactions and Proposition of a Phase Diagram. Langmuir 2010;26:7833–42. https://doi.org/10.1021/la9047227.

[256] Bhardwaj R, Fang X, Attinger D. Pattern formation during the evaporation of a colloidal nanoliter drop: a numerical and experimental study. New J Phys 2009;11:75020. https://doi.org/10.1088/1367-2630/11/7/075020.

[257] Li F, Leo PH, Barnard JA. Dendrimer Pattern Formation in Evaporating Drops: Solvent, Size, and Concentration Effects. The Journal of Physical Chemistry C 2008;112:14266–73. https://doi.org/10.1021/jp802850y.

[258] Truskett VN, Stebe KJ. Influence of Surfactants on an Evaporating Drop: Fluorescence Images and Particle Deposition Patterns. Langmuir 2003;19:8271–9. https://doi.org/10.1021/la030049t.

[259] He Y. An investigation of inkjet printing of polycaprolactone based inks. University of Nottingham, 2016.

[260] Simon J, Langenscheidt A. Curing behavior of a UV-curable inkjet ink: Distinction between surface-cure and deep-cure performance. J Appl Polym Sci 2020;137. https://doi.org/10.1002/app.49218.

[261] Xie D, Zhang HH, Shu XY, Xiao JF. Fabrication of polymer micro-lens array with pneumatically diaphragm-driven drop-on-demand inkjet technology. Opt Express 2012;20:15186. https://doi.org/10.1364/OE.20.015186.

[262] Vaithilingam J, Saleh E, Körner L, Wildman RD, Hague RJM, Leach RK, et al. 3-Dimensional inkjet printing of macro structures from silver nanoparticles. Mater Des 2018;139:81–8. https://doi.org/10.1016/j.matdes.2017.10.070.

[263] Goh GL, Zhang H, Chong TH, Yeong WY. 3D Printing of Multilayered and Multimaterial Electronics: A Review. Adv Electron Mater 2021;7. https://doi.org/10.1002/aelm.202100445.

[264] Correia V, Mitra KY, Castro H, Rocha JG, Sowade E, Baumann RR, et al. Design and fabrication of multilayer inkjet-printed passive components for printed electronics circuit development. J Manuf Process 2018;31:364–71. https://doi.org/10.1016/j.jmapro.2017.11.016.

[265] Liu Z, Huang J, Li P, Ping B, Zhang J, Meng F, et al. High-precision inkjet 3D printing of curved multi-material structures: Morphology evolution and optimization. Addit Manuf 2024;94:104497. https://doi.org/10.1016/j.addma.2024.104497.

[266] Vu IQ, Bass LB, Williams CB, Dillard DA. Characterizing the effect of print orientation on interface integrity of multi-material jetting additive manufacturing. Addit Manuf 2018;22:447–61. https://doi.org/https://doi.org/10.1016/j.addma.2018.05.036.

[267] Liu F, Li T, Jiang X, Jia Z, Xu Z, Wang L. The effect of material mixing on interfacial stiffness and strength of multi-material additive manufacturing. Addit Manuf 2020;36:101502. https://doi.org/10.1016/j.addma.2020.101502.

[268] Cummins G, Desmulliez MPY. Inkjet printing of conductive materials: A review. Circuit World 2012;38:193–213. https://doi.org/10.1108/03056121211280413.

[269] Bailey C, Stoyanov S, Tilford T, Tourloukis G. 3D-printing and electronic packaging. 2016 Pan Pacific Microelectronics Symposium, Pan Pacific 2016 2016. https://doi.org/10.1109/PanPacific.2016.7428385.

[270] Gokhale P, Mitra D, Sowade E, Mitra KY, Gomes HL, Ramon E, et al. Controlling the crack formation in inkjet-printed silver nanoparticle thin-films for high resolution patterning using intense pulsed light treatment. Nanotechnology 2017;28:495301. https://doi.org/10.1088/1361-6528/aa9238.

[271] Ko SH, Pan H, Grigoropoulos CP, Luscombe CK, Fréchet JMJ, Poulikakos D. All-inkjet-printed flexible electronics fabrication on a polymer substrate by low-temperature high-resolution selective laser sintering of metal nanoparticles. Nanotechnology 2007;18:345202. https://doi.org/10.1088/0957-4484/18/34/345202.

[272] Li L, Pan L, Ma Z, Yan K, Cheng W, Shi Y, et al. All Inkjet-Printed Amperometric Multiplexed Biosensors Based on Nanostructured Conductive

Hydrogel Electrodes. Nano Lett 2018;18:3322–7. https://doi.org/10.1021/acs.nanolett.8b00003.

[273] Meyer Burger. PiXDRO LP50 User manual - V5.0 n.d.

[274] GIMP 2019.

[275] MATLAB 2021.

[276] El-Azazy M. Introductory Chapter: Infrared Spectroscopy - A Synopsis of the Fundamentals and Applications. Infrared Spectroscopy - Principles, Advances, and Applications, 2019. https://doi.org/10.5772/intechopen.82210.

[277] Paramelle D, Sadovoy A, Gorelik S, Free P, Hobley J, Fernig DG. A rapid method to estimate the concentration of citrate capped silver nanoparticles from UV-visible light spectra. Analyst 2014;139:4855. https://doi.org/10.1039/C4AN00978A.

[278] Goodhew PJ, Humphreys J, Humphreys J. Electron Microscopy and Analysis. 3rd ed. CRC Press; 2000. https://doi.org/10.1201/9781482289343.

[279] Nanoscience Instruments. Scanning Electron Mictoscopy | Nanoscience Instruments 2024. https://www.nanoscience.com/techniques/scanning-electron-microscopy/ (accessed September 20, 2024).

[280] Schindelin J, Arganda-Carreras I, Frise E, Kaynig V, Longair M, Pietzsch T, et al. Fiji: an open-source platform for biological-image analysis. Nat Methods 2012;9:676–82. https://doi.org/10.1038/nmeth.2019.

[281] Klemm A. ImageJ/Fiji Macro Language - [NEUBIASAcademy@Home] Course 2020.

[282] NIST. Schematic of an Atomic Force Microscope 2024. https://www.nist.gov/image/afmschematic (accessed September 20, 2024).

[283] Schroder DK. Semiconductor Material and Device Characterization. Hoboken, NJ, USA: John Wiley & Sons, Inc.; 2005. https://doi.org/10.1002/0471749095.

[284] Weir WB. Automatic measurement of complex dielectric constant and permeability at microwave frequencies. Proceedings of the IEEE 1974;62:33–6. https://doi.org/10.1109/PROC.1974.9382.

[285] Nicolson AM, Ross GF. Measurement of the Intrinsic Properties of Materials by Time-Domain Techniques. IEEE Trans Instrum Meas 1970;19:377–82. https://doi.org/10.1109/TIM.1970.4313932.

[286] Minakov AV, Rudyak VYa, Pryazhnikov MI. Rheological behavior of water and ethylene glycol based nanofluids containing oxide nanoparticles. Colloids Surf A Physicochem Eng Asp 2018;554:279–85. https://doi.org/10.1016/j.colsurfa.2018.06.051.

[287] XTPL. Certificate of Analysis XTPL Ag Nanoink IJ36 3465_IJ36_1 2022.

[288] Malvern Panalytical. An Introduction to Dynamic Light Scattering (DLS) | Malvern Panalytical 2024. https://www.malvernpanalytical.com/en/learn/knowledge-center/technical-notes/tn101104dynamiclightscatteringintroduction (accessed October 28, 2024).

[289] Chen J, Pei Z, Chai B, Jiang P, Ma L, Zhu L, et al. Engineering the Dielectric Constants of Polymers: From Molecular to Mesoscopic Scales. Advanced Materials 2023. https://doi.org/10.1002/adma.202308670.

[290] Zair L, Berrayah A, Arabeche K, Bouberka Z, Best A, Koynov K, et al. Temperature Controlled Mechanical Reinforcement of Polyacrylate Films Containing Nematic Liquid Crystals. Polymers (Basel) 2022;14:5024. https://doi.org/10.3390/polym14225024.

[291] Huang W, Zhang J, Singh V, Xu L, Kabi P, Bele E, et al. Digital light 3D printing of a polymer composite featuring robustness, self-healing, recyclability and tailorable mechanical properties. Addit Manuf 2023;61:103343. https://doi.org/10.1016/j.addma.2022.103343.

[292] Hagiopol C. Copolymers. Encyclopedia of Condensed Matter Physics, Elsevier; 2005, p. 235–40. https://doi.org/10.1016/B0-12-369401-9/00544-1.

[293] He Y, Abdi M, Trindade GF, Begines B, Dubern J, Prina E, et al. Exploiting Generative Design for 3D Printing of Bacterial Biofilm Resistant Composite Devices. Advanced Science 2021;8. https://doi.org/10.1002/advs.202100249.

[294] Stringer J, Derby B. Formation and Stability of Lines Produced by Inkjet Printing. Langmuir 2010;26:10365–72. https://doi.org/10.1021/la101296e.

[295] Lemarchand J, Bridonneau N, Battaglini N, Carn F, Mattana G, Piro B, et al. Challenges, Prospects, and Emerging Applications of Inkjet-Printed Electronics: A Chemist's Point of View. Angewandte Chemie International Edition 2022;61:e202200166. https://doi.org/10.1002/ANIE.202200166.

[296] Colton T, Crane NB. Influence of droplet velocity, spacing, and inter-arrival time on line formation and saturation in binder jet additive manufacturing. Addit Manuf 2021;37:101711. https://doi.org/10.1016/J.ADDMA.2020.101711.

[297] Colton T, Inkley C, Berry A, Crane NB. Impact of inkjet printing parameters and environmental conditions on formation of 2D and 3D binder jetting geometries. J Manuf Process 2021;71:187–96. https://doi.org/10.1016/J.JMAPRO.2021.09.024.

[298] Elkaseer A, Schneider S, Deng Y, Scholz SG. Effect of Process Parameters on the Performance of Drop-On-Demand 3D Inkjet Printing: Geometrical-Based Modeling and Experimental Validation. Polymers (Basel) 2022;14. https://doi.org/10.3390/POLYM14132557.

[299] Hu S, Zhu W, Yang W, Li M. Morphology simulation of drop-on-demand inkjet-printed droplets. Npj Flexible Electronics 2022 6:1 2022;6:1–11. https://doi.org/10.1038/s41528-022-00187-3.

[300] Reyes-Luna JF, Chang S, Tuck C, Ashcroft I. A surrogate modelling strategy to improve the surface morphology quality of inkjet printing applications. J Manuf Process 2023;89:458–71. https://doi.org/10.1016/J.JMAPRO.2023.01.078.

[301] Kang H, Soltman D, Subramanian V. Hydrostatic optimization of inkjet-printed films. Langmuir 2010;26:11568–73. https://doi.org/10.1021/LA100822S/SUPPL_FILE/LA100822S_SI_001.PDF.

[302] Hu H, Larson RG. Marangoni effect reverses coffee-ring depositions. Journal of Physical Chemistry B 2006;110:7090–4. https://doi.org/10.1021/JP0609232.

[303] Hu G, Albrow-Owen T, Jin X, Ali A, Hu Y, Howe RCT, et al. Black phosphorus ink formulation for inkjet printing of optoelectronics and photonics. Nat Commun 2017;8. https://doi.org/10.1038/s41467-017-00358-1.

[304] Friederich A, Binder JR, Bauer W. Rheological Control of the Coffee Stain Effect for Inkjet Printing of Ceramics. Journal of the American Ceramic Society 2013;96:2093–9. https://doi.org/10.1111/JACE.12385.

[305] Sliz R, Czajkowski J, Fabritius T. Taming the Coffee Ring Effect: Enhanced Thermal Control as a Method for Thin-Film Nanopatterning. Langmuir 2020;36:9562–70. https://doi.org/10.1021/ACS.LANGMUIR.0C01560/SUPPL_FILE/LA0C01560_SI_002.MP4.

[306] Sliz R, Lejay M, Fan JZ, Choi M-J, Kinge S, Hoogland S, et al. Stable colloidal quantum dot inks enable inkjet-printed high-sensitivity infrared photodetectors. ACS Nano 2019;13:11988–95.

[307] Buga C, C Viana J. Optimization of print quality of inkjet printed PEDOT:PSS patterns. Flexible and Printed Electronics 2022;7:045004. https://doi.org/10.1088/2058-8585/ac931e.

[308] Qiu X, Gong X, Zhang X, Zheng W. Ink-Jet Printing towards Ultra-High Resolution: A Review. Coatings 2022, Vol 12, Page 1893 2022;12:1893. https://doi.org/10.3390/COATINGS12121893.

[309] Cook RL. Stochastic sampling in computer graphics. ACM Transactions on Graphics (TOG) 1986;5. https://doi.org/10.1145/7529.8927.

[310] Floyd RW, Steinberg L. An Adaptive Algorithm for Spatial Gray Scale. Society for Information Display, vol. 17, 1976.

[311] Ahn J, Jeong JG, Hong H, Yoon YJ. A simple method for miniaturization of self-complementary Archimedean spiral antenna. 2015 International Workshop

on Antenna Technology, iWAT 2015, 2015. https://doi.org/10.1109/IWAT.2015.7365328.

[312] Kaur N, Sivia JS, Kaur M. Design of Modified Sierpinski Gasket Fractal Antenna for C and X-band applications. Proceedings of the 2015 IEEE 3rd International Conference on MOOCs, Innovation and Technology in Education, MITE 2015, 2016. https://doi.org/10.1109/MITE.2015.7375324.

[313] Choi JH, Ryu K, Park K, Moon S-J. Thermal conductivity estimation of inkjet-printed silver nanoparticle ink during continuous wave laser sintering. Int J Heat Mass Transf 2015;85:904–9. https://doi.org/10.1016/j.ijheatmasstransfer.2015.01.056.

[314] Nelson-Dummett O, Rivers G, Gilani N, Simonelli M, Tuck CJ, Wildman RD, et al. Off the Grid: A new strategy for material-jet 3D printing with enhanced sub-droplet resolution. Additive Manufacturing Letters 2024;8:100185. https://doi.org/10.1016/j.addlet.2023.100185.

[315] Vaithilingam J, Saleh E, Körner L, Wildman RD, Hague RJM, Leach RK, et al. 3-Dimensional inkjet printing of macro structures from silver nanoparticles. Mater Des 2018;139:81–8. https://doi.org/10.1016/j.matdes.2017.10.070.

[316] Saleh E, Vaithilingam J, Tuck C, Wildman R, Ashcroft I, Hague R, et al. 3D inkjet printing of conductive structures using in-situ IR sintering. Proceedings - 26th Annual International Solid Freeform Fabrication Symposium - An Additive Manufacturing Conference, SFF 2015, 2020, p. 1554–9.